MODIFIED THERMAL REDUCTION OF GRAPHENE OXIDE

HAO LIU

Thesis submitted to the University of Nottingham for the degree

of Doctor of Philosophy

January 2014

Abstract

As a strictly two-dimensional carbon material, graphene has attracted great interest in recent years due to its unique mechanical, electrical and optical properties. Currently, the principal methods for mass production of graphene are focused on the solution-based chemical redox reaction. The oxidation of graphite introduces a large amount of oxygen functional groups attached onto its basal plane or edges, which makes graphene oxide (GO) sheets hydrophilic to form stable aqueous colloids. However, the raw material graphite gradually becomes an insulator during the oxidation process as part of planar sp^2-hybridized geometry transformed to distorted sp^3-hybridized geometry, which loses its excellent electronic properties. As a result, reduction of GO is definitely necessary to recover its "lost" electrical conductivity for practical applications. In addition, the hydrophilic property of GO sheets allows metal oxide (MO) nanoparticles (NPs) anchoring on reduced graphene oxide (rGO) plane to fabricate MO/rGO composites with excellent electrochemical performance. However, the current preparation methods for the electrical conductive MO/rGO composites are very complicated which might have negative effects on the properties and hinder mass production. The objective of this project is to synthesize aluminium oxide (Al_2O_3)/rGO nanocomposites via oxygen annealing without using an Al_2O_3 precursor. This method establishes a very simple and efficient way to yield Al_2O_3 NPs on rGO plane by filtering GO dispersion through an Anodisc membrane filter with oxygen annealing, which is named oxygenally reduced graphene oxide (OrGO). The characterizations reveal that the Al_2O_3 NPs are formed exclusively on the edges of defective regions with

uniform particle size less than 10 nm. As for the electronic properties, OrGO has a higher electrical conductivity at 7250 S m^{-1} with a narrower range of the electrical conductivity mostly between 6500 and 7250 S m^{-1}, which can be due to the increase of the sp^2/sp^3 carbon ratio caused by the formation of Al_2O_3 NPs at the edges of defective regions in OrGO plane. Moreover, the formation of Al_2O_3 NPs maintains OrGO sheets with good hydrophilic property with a contact angle around 71.5 °. The electrochemical performance of OrGO paper fabricated as electrode materials for lithium-ion batteries (LIBs) is also investigated. OrGO electrodes exhibit a high specific charge and discharge capacity at 1328 and 1364 mAh g^{-1}. The cyclic voltammograms (CV) performance reveal that the insertion of Li^+ ions begins at a very low potential around 0 V vs. Li^+/Li while the extraction process begins in the range of 0.2–0.3 V. In addition, the OrGO electrode has excellent rate capability and cycling performance. The average coulombic efficiency (CE) was measured at 99.608% for 30 cycles, indicating a superior reversibility of the Li^+ ion insertion/extraction process.

Publications

Journal paper:

H. Liu, K.-L. Choy, and M. Roe, *Enhanced conductivity of reduced graphene oxide decorated with aluminium oxide nanoparticles by oxygen annealing*. Nanoscale, 2013. **5**(13): p. 5725-5731.

Conference paper:

H. Liu, and K.-L. Choy, *Synthesis of aluminium oxide/graphene nanocomposites and application as an anode material for lithium-ion batteries.* MRS Spring Meeting, San Francisco, CA, Apr. 2013.

Presentation:

Poster presentation; H. Liu, K.-L. Choy, and H. Morvan, *Large-scale novel graphene based conducting nanocomposites*. Engineering Faculty Postgraduate Research event, the University of Nottingham, Nottingham, May, 2013.

Abbreviations

2D	Two-dimensional
α	Fine-structure constant
π	Pi
Ω	Ohm
ADF	Annular dark field
AFM	Atomic force microscopy
$Al(OH)_3$	Aluminium hydroxide
Al_2O_3	Aluminium oxide
Ar	Argon
ATR	Attenuated total reflection
$AuCl_4$	Gold(III) chloride
BSE	Back-scattered electrons
C	Carbon
C_{60}	Fullerene
CC/CV	Constant current / constant voltage
CCD	Charge-coupled device
CDG	Chemically derived graphene

CE	Coulombic efficiency
CL	Cathodoluminescence
ClO_2	Chlorine dioxide
cm	Centimetre
CNT	Carbon nanotube
CO	Carbon monoxide
CO_2	Carbon dioxide
Cu	Copper
CV	Cyclic voltammograms
CVD	Chemical vapor deposition
DCE	1, 2-dichloroethane
DI	Deionized
DMF	N,N-dimethylformamide
DMSO	Dimethyl sulfoxide
DXR	Doxorubicin hydrochloride
EDX	Energy dispersive X-ray spectroscopy
EPD	Electrophoretic deposition

ESEM	Environmental SEM
ET	Electron transfer
FEG	Field emission gun
FTIR	Fourier transform infrared spectroscopy
FWHM	Full width at half maximum
g	Gram
GO	Graphene oxide
h	Hour
H	Hydrogen
H_2SO_4	Sulfuric acid
H_3PO_4	Phosphoric acid
HNO_3	Nitric acid
HOPG	Highly oriented pyrolytic graphite
HRTEM	High-resolution transmission electron microscopy
ITO	Indium tin oxide
$K_2S_2O_8$	Potassium persulfate
$KClO_3$	Potassium chlorate

$KMnO_4$	Potassium permanganate
KOH	Potassium hydroxide
Li	Lithium
LIB	Lithium-ion battery
$LiPF_6$	Lithium hexafluorophosphate
m	Mol
mA	Milliampere
min	Minute
MO	Metal oxide
mPa	Megapascal
N	Nitrogen
N_2O_4	Dinitrogen tetroxide
$NaBH_4$	Sodium borohydride
$NaNO_3$	Sodium nitrate
Ni	Nickel
NIR	Near-infrared
nm	Nanometre

NMR	Nuclear magnetic resonance
NO_2	Nitrogen dioxide
NP	Nanoparticle
O	Oxygen
OLED	Organic light-emitting diode
OrGO	Oxygenally reduced graphene oxide
P_2O_5	Phosphorus pentoxide
Pa	Pascal
PL	Photoluminescence
PMT	Photomultiplier tube
PSD	Position sensitive detector
Pt	Platinum
PVP	Poly-4-vinylphenol
QD	Quantum dot
rGO	Reduced graphene oxide
rpm	Revolutions per minute
Rs	Sheet resistance

Ru	Ruthenium
SAED	Selected area electron diffraction
SE	Secondary electrons
SEI	Solid electrolyte interface
SEM	Scanning electron microscopy
SiC	Silicon carbide
SiO_2	Silicon dioxide
SnO_2	Tin dioxide
$SOCl_2$	Thionyl chloride
sq	Square
STEM	Scanning transmission electron microscope
STM	Scanning tunneling microscopy
TEM	Transmission electron microscopy
THF	Tetrahydrofuran
TiO_2	Titanium dioxide
TrGO	Thermally reduced graphene oxide
UHV	Ultra-high vacuum

UV	Ultraviolet
UV-Vis	Ultra-High Vacuum
V	Volt
vis	Visible
W	Watt
XPS	X-ray photoelectron spectroscopy
XRD	X-ray diffraction
ZnO	Zinc oxide

Acknowledgements

With great pleasure and respect, I express my heartfelt gratitude to my supervisor Professor Kwang-Leong Choy for her continued support, motivation, patience and guidance during my PhD studies. I would also like to thank the China Scholarship Council (CSC) for funding my PhD for 4 years.

Professor Kwang-Leong Choy, thank you for giving me the opportunity to do a PhD and for being a calm head during the hectic times. You always had a solution! I have learnt so much from you.

I would like to thank the technical staff that helped me throughout the PhD process with my laboratory work. The supports from Vladimir Astachov and Michael Fay on AFM and HRTEM measurements, respectively, are gratefully acknowledged.

I am very grateful for the friendship and help from the current and past group members especially Dr. Xianghui Hou, Dr. Jungpeng Liu, Chyi Shen Tho, Marcus Jahn, and many others. I express my sincere thanks to my friends for helping me through the difficult times and for all their emotional support.

Finally, I would like to thank my family and girlfriend for being patient and understanding throughout the demanding PhD years. My parents Xiaoming Tang and Yongguo Liu as well as my girlfriend Lin Qiu, have always been my rock and I could not have done this without their moral and financial support.

Table of contents

Chapter 1 Introduction

1.1 Graphene

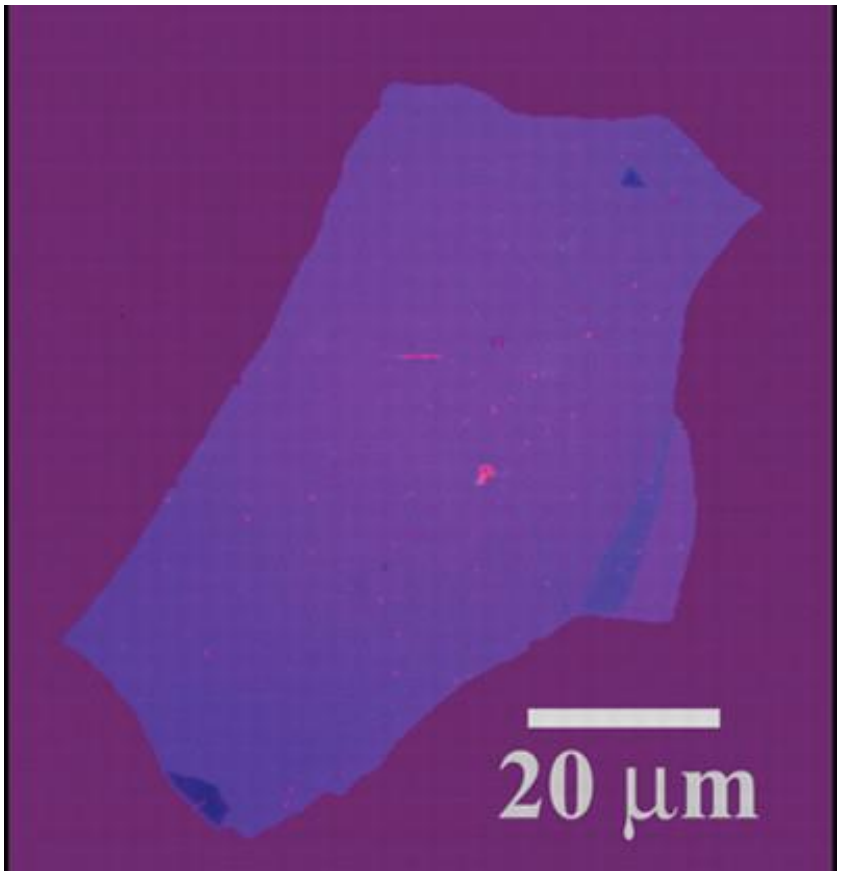

Figure 1.1 A graphene flake under bright field on top of an oxidized Si wafer[1]

In 2004, Geim and co-workers reported a strictly two-dimensional carbon material named graphene (Figure 1.1)[1]. It is a single layer of graphite with only one atom thick having unique mechanical, electrical and optical properties [2-4]. For example, the spring constant of graphene is in the range of 1-5 N/m and a Young's modulus of 0.5 Tpa, indicating a breaking strength 200 times greater than steel. These high values make graphene one of the strongest materials ever tested[2]. Graphene also has a very low electrical resistivity at room temperature of 10^{-6} Ω·cm, less than that of silver[3].

Moreover, its unique electronic structure makes graphene absorb a significant ($\pi\alpha$ =2.3%, α is the fine-structure constant) part of incident white light, which makes graphene an excellent candidate for terahertz applications [4]. Since graphene is a gapless semiconductor, its charge carriers can continuously cross the Dirac point from electrons to holes under an external electric field. The mobility of these charge carriers in graphene can exceed 105 $cm^2V^{-1}s^{-1}$ at low temperature, and is not influenced by the doping process as in conventional semiconductors [5]. For the thermal properties, graphene exhibits a strong heat conductivity measured between $(4.84\pm0.44)\times10^3$ to $(5.30\pm0.48)\times10^3$ $Wm^{-1}K^{-1}$. According to the literature, the thermal characteristics are proved to be significantly improved by embedding multiple layers of graphene into silicon chips. This result suggests that a lower temperature can be achieved by graphene, which promises chips with a higher processing speeds [6].

1.2 How to make graphene

Normally, graphene sheets can be made in three principal ways. The first method, micromechanical cleavage, was originally reported by Geim and other researchers in 2004[1].This method involves two steps, repeatedly splitting graphite crystals by Scotch tape and dissolving the resulted pieces in acetone. After depositing the dispersion onto a piece of silicon wafer, the sheets consisting of single layers of graphene were found under scanning electron microscopy (SEM) (Figure 1.2).

Figure 1.2 Micromechanical cleavage of graphite to obtain graphene using Scotch tape [7].

Although this method can produce the pristine graphene used for theoretical research, its complicated process and small size of graphene sheets obtained make the procedure difficult for practical applications.

The second route is growing epitaxially graphitic layers on top of silicon carbide at high temperature over 1100 ℃ [8]. The substrate is then removed by chemical etching to obtain free-standing graphene layers (Figure 1.3). However, it is not practical to use expensive Silicon carbide (SiC) substrate for industrial applications even though the epitaxial graphene expresses high quality.

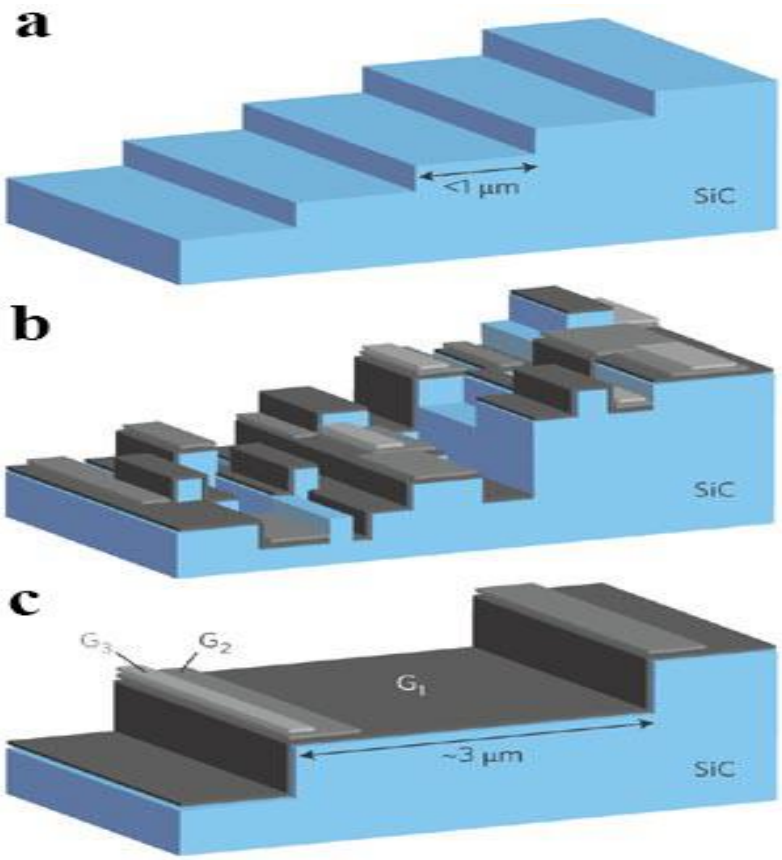

Figure 1.3 a, The starting material of SiC surface with a staircase of flat terraces. b, Fabrication process of vacuum-graphitized SiC. c, Morphology graphene obtained from the surface in high-pressure argon[8].

The third method used to obtain uniform and large-scale graphene films is chemical vapor deposition (CVD)[9].This method requires an operating temperature as high as 1,000 ℃ along with a hydrocarbon gas flow as precursor and pure hydrogen as a carrier gas, which limits the application range.

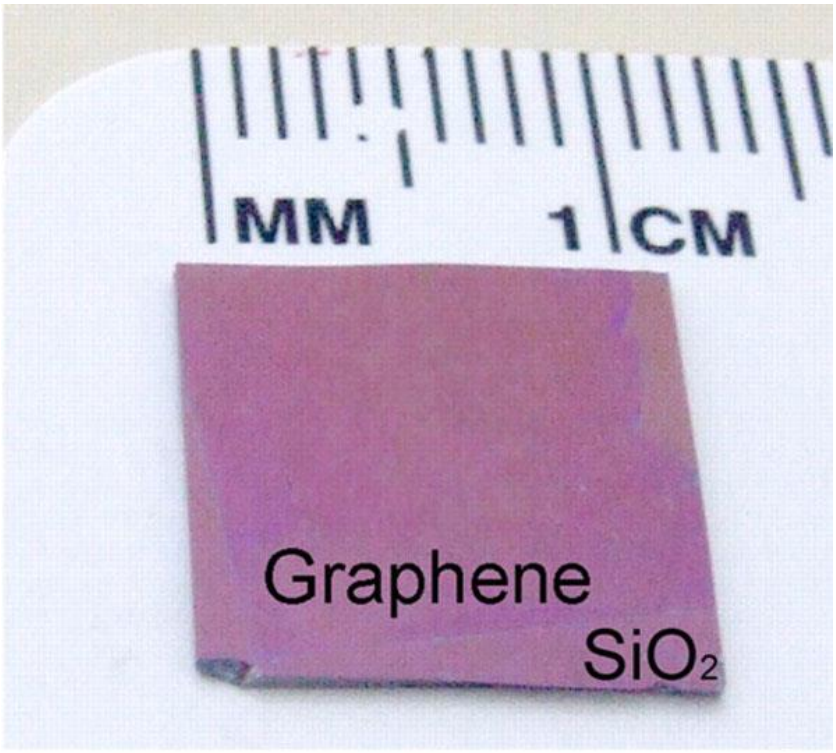

Figure 1.4 Graphene films synthesized by CVD method and transferred onto a silicon dioxide (SiO_2)/Si wafer [9]

1.3 Graphene oxide and mass production

The methods mentioned in 1.2 are inefficient and high-cost for the production of small quantities of graphene sheets, and cannot meet mass production requirements. The solution-based route, namely Hummers method, is considered able to produce graphene sheets in large amounts [10, 11]. In this technique, graphite is initially oxidized to synthesize strongly hydrophilic graphite oxide due to the large amounts of oxygen functional groups attached onto the basal or edge plane of graphite. These functional groups make graphite oxide easily exfoliated in solvent to form stable GO dispersion. GO can be partially reduced to form graphene-like materials by removing the oxygen functionalities from the basal plane and recovering the conjugated structure. The rGO sheets are normally grouped as the chemically derived

graphene[12]. Therefore, it seems advisable that the most intensive effort to reduce GO should be focused on producing graphene-like sheets with their structures and properties similar to the individual layers of graphite, the pristine graphene. For a more accurate expression, we will substitute “rGO” for “graphene” to describe the chemically derived graphene after the reduction process.

1.4 The Achilles' heel of GO

There are two important advantages enabling the mass production of GO. First of all, the chemical process uses inexpensive graphite as a raw material to produce GO sheets. On the other hand, the as-obtained highly hydrophilic GO sheets can easily form stable aqueous colloids, which facilitates a simple and feasible solution process for mass production of rGO.

However, graphite gradually becomes an insulator during the oxidation process as part of planar sp^2-hybridized geometry transformed to distorted sp^3-hybridized geometry, which loses the excellent electronic properties of graphite[13]. GO has to be reduced to restore the aromatic graphene networks so that the electrical conductivity can be recovered, in which case, most of the oxygen-containing functionalities have to be removed. However, a gradual decrease in hydrophilic character happens during the GO reduction process, which often results in irreversible agglomeration and precipitation.

1.5 Motivation

1.5.1 TrGO: the way to improve the electrical conductivity

Reduction of GO is definitely necessary to recover its "lost" electrical conductivity for practical applications. A variety of reduction processes have been applied to produce electrical conductive rGO with different properties. The reduction methods for GO sheets mainly include two strategies: chemical reagent reduction and thermal annealing.

Stankovich *et al.* first reported the chemical reduction method using hydrazine to obtain rGO sheets [11, 14]. Although hydrazine successfully reduced GO, the large-scale implementation of this highly toxic reagent for rGO mass production is not desirable. Moreover, extra nitrogen functional groups were introduced on rGO plane by hydrazine during the chemical reduction [15], which restricts the applications in gas sensor[16]. Sodium borohydride ($NaBH_4$) was accepted as a reducing reagent due to a more effective reduction capability than hydrazine. However, $NaBH_4$ can be slowly hydrolyzed in water so that it should be used freshly as a reductant. Furthermore, $NaBH_4$ is not highly effective in reducing epoxy groups and carboxylic acids although it can efficiently reduce C=O species, resulting in alcohol groups remaining on rGO plane after reduction [17].

GO also can be reduced by thermal annealing to achieve rGO, hence named "thermally reduced graphene oxide" (TrGO). The initial thermal annealing, rapid heating over 2000 ℃/min, was used to exfoliate graphite oxide to produce graphene

sheets [13, 18, 19]. During the process, the oxygen functional groups rapidly decomposed to form gases to increasing the pressure between the stacked layers of graphite oxide. Li *et al.* decreased the annealing temperature to 800 ^{O}C with high-quality GO sheets. After the oxidation process by Hummer's method, GO dispersion was repeatedly centrifuged at high rotation speed and resuspended in fresh 1, 2-dichloroethane (DCE)[20]. Further decrease of annealing temperature was achieved by a step thermal annealing process. GO sheets fabricated by Hummer's method was partially reduced by heating in Ar flow at 200 ^{O}C for 1 hour, the sample resistance went down to ~ 750 kΩ. The following thermal treatment at 300 °C increased the device electrical conductivity by 10 times due to more oxygen functional groups being removed from GO sheets plane[21].

1.5.2 NPs: boosts rGO potential

The uniform GO colloidal dispersion has been attracting great interest for its fascinating hydrophilic properties, which allows GO sheets anchoring NPs to form composites [22-27]. Reduction of as-formed nanocomposites boots their potential for use in optical, electronic, thermal, mechanical, and catalytic applications.[28-30] Moreover, the flexible and electrical conductive rGO sheets supporting the nanocomposites result in an enhanced electrochemical performance, which allows NP/rGO hybrids to be fabricated in electronic devices such as LIBs, electrochemical capacitors, field effect transistors and photodetectors [31-36]. For example, catalyst particles were distributed onto rGO sheets to fabricate selective catalytic composites

and sensors [37]. The large-band-gap MOs such as TiO_2 and ZnO can interact with carboxylic acid functional groups of GO to form rGO based semiconductor composites, which are photocatalytically active under ultraviolet (UV) irradiation[24, 38]. For the application of energy storage, lithium-ion batteries employing graphene as anodes were researched by many groups. In order to enhance the cycling performance, MO/rGO composites were assembled. For example, SnO_2/rGO anode material exhibits a reversible capacity of 810 mA h g^{-1} as well as 570 mA h g^{-1} after 30 cycles[31].

1.5.3 OrGO: an innovation behind fabrication of GO sheets

The NP/rGO composites are often made via two steps. Firstly, NPs distributes on GO sheets in aqueous dispersion prepared by Hummer's method forming the homogeneous composites. Secondly, reducing the composites is achieved by a variety of reduction processes such as chemical reduction and thermal annealing. For example, Gold(III) chloride ($AuCl_4^-$) reduced by $NaBH_4$ in a GO dispersion to form gold NP/rGO is a typical route for rGO based composites fabrication. $NaBH_4$ solution is mixed with GO dispersion in tetrahydrofuran (THF) followed by adding $AuCl_4^-$ to the mixture. Subsequently, excess $NaBH_4$ is added to the GO dispersion facilitating the reduction process of $AuCl_4^-$ and unfunctionalized oxygen functional groups. The as-formed GO dispersion is then measured and filtered through a membrane filter to fabricate custom-sized GO film, its size depending on the diameter of the filter. Followed by air-drying and peeling from the filter, the obtained rGO paper or rGO based composite paper can be used in many applications.

However, there is an innovation behind the filtration stage, which allows a very simple and efficient way to yield NP/rGO composites allowing the annealing process to fabricate rGO based nanocomposites without extra NPs, reductant and any kind of organic solvent. This innovation is an Anodisc membrane filter (aluminium oxide membrane, 47 mm in diameter, 0.2 μm pore size; Whatman), which is widely used in filtering GO dispersions to form GO papers due to its physical properties of hydrophilicity and porosity. Anodisc membrane filters are highly porous (about max. 50 – 65% at the surface), and the pores are disttributed in a hexagonal array. The manufacturers data indicate that the thickness of the membrane is about 60 μm and the pore density is about 10^{10} cm^{-2}. During the vacuum filtration, a small amount of Al_2O_3 NPs coming from the membrane filter is dissolved in DI water and then distributed on the GO plane owing to the liquid removed through the membrane pores under a directional flow by vacuum suction. The GO dispersion prepared by Hummer's method is subjected to vacuum filtration through the Anodisc membrane filter to produce GO paper. The vacuum filtration of a GO dispersion produces GO paper with an Anodisc membrane filter, resulting layers therefore becoming flexible in a paper-like structures which can be stretched and folded. This free-standing GO paper can be considered for applications such as flexible film batteries, hydrogen storage or electric membranes. Different from the conventional heat treatment for reducing GO paper by other groups, we modify the thermal annealing process by introducing oxygen gas flow to fabricate Al_2O_3 NP/rGO composites, named "oxygenally reduced graphene oxide" (OrGO). The oxygen gas flow used in the thermal treatment process

enables the removal of oxygen functional groups and recovery of defective regions. Herein, we present a simple approach for the preparation of large-area, free-standing, electrical conductive and hydrophilic OrGO paper and its potential application in LIBs.

1.6 The aims of this research project

The overall aim of this research is to unveil an innovative oxygen annealing method for the fabrication of Al_2O_3 NP/rGO composites and investigate the mechanism of Al_2O_3 NPs' distribution and aggregation on the GO plane. We also determine the electrical conductivity and wettability of OrGO paper followed by applying it in LIB. The key objectives of this research are shown as follows:

(i) To use modified Hummer's Method for synthesis of GO.

(ii) To fabricate GO paper by vacuum filtration through an Anodisc membrane filter.

(iii) To characterize the formation mechanism, and properties of OrGO sheets.

(iv) To study the electrochemical performance of OrGO paper as the electrode material in LIBs.

Chapter 2 Literature Review

2.1 Introduction

Graphene, a two-dimensional monolayer of graphite, has attracted intense research interest due to its unique mechanical, electrical and optical properties [2-4]. For its mass production, the strongly hydrophilic GO sheets synthesized by Hummer's method can be reduced for large-scale preparation of chemically derived graphene (CDG) sheets. GO is basically a wrinkled two-dimensional carbon material covered by oxygen functional groups on its basal plane and edges. Removing the oxygen functional groups by either chemical or thermal reduction processes enables GO to be a precursor for CDG fabrication. However, the oxygen functional groups on the GO plane can strongly affect the electronic, mechanical, and electrochemical properties, therefore resulting in the property differences between GO and pristine graphene [39]. The structural defects in GO produced by the chemical oxidation process limit its direct application especially in electronic devices due to the oxygen functional groups reducing the electrical conductivity of GO sheets [40]. However, the oxygen functionalization makes GO sheets strongly hydrophilic, which promises GO sheets an excellent dispersibility in many solvents(Figure 2.1)[41], particularly in water for further functionalization and derivatization.[42]. As a result, GO can form stable aqueous colloids to promote the mass production of rGO, which is important for industrial applications.

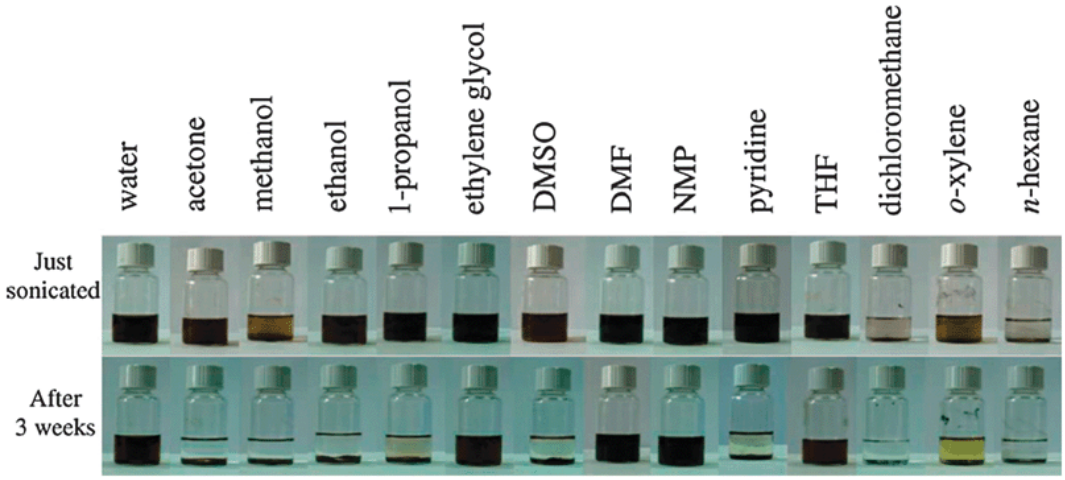

Figure 2.1 GO dispersed in DI water and other thirteen organic solvents by ultrasonication for 1 hour. Top: as-prepared dispersions after sonication. Bottom: dispersions settled aside for 3 weeks after sonication. [41]

Due to sp^2 bonding networks disrupted by chemical oxidation process, GO is electrically insulating. Thus, the reduction process is important to recover electrical conductivity by restoring the p-network. The reduction methods can be described as chemical, thermal, or electrochemical processes. Some of these methods can reduce the GO to a condition very closely resembling pristine graphene in terms of the electrical, thermal, and mechanical properties. The most commonly accepted reagent used for chemical reduction is hydrazine, which is not a strong reductant reacting with water [11]. The conductivity is usually enhanced by several orders of magnitude during the reduction processes. However, compared to mechanically cleaved graphene, the as-obtained rGO are much poorer in crystallinity and carrier mobility [43]. Moreover, the defects and vacancies within the sp^2 carbon lattice, caused by the chemical oxidation process in GO synthesis, are actually almost impossible to recover by subsequent chemical reduction treatments[44]. Chemical reduction is a common but certainly not the only method for the preparation of rGO. Instead of using a

chemical reduction route, directly heating GO in a furnace can also remove the oxide functionalities from the GO sheets surface. Results of the thermal exfoliation and reduction of GO have been reported [13, 19]. However, high temperature thermal annealing easily gives rise to structural damage as CO_2 released during the heating process[45], and a pressure of 130 MPa is generated at 1000 ^{O}C. As a result, holes and topological defects are left throughout the rGO sheets surface, which cause an approximately 30% mass loss of GO.

The excellent electrical conductivity along with thermal conductivity, high surface area (theoretically 2630 m^2/g for single-layer graphene) and strong mechanical strength [26] make the rGO useful in many applications, including electronics [46],solar cells [47],fuel cells [29, 48] as well as energy storage and conversion devices, such as supercapacitors [49, 50] and batteries[51-57]. Different from the brittle graphite, rGO sheets are flexible, which is an advantage for fabrication of flexible electronic and energy storage devices. Compared with the electrodes made from graphite, electrochemically active sites of graphene electrodes represent a more uniform distribution.

2.2 Limits of graphene and GO

The pristine graphene was first produced by micromechanical cleavage[1]. This method involves two steps, repeatedly splitting graphite crystals by Scotch tape and dissolving the resulted pieces in acetone. Although this method can produce the pristine graphene used for theoretical research, its complicated process and small size

of graphene sheets obtained make the procedure difficult for practical applications. The monolayer graphene also can be synthesized by CVD method at a high temperature under vacuum. However, this method requires an operating temperature as high as 1,000 ℃ along with a hydrocarbon gas flow as precursor and pure hydrogen as a carrier gas, which limits the application range. In the pristine graphene, the charge carriers in this two-dimensional structural channel can change between the electrons and holes with the application of an electrostatic gate, with a minimum density (or Dirac) point characterizing the transition. The zero bandgap of graphene limits achievable on–off current ratios[58].

GO is an insulator after the oxidation process of graphite as part of planar sp^2-hybridized geometry transformed to distorted sp^3-hybridized geometry, which loses the excellent electronic properties of graphite[13]. Therefore, GO has to be reduced to restore the aromatic graphene networks so that the electrical conductivity can be recovered, in which case, most of the oxygen-containing functionalities have to be removed.

2.3 Structure of GO and rGO based material

Understanding the structure and properties of GO is important for discovering the potential applications. Different from the perfect structure of pristine graphene sheets solely consisting of sp^2 carbon atoms in a honeycomb crystal lattice[59], GO has both sp^2- and sp^3-hybridized carbon atoms in the hexagonal ring-based carbon networks where oxygen functional groups produced by Hummer's method are attached [60].

Unfortunately, until now, the structure of GO is still not quite clear because of its partial amorphous character. Structural models of GO proposed in several early researches[61] consisted of a regular lattice composed of discrete repeat units. The widely accepted model, reported by Lerf and Klinowski, was a nonstoichiometric structure (Figure 2.2) in which the carbon plane is decorated with hydroxyl and epoxy (1,2-ether) functional groups[62, 63]. Carbonyl groups are decorated in the GO sheet plane while the carboxylic acids are located at the sheet edge. More details have been revealed by nuclear magnetic resonance (NMR) spectroscopy, which enriches our knowledge of GO structure [64, 65]. Although the presence of epoxy and alcohol groups on the sheet planes are still dominant, the groups of 5- and 6-membered lactols have also been detected on the edges of graphitic platelets. In addition, the tertiary alcohols and esters were found on the sheet surface.

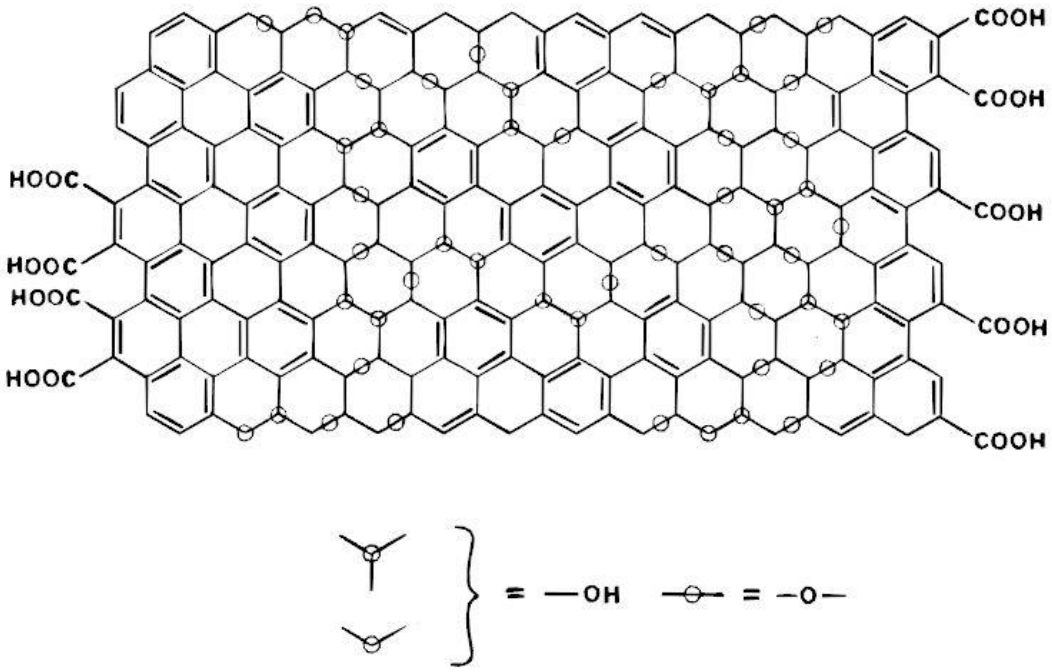

Figure 2.2 The nonstoichiometric structure of carbon plane decorated with hydroxyl and epoxy (1,2-ether) functional groups[62, 63].

Briefly, in the structure of GO, oxidized regions are the disrupted sp^2 conjugated areas where the sp^3 hybridized carbons are covalently bonded with oxygen functional groups, such as hydroxyl, epoxy, and carboxy(Figure 2.3). In another words, the original sp^2 conjugated honeycomb-lattice structure can be interpreted as the unoxidized regions while the sp^3 hybridized carbon clusters are uniformly but randomly displaced on both sides of the graphene plane[13].

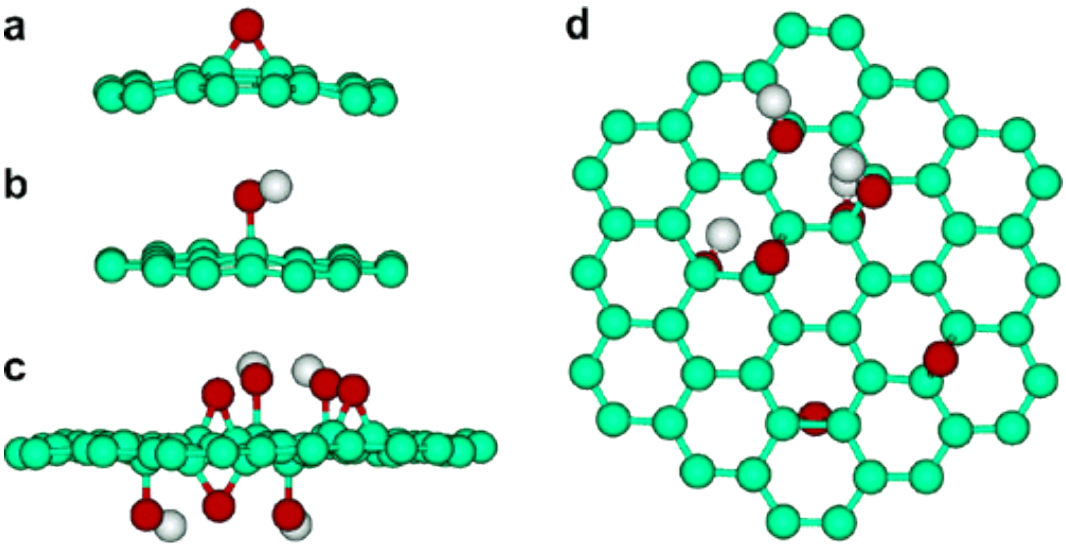

Figure 2.3 (a) An epoxy group. The oxygen atom (in red) decorated on the top of carbon grid with 0.19nm. (b) A hydroxyl group. The top hydrogen atom is 0.22 nm above the carbon grid. (c) Side view of a graphene sheet decorated by functional groups including epoxy and hydroxyl on both sides. The oxygen atom (in red) is 0.19 nm above the carbon grid. The top hydrogen atom (in grey) of the hydroxyl group is 0.22 nm above the carbon grid. (d) The top view of (c). The thickness of GO is 0.78 nm[13].

For an in-depth investigation of GO structure, various detection methods have been employed. Mkhoyan *et al.* used high-resolution annular dark field (ADF) under a scanning transmission electron microscope (STEM) to exam the oxygen distribution on a GO monolayer (Figure 2.4)[40]. According to the analysis of the results, the average roughness of the GO sheet surface is 0.6nm and its distortions from sp^3 hybridized bonds cause the amorphous structure. Atomic force microscopy (AFM) is used to

directly measure the thickness of the single-layer GO as well as the number of layers[66].

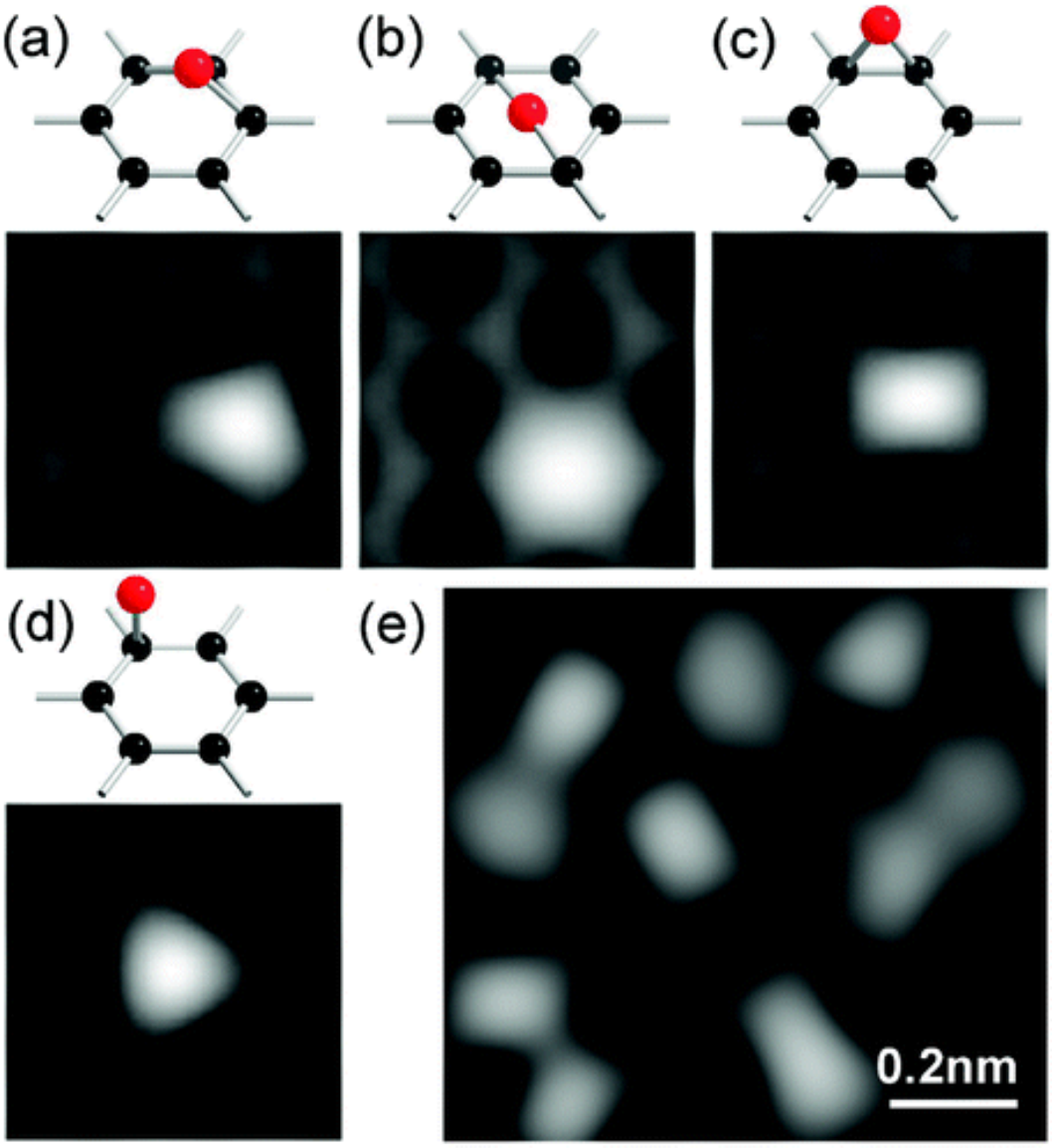

Figure 2.4 schematic of oxygen atoms (in red) attached onto carbon lattice. images of graphene with attached to the surface. (a−d) Simulated STEM-ADF images represent possible cases of oxygen atom bonded to the carbon lattice of graphene. (e) Oxygen atoms randomly attached to both sides of graphene[40].

Scanning tunneling microscopy (STM), another atomic level imaging technique, has been used to observe highly defective and intact regions [66, 67]. The results show that oxygen functional groups introduced by the chemical oxidation process generate the

disordered structure of GO sheets. Therefore, the structure of GO consists both of randomly distributed defective regions and non-oxidized intact areas. By calculating the ratio of defective and intact regions, the degree of functionalization can be estimated. Gómez-Navarro *et al.* reported other possible atomic structures using aberration-corrected high-resolution transmission electron microscopy (HRTEM) [39]. They found disordered regions, including clustered pentagons and heptagons, and in-plane distortions as well as the strain in the surrounding lattice. HRTEM images also exhibit the GO structure with holes, graphitic regions, and disordered regions at the atomic scale [39, 68]. The researchers demonstrated that the holes in GO are formed by the release of carbon monoxide (CO) or carbon dioxide (CO_2) molecules during the oxidation process while some of the honeycomb graphitic structure is preserved due to incomplete oxidation. In addition, the disordered regions consist of oxygen functional groups, such as hydroxyls, (1,2) epoxies, and carbonyls (Figure 2.5)[13].

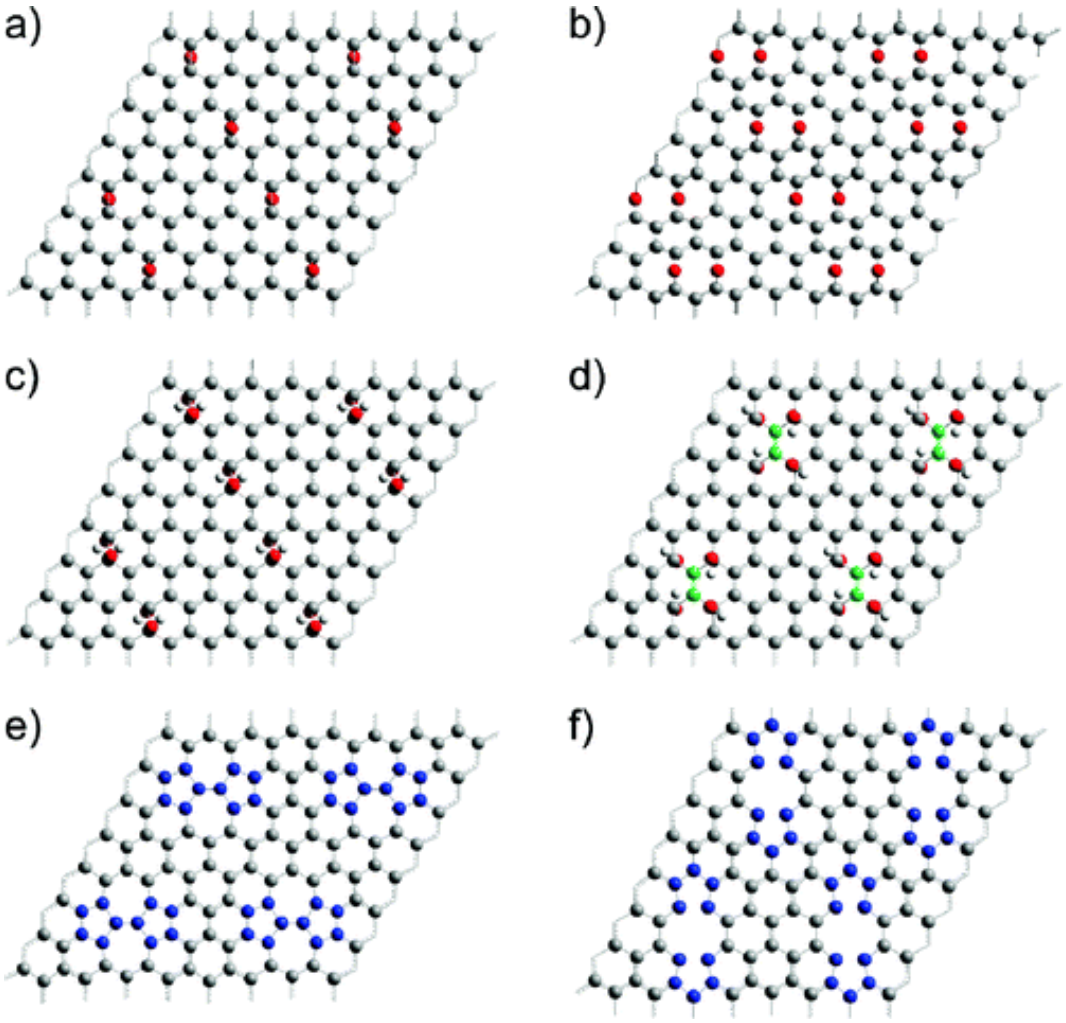

Figure 2.5 The replicated cells with various groups and defective regions. (a) Graphene attached by individual epoxy groups (OX1). (b) Graphene attached by two epoxy groups arranged in a pre-unzipping pattern (OX2). (c) After hydrolysis, graphene attached by 1,2-hydroxyl pair per epoxy group (OH1). (d) Graphene attached by two 1,4-hydroxyl pairs (OH2), forming an isolated double bond (colored green). (e) Graphene with the 5−7−7−5 defect (SW). (f) Graphene with a C_2 vacancy (relaxed 5−8−5 defect structure). [13]

2.4 Structural modelling of GO

The properties of graphene and GO are greatly dependent on the distribution and type of functional groups and defects. Therefore, understanding the inside structure of them arouses great interest. Structural modeling is broadly used to predict the structural evolution during the oxidation and reduction of GO which allows controlling the properties of the obtained graphene.[69]

Although the structure of GO is still unclear today due to its nonstoichiometry property, the researchers reported several models proposed via computer modeling (Figure 2.6). The atomic configuration of GO was first presented by Hofmann[41] with randomly distributed epoxies. Ruess[41] suggested that hydroxyls are also common in GO, moreover, he proposed that O atoms of epoxies connected with the 1,3 site C atoms (1,3-ether) also exist. The skeleton of C atoms is strongly distorted into three dimensional structure of GO by hydroxyls and these 1,3-ethers. In Scholz and Boehm's model[41], ribbons of conjugated carbon backbone and regular quinoidal species were coexisted instead of epoxies. However, Nakajima–Matso's[70] model put the oxygen atoms in epoxies link adjacent layers. Zsabo and Dekeny's[61] model is the integration of Sholz–Boehm and Ruess' models. Lerf-Klinowski's[62] model is commonly used by researchers, in which randomly distributed epoxy (1,2-ether) and hydroxyl are the major functional groups across the carbon layer, and carboxyls, lactones, and carbonyls are mainly distributed at the edge.

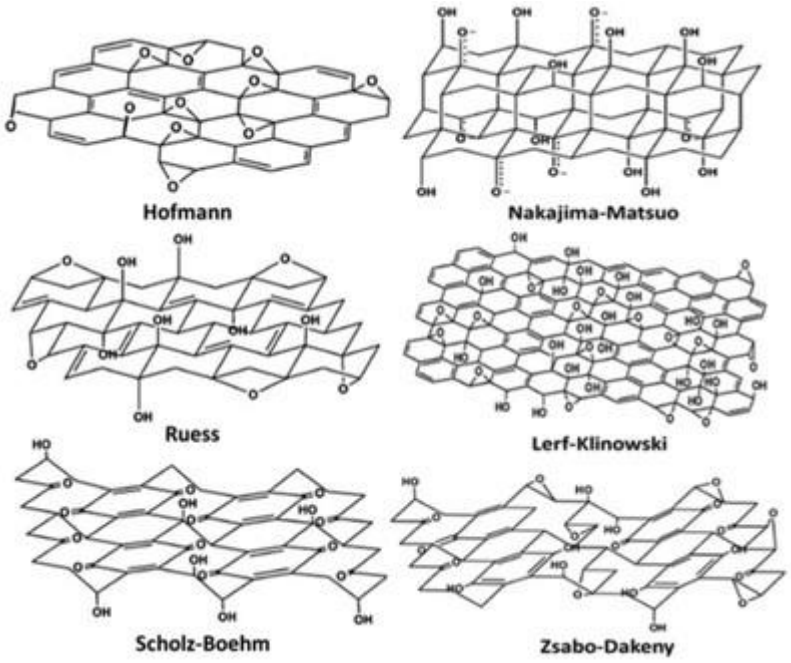

Figure 2.6 proposed models of grapheme oxide[41]

2.5 Properties of GO and rGO based material

GO has a variety of excellent properties including electronic, electrochemical thermal, optical, mechanical properties as well as the chemical reactivity due to the oxygen functional groups attached to its 2D structure surface. The electronic and electrochemical properties will be briefly introduced in this section.

Table 2-1The properties of graphene and other carbon materials[71-75]

Part 1

Carbon allotropes	**Hybridized form**	**Crystal system**	**Dimension**	**Experimental specific surface area ($m^2 g^{-1}$)**	**Density ($g cm^{-3}$)**	**Optical properties**
Graphite	sp^2	Hexagonal	Three	~10–20	2.09–2.23	Uniaxial
Diamond	sp^3	Octahedral	Three	20–160	3.5–3.53	Isotropic
Fullerene (C_{60})	Mainly sp^2	Tetragonal	Zero	80–90	1.72	Non-linear optical response
Carbon nanotube	Mainly sp^2	Icosahedral	One	~1300	>1	Structure-dependent properties
Graphene	sp^2	Hexagonal	Two	~1500	>1	97.7% of optical transmittance

Part 2

Carbon allotropes	**Thermal conductivity ($W m^{-1} K^{-1}$)**	**Hardness**	**Tenacity**	**Electronic properties**	**Electrical conductivity ($S cm^{-1}$)**
Graphite	1500–2000, 5–10	High	Flexible non-elastic	Electrical conductor	Anisotropic, $2–3\times10^4$, 6
Diamond	900–2320	Ultrahigh	–	Insulator, semi-	–
Fullerene (C_{60})	0.4	High	Elastic	Insulator	10^{-10}
Carbon nanotube	3500	High	Flexible elastic	Metallic and semiconducting	Structure-dependent
Graphene	4840–5300	Highest (single layer)	Flexible elastic	Semimetal, zero-gap semiconductor	2000

2.5.1 Electronic Properties

In general, the chemical oxidation process introduces high density electronegative oxygen atoms on the GO basal plane, which gives rise to an energy gap in the electron density of states[76] (Figure 2.7), making GO non-conductive with a sheet resistance (R_s) values of about 10^{12} Ω sq^{-1} or higher[77]. The intrinsic insulating nature of GO is strongly correlated to the amount of sp^3 C–O bonding, resulting in the transport barriers. These defects disrupt the classical carrier transportation among the sp^2 carbon clusters[78]. As a result, R_s can be decreased by several orders of magnitude with the reduction of GO using a variety of chemical and thermal treatments, which transforms the material into a semiconductor or a graphene-like semimetal[79-81]. GO is an electronically hybrid material consisting of both electrically conductive π-states from sp^2 carbon sites and a large energy gap (carrier transport gap) σ-states from sp^3-bonded carbons. The sp^2 and sp^3 fractions ratio changed by reduction chemistry is a powerful way to tune the bandgap and therefore controllably transform GO from an insulator to a semiconductor and to a graphene-like semi-metal[82]. This suggests a great potential for tuning the energy gap by controlling the reduction processes.

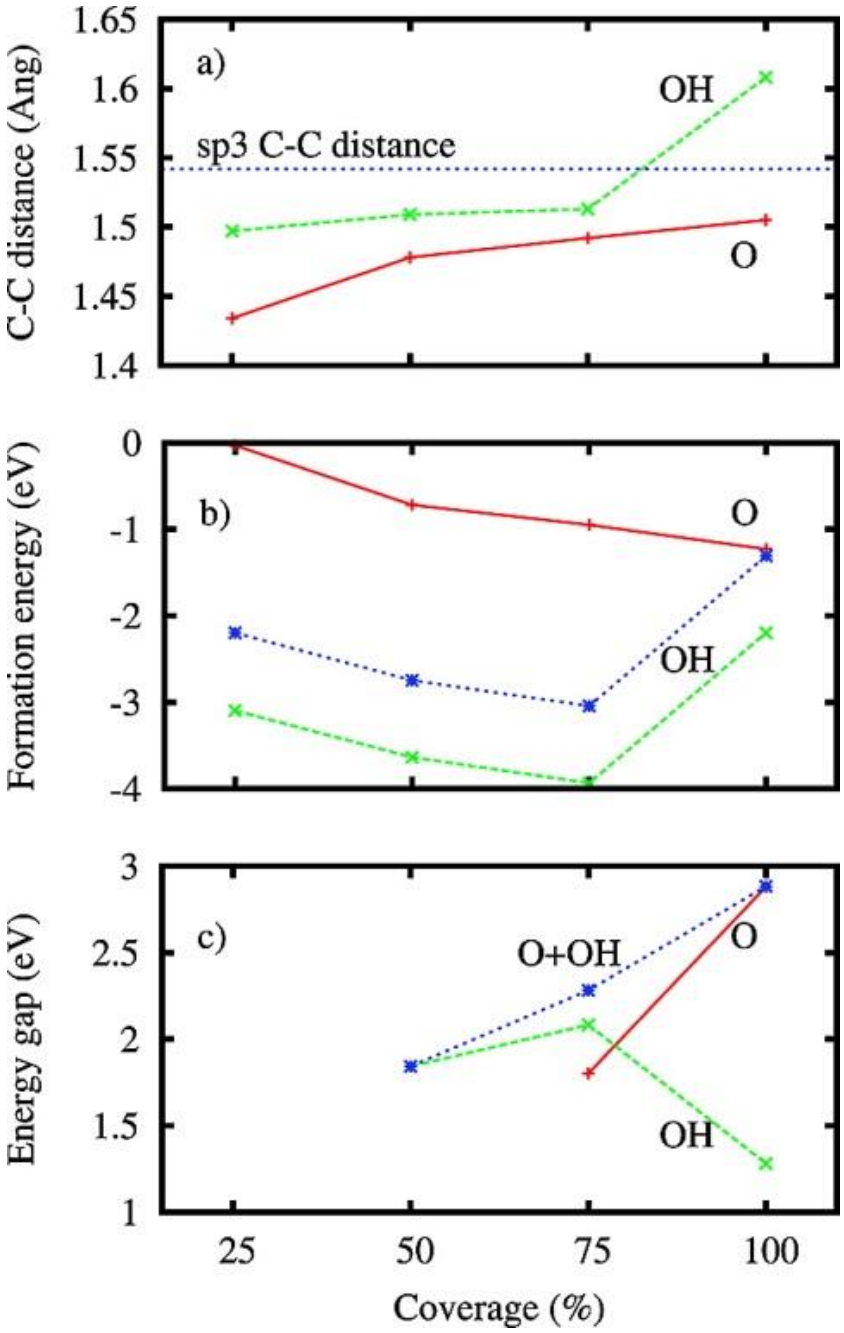

Figure 2.7 Dependence of carbon−carbon bond length (a), chemisorption energy (b), and electron energy gap (c) on oxygen functional groups coverage. The energy gap in c) opens 1.8 eV with 75% coverage and then grows up to 2.9 eV while the coverage increase.

As discussed in section 1.5 and 2.3, the electrical conductivity can be recovered by chemical or thermal reduction methods. Hydrazine was mostly used to reduce the aqueous graphene oxide suspension and gained a paper-like material after filtration which exhibits moderate electrical conductivity at 200 S m^{-1}[11, 15, 83-88]. In order

to enhance the electrical conductivity of hydrazine reduced GO sheets, potassium hydroxide (KOH) solution was added to GO dispersion to functionalize carboxylate anions with K^+ ions at the edges of GO sheets. The electrical conductivity of this KOH modified rGO material achieved ~690 S m^{-1}[89].

The electrical conductivity produced by hydrazine reduction can be further dramatically improved by controlling the pH conditions of the GO dispersion. Li *et al.* reported an rGO paper reduced by hydrazine under the condition of pH 10 showed an excellent electrical conductivity of ~7,200 S m^{-1}[10]. The reduction of a GO dispersion by hydrazine easily results in the aggregation of rGO nanosheets. Therefore, the reduction process was carried out under pH 10 conditions so that the neutral carboxylic groups can be negatively charged to form carboxylate groups, which avoids the agglomeration during the hydrazine reduction process.

On the other hand, although barely studied until recent years, rGO can be achieved by thermal treatment with rapid heating (>2,000 ℃ min^{-1}) up to 1,050 ℃ [13, 18, 19]. During the process, exfoliation of GO can be simultaneously carried out with its reduction, rapid heating instantly generating a high pressure as much as 130 MPa at the interlayers (Figure 2.8). The as-obtained TrGO sheets have a good electrical conductivity in the range of (1–2.3) × 10^3 S m^{-1}. Moreover, GO sheets oxidized by Hummer's method were reported as resulting in partial reduction by a step heat treatment at 200 ℃ for 1 h, followed by increasing the temperature to 300 °C in an Ar

flow. After the thermal annealing, the sample resistance went down to ~ 750 kΩ from insulating [21].

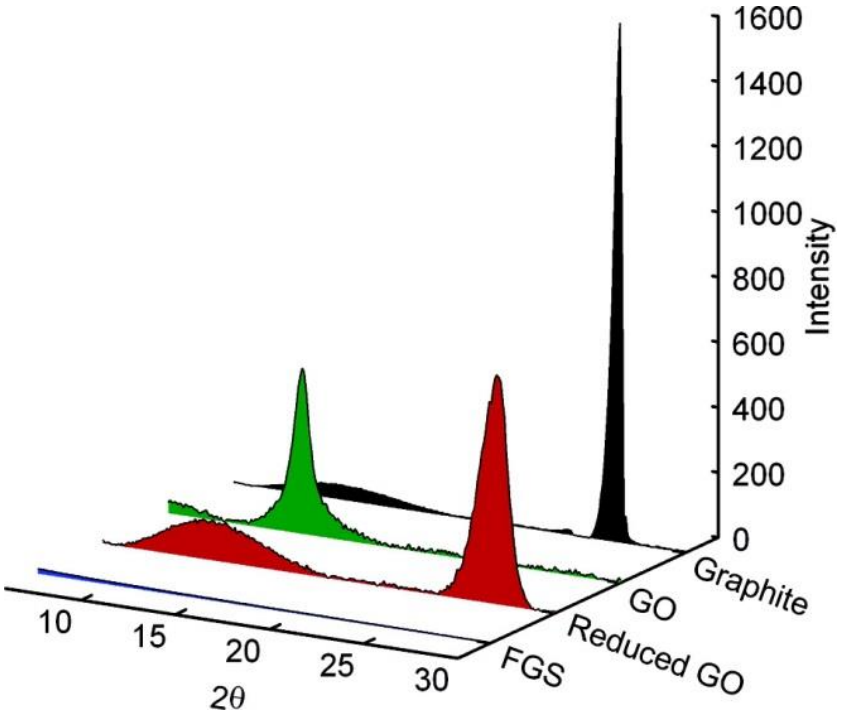

Figure 2.8 X-ray Diffraction (XRD) patterns of graphite, GO, TrGO by slow heating (1 ℃/min), and functionalized single graphene sheet (FGS). The slow heat treatment for GO maintains the initial graphite spacing due to the gas evolution is insufficient to yield a high pressure overcoming the van der Waals force between the layers[19].

2.5.2 Electrochemical Properties

Recently, GO has been is employed as an electrode surface material due to its excellent electrocatalytic properties [90, 91] which have been applied in electrochemical reduction [92-94]. Ramesha *et al.* reported that the reduction of GO occurred at −0.6 V and completed in only one scan. This electrochemically irreversible process was carried out by cyclic voltammetric scanning from 0 to −1 V in a 0.1 M KNO_3 solution[94]. Zhou *et al.* found the participation of H^+ ions in the reduction process under low pH conditions, indicating controlling the pH value of the

buffer solution can improve the potential of the reduction process. The electrical conductivity of as-obtained rGO film was approximately 8500 S m^{-1} and the C/O ratio achieved a high value of 23.9[95]. An *et al.* reduced GO sheets on the anode surface by electrophoretic deposition (EPD) (Figure 2.9) [93]. The as-deposited rGO film has an improved electrical conductivity of 1.43×10^{4} S m^{-1} which is higher than that of the filtration method[93]. GO-based materials can be deposited onto well-defined surfaces through solution processing, which allows sensitive or electroactive species incorporating into an electrochemical system.

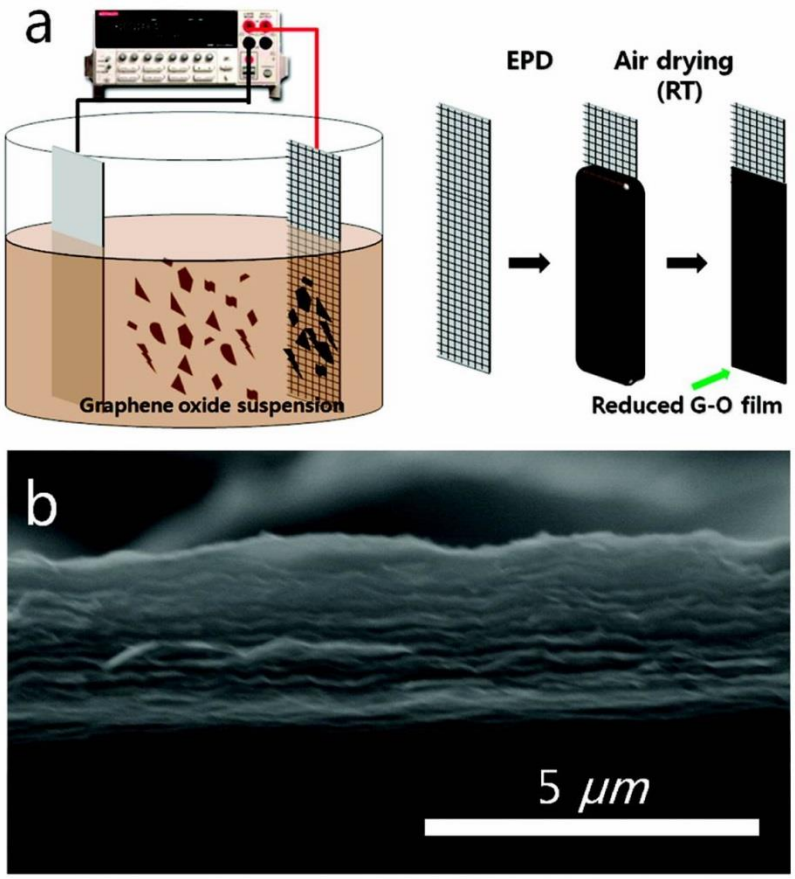

Figure 2.9（a）schematic diagram of the EPD process and (b) cross-sectional SEM image of EPD-GO film[93].

GO can accommodate the active species and facilitate their electron transfer (ET) at electrode surfaces due to its advantageous electron mobility and unique surface properties, such as high specific surface area and one-atom thickness[84, 92]. Moreover, GO has potential application in energy storage devices due to its high electrochemical capacitance with prominent cycle performance[96]. It has been reported that rGO presents much higher electrochemical capacitance and cycling durability than carbon nanotubes (CNTs)[91]. The specific capacitance was found to be ~165 for rGO while CNTs achieved ~86 F g^{-1}. Compared with conventional electrodes, the manufacturing costs for electrochemical applications can be reduced due to the larger surface area-to-volume ratio of GO which decreases the usage of materials in the fabrication of electrode films. Scientists therefore have switched their interest toward GO and rGO applications particularly in electrochemical applications due to their facile synthesis, high dispersibility in a range of solvents and capability of anchoring electroactive species onto the surface.

2.5.3 Chemical activity

GO exhibits a unique chemical activity owing to the oxygen functional groups attached onto its basal plane. These chemically reactive functional groups allow GO chemical functionalization with other groups by covalent or non-covalent binding. The covalent functionalization is typically approached by amidation or esterification of selected small molecules with the carboxyls or hydroxyls on GO sheets [97-99]. The carboxyls can be activated through coupling reactions to make GO soluble in organic

solvents. For functionalizing GO sheets, the materials decorated by carboxyl functional groups react with thionyl chloride ($SOCl_2$) and then coupled with octadecylamine[97]. The epoxy group is another candidate for the covalent functionalization via ring-opening reaction, the amine acting as a nucleophile to attack α-carbon [100, 101]. Wang *et al.* fabricated surface-functionalized GO sheets by attaching octadecylamine with the epoxy groups via a ring-opening reaction [100]. These high-quality GO based nanocomposites can dispersed in organic solvents to form uniform suspension at single layer level. Yang *et al.* reported another modification process of GO by a ring-opening reaction with the epoxy groups[101]. Different from Wang's procedure, the ionic liquid (1-(3-aminopropyl)-3-methylimidazolium bromide; R-NH_2) reacted with the epoxy groups promises an excellent dispersion of resulted GO nanocomposites in DI water, N,N-dimethylformamide (DMF), and dimethyl sulfoxide (DMSO) due to their high polarity.

For non-covalent functionalization of GO, its unoxidized sp^2 networks are used for non-covalent binding including π–π stacking, cation−π and van der Waals interactions. Yang et al. synthesized a hybrid material of doxorubicin hydrochloride (DXR) and GO by non-covalent interactions. The quinone functionality attached on DXR and the sp^2 carbons of GO were dominantly π–π stacked together as well as hydrophobic interactions. Moreover, the results also indicated the existence of strong hydrogen

bonding in both DXR and GO,–OH and –NH_2 groups in DXR as well as –OH and –COOH groups of GO (Figure 2.10 and Figure 2.11)[102].

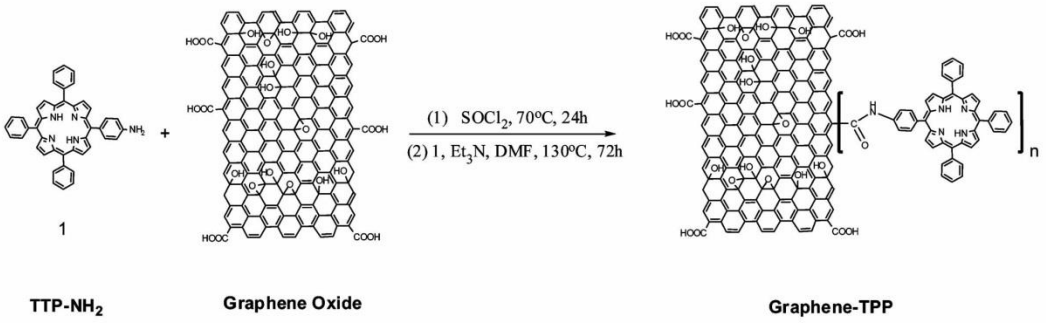

Figure 2.10 Synthesis schematic diagram of Graphene-TPP[102].

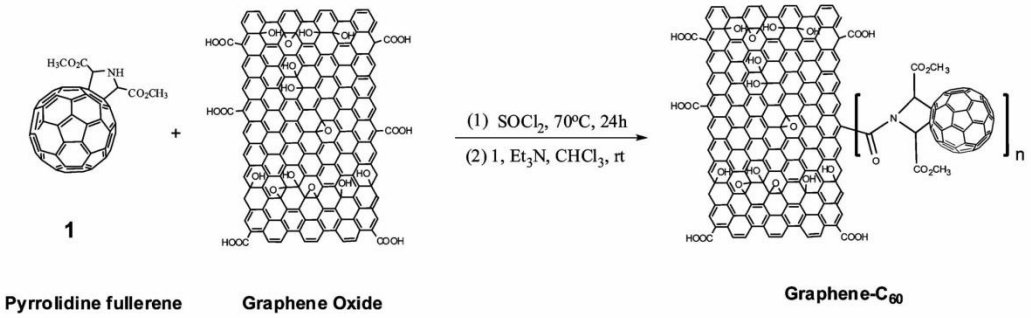

Figure 2.11 Synthesis schematic diagram of Graphene-C_{60}[102].

2.5.4 Wettability of graphene

According to the description of graphene, GO and rGO structures in section 2.3, the hydrophilic GO sheets can be converted to hydrophobic rGO sheets by a chemical reduction process. As a result, the tunable wettability allows rGO great potential in applications such as energy storage, surface coating [103-106], nanopores sequencing[107] and filtration[108] due to its water wettability playing an important role in the fabrication of devices. In addition, the water wettability of rGO affects other properties such as carrier mobility[109], adhesion[110] and charge doping[111]

due to the surface property essentially determining the compatibility of rGO in device fabrication. As a result, the surface of rGO material, which has a hydrophobic property, needs to be modified to prepare hybrid materials[112], electrode coatings[47] or biological applications[113]. Goncalves *et al.* modified the GO surface with oxygen functionalities to obtain reactive sites for growing gold NPs in aqueous suspension[112]. This growth depends on the oxidation degree of the rGO surface as no gold NPs can be obtained on the completely reduced GO surface. Wang *et al.* fabricated solid-state dye-sensitized solar cells with thermally reduced GO as electrodes [47]. After the heat treatment of GO film at 400 ℃, the surface wettability of the resultant rGO film can be tunable from 66.5−69° to 2.2−8.6° by treating with argon plasma for 30 s. Wang *et al.* synthesized rGO electrodes by the Hummers and Offeman Method for selective determination of dopamine[113]. They found a promotional performance of rGO that π–π interaction between two rGO surfaces and dopamine enhance the electron transfer and weakens the oxidation process of ascorbic acid.

The wettability of graphene samples produced by epitaxial growth has recently revealed that most graphene is hydrophobic, indicating a similar wettability to graphite. Shin *et al.* reported that the water contact angle of graphene, which was epitaxially grown on a SiC substrate, was measured at 92 ° and its wettability could not be affected by sample thickness[111]. Kim et al. measured the contact angle of graphene prepared by the CVD method [104]. The multilayer graphene grown on nickel (Ni)

and the monolayer graphene grown on copper (Cu) have slightly different contact angles at 90.4 ° and 93.8 °, respectively. However, the wettability of monolayer graphene deposited on different substrates such as copper, glass and SiO_2 leads to a variety of contact angle at 86 ¶[114], 48.1 ¶[114] and 40 ¶[115], respectively. As a result, compared to free-standing rGO paper, the wettability of monolayer graphene has been affected by the substrate and its quality.

2.6 Synthesis of GO and rGO based material

2.6.1 Chemical oxidation process

2.6.1.1 Brodie Method and Staudenmaier Method

Graphite oxide was first prepared by Brodie when he was researching graphite in 1859[116]. The graphite was oxidized by adding potassium chlorate ($KClO_3$) in a graphite/nitric acid (HNO_3) mixture. The resulting graphite oxide contained carbon, oxygen and hydrogen. After repeatedly washing, drying and re-oxidation, the graphite oxide was light yellow and stable in additional oxidation treatment. Staudenmaier developed Brodie's work by increasing the acidity of the graphite/HNO_3 mixture and slowly adding potassium chlorate solution to the mixture. These two variations improved the quality of the highly oxidized GO and simplified the synthesis process. However, this method required a long time for the addition of potassium chlorate and the as-formed chlorine dioxide gas was hazardous. The mixture of potassium chlorate and nitric acid was previously used in the synthesis of nanotubes [117] and fullerenes[118]. However, the oxidation reagent introduced too many oxygen

functional groups such as carboxyls, lactones, ketones, and released toxic gases of nitrogen dioxide (NO_2) and dinitrogen tetroxide (N_2O_4). Therefore, the oxidation process of graphite still needed to be improved.

2.6.1.2 Hummers Method and modified Hummers Method

Hummer and his colleagues developed the oxidation process for preparation of GO now named Hummer's Method [119]. In this method, a water-free mixture of concentrated sulfuric acid, sodium nitrate and potassium permanganate was mixed and maintained below 45 ℃ for two hours. The final product had a higher oxidation degree than that of the Staudenmaier Method.

However, it was found that the products made by Hummer's Method usually have an incompletely oxidized graphite core with GO shells. As a result, pretreatment was needed for an excellent oxidation with Hummer's Method. Kovtyukhova first introduced a pretreatment for Hummer's Method by adding graphite to the mixture of concentrated sulfuric acid (H_2SO_4), potassium persulfate ($K_2S_2O_8$), and phosphorus pentoxide (P_2O_5) at 80 ℃ for several hours (Figure 2.12)[120]. The pre-oxidized graphite was then washed by repeated filtration and washing with DI water followed by air drying.

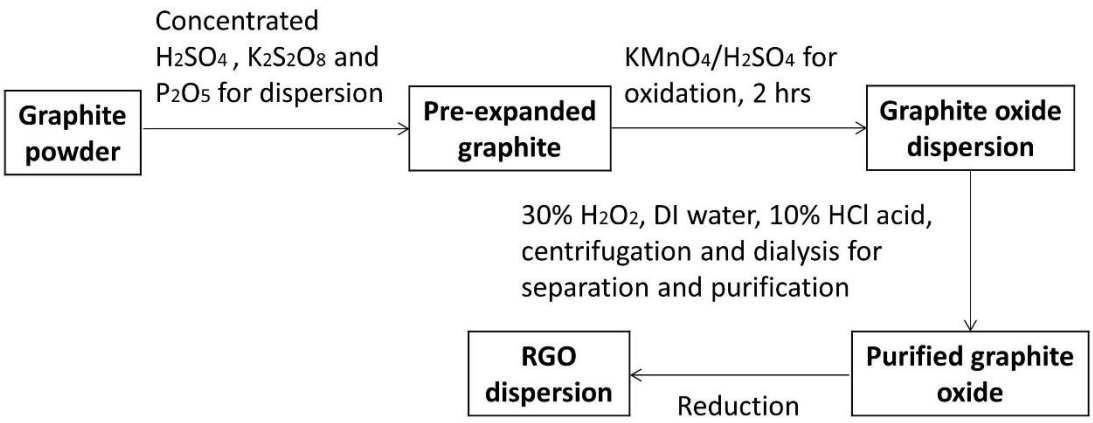

Figure 2.12 A Schematic diagram of GO preparation by modified Hummer's method [120].

Another modified Hummer's Method was reported by Marcano *et al.* in 2010[121]. They added phosphoric acid instead of sodium nitrate as well as increasing the amount of potassium permanganate. In this method, graphite reacted with six equivalents of potassium permanganate ($KMnO_4$) in a 9:1 mixture of H_2SO_4/phosphoric acid (H_3PO_4). This method reduces the toxic hazard due to the absence of sodium nitrate ($NaNO_3$) in the process avoiding the NO_2, N_2O_4 or chlorine dioxide (ClO_2) emission.

In summary, the above mentioned four recipes for graphite oxidation yield the potential for large-scale production of graphite oxide. Today, GO sheets produced by modified Hummer's Method can achieve the ultra-thin thickness of 1 nm, indicating a single layer material. Furthermore, these GO sheets can be fabricated under vacuum filtration as a paper-like material named GO paper.

2.6.2 Reduction strategies of GO

2.6.2.1 Thermal Annealing for Reduction

GO can be reduced by heat treatment without any extra reductant regent, the process being named “thermal annealing reduction”. High temperature heating significantly affects the efficiency of the reduction process in the initial stages [13, 15, 77, 122]. During the high temperature reduction process, CO or CO_2 gases is rapidly evolved at the graphene interlayers due to the oxygen functional groups attached on GO plane formed as gases. Therefore, exfoliation of GO can be simultaneously carried out with its reduction due to rapid heating instantly generating a high pressure as much as 130 MPa at the interlayers, which is enough to isolate GO sheets[19]. The as-obtained TrGO sheets have a good electrical conductivity in the range of $(1–2.3)\times10^3$ S m^{-1}. Wu *et al.* reported an arc-discharge treatment in the preparation of rGO sheets which, due to the high temperature produced by this method, can exfoliat graphite oxide to GO and reduce it to rGO in a short time[122]. The elemental analysis of the resulted rGO shows a high C/O ratio between 15to18 and a sheet electrical conductivity of about 2×10^5 S m^{-1}. Schniepp *et al.* analyzed the reduction level at different temperatures. The C/O ratio was measured at less than 7 when the temperature was under 500 ℃ while the ratio could be increased to over 13 at 750 ℃. [13]. Wang *et al.* reported that the electrical conductivity of rGO sheets prepared by thermal reduction at 500 ℃ was only 50 S/cm. However, the electrical conductivities could be increased

to 10,000 S m^{-1} at 700 ℃ and 550 S cm^{-1} at 1100 ℃. The electrical conductivity of TrGO sheets fabricated at different temperatures is shown in Figure 2.13[47].

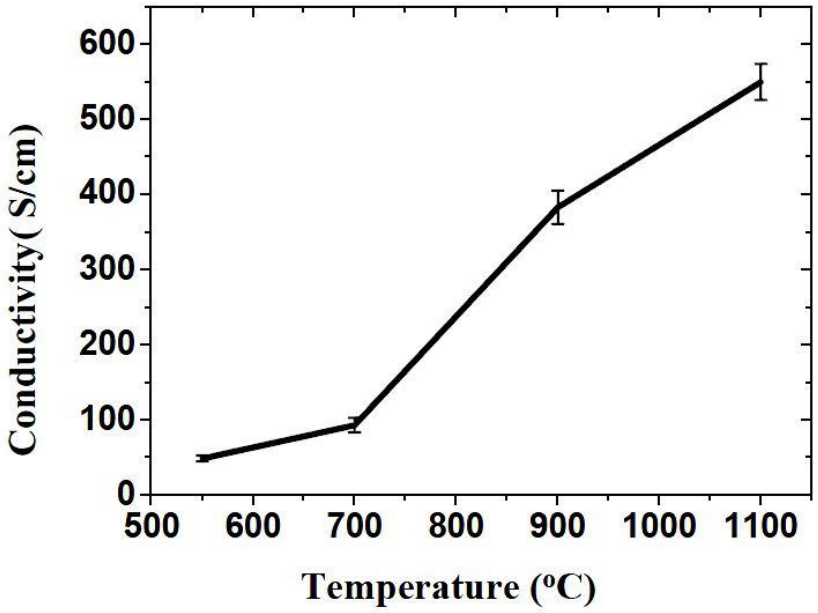

Figure 2.13 The electrical conductivity of rGO sheets produced by thermal annealing increases from 49, 93, 383 to 550 S/cm at the annealing temperature of 550 ^{O}C, 700 ^{O}C, 900 ^{O}C and 1100 ^{O}C, respectively[47].

Annealing atmosphere is another crucial factor for the thermal annealing reduction of GO. Normally, the thermal reduction process is carried out under vacuum[77] or a protection gas[47] in order to cut off the oxygen gas rapidly generated during the high temperature heating process [18, 47, 123, 124]. Becerril *et al.* suggested thermally reducing GO sheets at 1000 ℃ under high vacuum($<10^{-5}$ Torr) as the fresh rGO easily reacts with the residual oxygen functional groups[77]. The resulted TrGO has a low sheet resistance about $10^{2}-10^{3}$ Ω sq^{-1} and a high transmittance of 80% under 550 nm light.

An inert gas can also facilitate the reduction process. For example, the reducing gas of H_2 introduced to the thermal reduction process can lower the heating temperature due

to its excellent reducibility. Wu *et al.* introduced a gas mixture of Ar/H_2 (1:1) in the thermal process to reduce GO sheets at 450 ℃ for 2 h. The as-prepared rGO sheets has a high electrical conductivity of $\sim 1 \times 10^5$ S m^{-1} with a C/O ratio of 14.9. Li *et al.* reported that the thermal treatment under a low-pressure ammonia atmosphere (2 Torr NH_3/Ar (10% NH_3)) simultaneously reduced GO and doped nitrogen on as-formed rGO sheet plane[124]. The highest doping level of ~5% N was recorded at 500 ℃ by thermal annealing GO in NH_3. Moreover, rGO sheets clearly exhibited n-type electron doping behavior, which could be beneficial for electronic device fabrication. Recently, Lopez *et al.* pointed out that vacancies in the rGO plane could be partially "repaired" by exposing rGO sheets to a carbon source such as ethylene at a high temperature (800 ℃), a similar condition used for CVD growth of single-walled nanotubes SWCNTs[125]. The sheet resistance of repaired rGO sheets can be decreased to 28.6 kΩ sq^{-1} (or 35,000 S m^{-1}) [126]. Su *et al.* reported a similar defect-healing process by functionalization of rGO sheets with aromatic molecules during heat treatment. The resultant modified rGO has denser graphitic regions and good electrical conductivity at 1.31×10^5 S m^{-1} [127].

2.6.2.2 Low temperature thermal annealing for reduction

Recent experimental research shows that many oxygen functional groups are not difficult to remove at low temperatures. Actually, the deoxygenation processes of GO can even be approached at 200 ^{O}C.

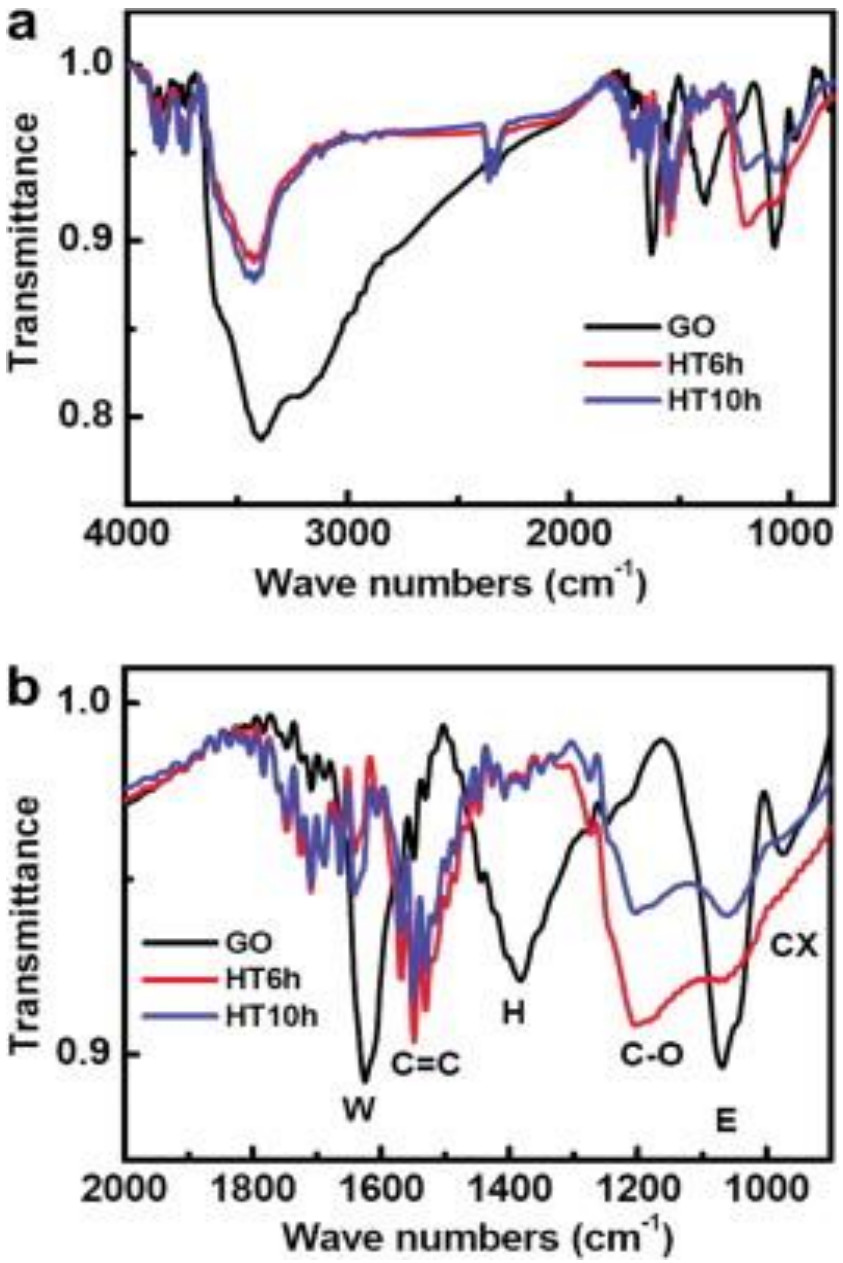

Figure 2.14 FTIR spectra of GO and rGO annealed for 6 hours and 10 hours, respectively, in the (a) range of 800-4000 cm^{-1} (b) range of 900-2000 cm^{-1}. The W, H, E, and CX represent FTIR peaks of water, hydroxyl, epoxide, and carboxyl, respectively. Peaks C=C and C–O represent the bond stretching vibrations [128].

Jeong *et al.* demonstrated that most oxygen functionalities can be removed by low temperature thermal annealing at 200 ℃ in a low-pressure argon atmosphere (550 mTorr) [128]. Fourier transform infrared spectroscopy (FTIR) was used to investigate the as-formed rGO material which had been annealed for 6 h, as shown in Figure 2.14.

The peaks of epoxy and carboxyl groups are found to apparently decrease while the hydroxyl peak completely disappears. After low temperature annealing for 10 h, the epoxy and carboxyl peaks decrease dramatically and a C/O ratio of around 10 is achieved.

2.6.2.3 Chemical reduction

GO can also be reduced by chemical reagents through chemical methods. Normally, the reduction is carried out at room temperature followed by a low temperature annealing, which is different from thermal annealing reduction. Chemical reduction is therefore another procedure for the mass production of rGO sheets.

The reduction of GO using hydrazine which was first reported by Stankovich *et al.* [11] and[14] is the method mostly used today [14, 22, 43, 67, 117, 118, 129-137]. Hydrazine reduction is started by adding the reducing reagent to a GO dispersion which is usually prepared by Hummer's Method. During the reduction process, partly reduced GO sheets are aggregated due to the increase of hydrophobility. Fernandez-Merino *et al.* reported a high electrical conductive rGO fabricated by hydrazine reduction with a C/O ratio of 12.5[130]. In order to facilitate the applications of hydrophobic rGO material, the surfactants including soluble polymers[14] or ammonia[129] are added to the dispersion to maintain its colloidal state. The resultant colloidal dispersion of rGO sheet based composites can be filtered to form rGO based composite films[129].

Apart from the above introduced reduction methods for rGO, Table 2-2 lists some other reduction process and the resultant properties of rGO.

Table 2-2 Comparison of the different reduction methods of GO.

Reduction method	**Electrical conductivity(S/m)**	**C/O ratio**	**Ref. no.**
Hydrazine hydrate	200	10.3	[11]
Hydrazine reduction in colloid state	7200	NA[b]	[129]
150 mM $NaBH_4$ solution, 2 h	4.5	8.6	[138]
Hydrazine vapor	NG	～8. 8	[15]
Thermal annealing at 900℃, UHVa	NG	～14.1	
Thermal annealing at 1100℃, UHV	～10^5	NA	[77]
Thermal annealing at 1100℃ in Ar/H_2	72700	NA	[47]
Multi-step treatment: (I) $NaBH_4$ solution (II) Concentrated H_2SO_4 180℃, 12 h (III) Thermal annealing at 1100℃ in Ar/H_2	 (I) 82.3 (II) 1660 (III) 20200	 (I) 4.78 (II) 8.57 (III) >246	[65]
Vitamin C Hydrazine monohydrate Pyrogallol KOH	7700 9960 480 0.1910	12.5 12.5 NA NA	[130]
55% HI reduction	29800	>14.9	[139]

[a] UHV: ultra high vacuum.

[b] NA: not available.

2.6.3 Functionalization with NPs

Because of the unique structures and excellent properties of GO-based nanocomposites, the numerous promising applications in the field of electrochemistry are apparent and research into these remarkable and intriguing materials has become very popular nowadays. The unique properties of GO nanosheets make GO-based nanocomposites extremely useful as the NP support due to their high surface area,

which is essential for the dispersion of the NPs as well as the electrochemical activities. The GO-supporting materials maximize the capability of the nano-scale surface area for electron transfer and provide for better mass transport of the electroactive sites on the electrode surface. Additionally, the collecting and transferring of the electrons to the collecting electrode surface are promoted by the conductive GO support. Also, nanoscale composite electrodes could be realized by the functionalization of GO with NPs. The improved performance of GO-based nanocomposite-modified electrodes, such as excellent catalytic activity, enhanced mass transport, high effective surface area, and control over the electrode microenvironment, shows superior properties over macroelectrodes in electrochemical applications. Moreover, in some functional electrochemical applications, the combination of GO with NPs present the capability of providing additional properties.

Earlier researches were focused on the preparation of functional GO/inorganic nanocomposites derived from the GO sheets decorated with inorganic NPs, such as metal NPs and MO NPs, which are used in electrochemical sensing, catalysis, and fuel cells. There are different physical and chemical approaches to preparing these functional metal or MO/GO nanocomposites. In situ chemical reduction process [23, 48], electrochemical synthetic processes[135, 140], impregnation processes[37], a self-assembly approach[141] and ultrasonic spray pyrolysis[49] are typical physical attachment approaches. Among these methods, MO NPs dissolved in GO dispersion

for preparation of GO-based nanocomposites is widely used due to the hydrophilic property of GO.

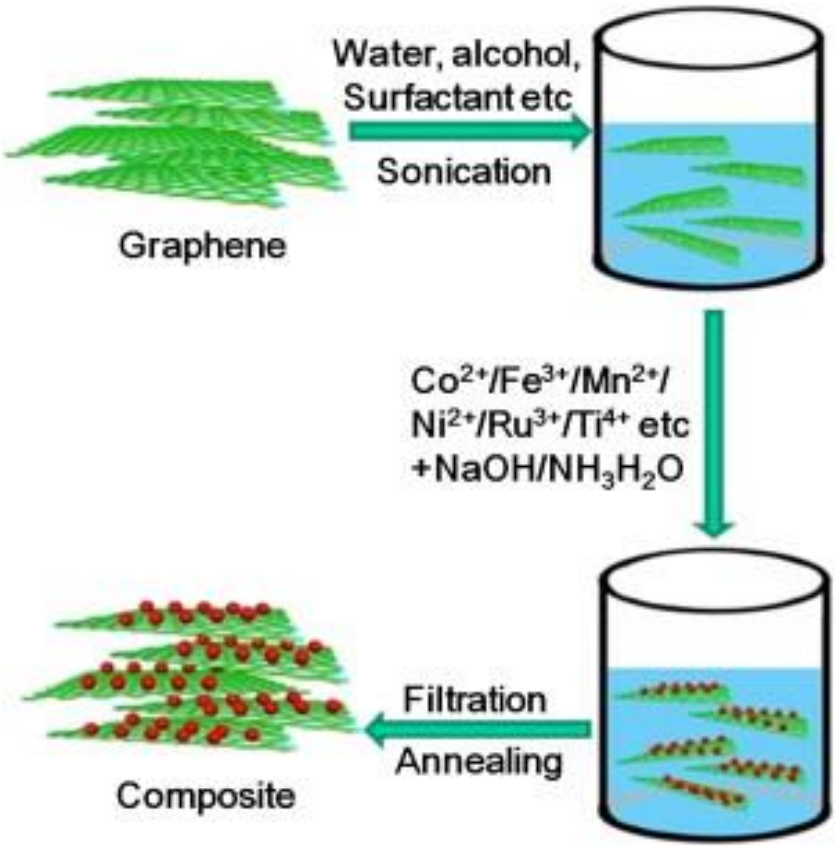

Figure 2.15 A general solution strategy for fabrication of MO/ rGO composites [142].

For instance, Dong *et al.* used ethylene glycol reduction to deposit platinum (Pt) and platinum–ruthenium (Pt–Ru) NPs onto surfaces of GO nanosheets[143]. Their results demonstrated that for both methanol and ethanol oxidation used in fuel cell applications, GO acts as a catalyst support on the electrocatalytic activity of Pt and Pt–Ru NPs. As a catalyst support, GO showed efficient enhancement of the electrocatalytic activity of Pt and Pt–Ru NPs for the oxidation of methanol and ethanol into CO_2 comparing to carbon black. To improve the cyclic performance and lithium storage capacity, Paek *et al.* prepared SnO_2/GO nanoporous electrodes with

three-dimensionally delaminated flexible structures by using an exfoliation-reassembly method[144]. Their experimental results suggest that the dispersed GO nanosheets were reassembled and homogeneously distributed in the ethylene glycol solution among the loosely packed SnO_2 NPs. The volume expansion could be controlled by the insertion of lithium in the SnO_2/GO nanoporous electrodes which resulted in excellent cyclic performances.

In order to establish another platform for electrochemical applications, quantum dots (QDs) have also been used to functionalize GO [145-147] as well as NPs such as Prussian blue [148], metal hydroxides[149], and polyoxometalates[150]. By introducing the in situ growth of QDs on noncovalently functionalized rGO, QD-sensitized rGO nanocomposites can afterwards be used as an efficient platform in photoelectrochemical applications. Moreover, to functionalize the GO-based electrodes for electrochemical applications, others, for instance, Chen *et al.* fabricated rGO–$Co(OH)_2$ nanocomposites in a water–isopropanol system which showed significantly improved electrochemical performance of $Co(OH)_2$ after deposition on rGO sheets[151].

2.6.4 Size effect of quantum dots and nanoparticles

Quantum dots (QDs) have smaller radii than the bulk exciton Bohr radius constituting a class of materials between molecular and bulk forms of matter. Quantum confinement between the electron and hole in the material leads to an increase in the effective bandgap with decreasing crystallite size. Therefore, their optical absorption

and emission blue shift to the higher energies wavelength as the size of the dots gets smaller (Figure 2.16). The structural studies indicate that the bulk crystal structure and lattice parameter can be retained although the nanocrystallites are not completed in the bulk materials.

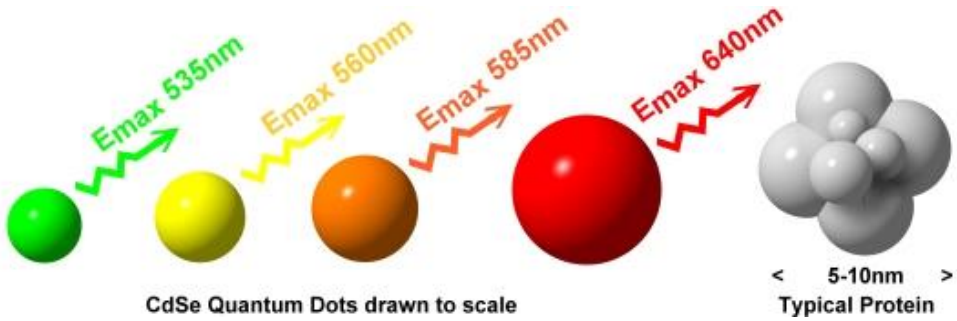

Figure 2.16 Size dependent fluorescence spectrum of QDs[152]

The light also can irradiate the small spherical metallic nanoparticles to produce the conduction electrons in the oscillating electric field[153]. Figure XX shows that the electron cloud distributed to the nuclei oscillates relative to the nuclear framework with a restoring force arises from Coulomb attraction between electrons and nuclei. The resulted oscillation frequency is affected by four electron properties: the density of electrons, the effective electron mass, and the size and the shape of the charge distribution.

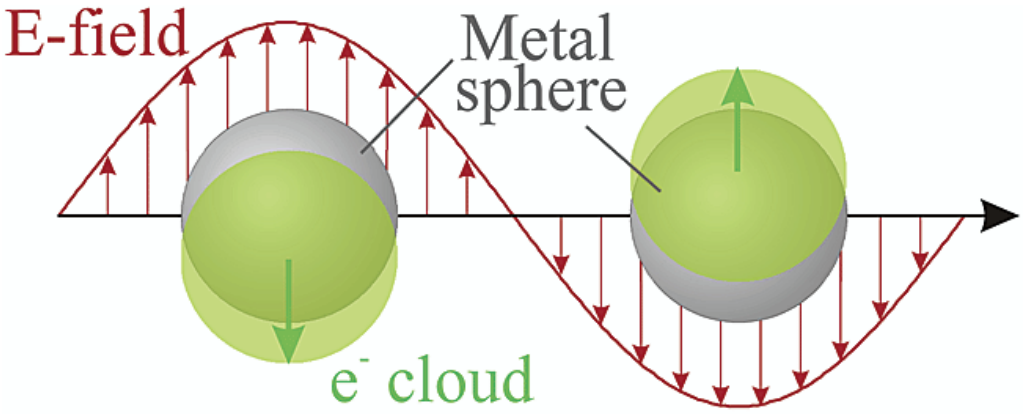

Figure 2.17 Schematic of oscillation for a sphere nanoparticle, showing the displacement of the conduction electron charge cloud relative to the nuclei[153].

2.7 Functionalization and Application for rGO based material

2.7.1 Introduction

As with graphene, recent researches indicate that GO based materials have great potential for various applications such as gas- or bio-sensors [72], nanogenerators [154], field emission devices [155], chemical sensors [87], catalysts [156], dye-sensitized solar cells [47], organic solar cells [157], photocatalysts [158], and hydrogen storage [159], etc.(Figure 2.18).

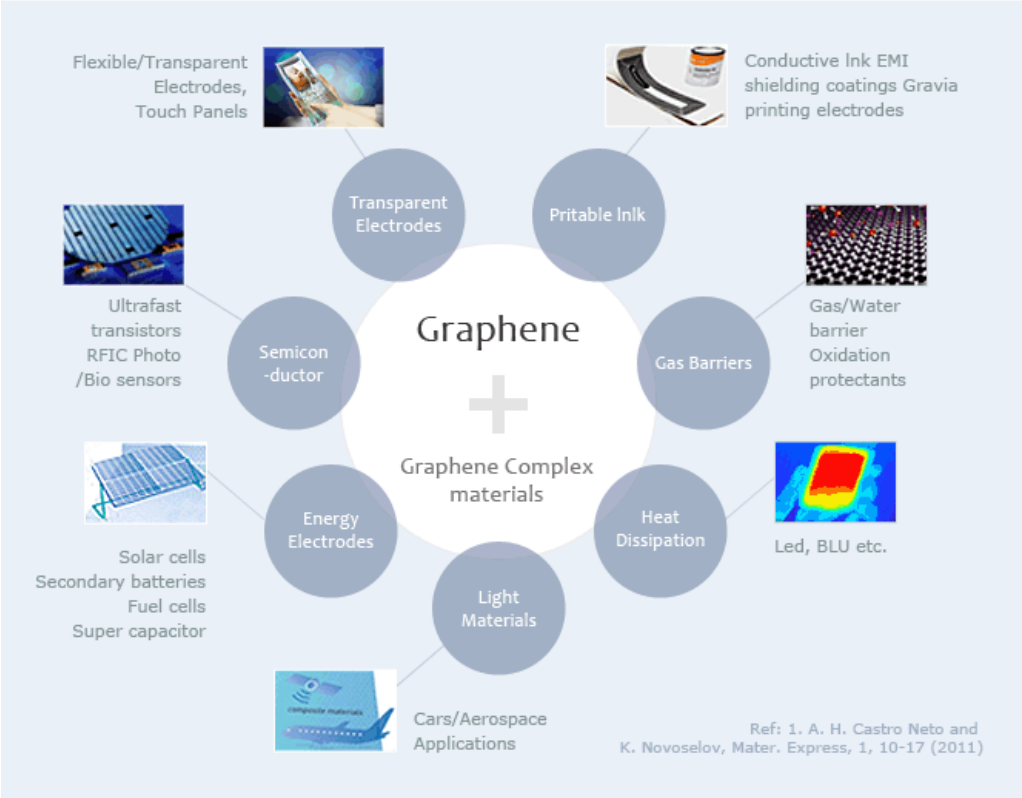

Figure 2.18 The potential applications for graphene and its complex materials[160].

Among these applications, GO-based electrodes fabricated for electrochemical applications by reliable and low-cost methods have attracted great interest due to their excellent properties as discussed in section 2.5. For example, Large-area rGO sheets have the potential to replace indium tin oxide (ITO) in display applications, such as touch screens or organic light-emitting diodes (OLED), if mass production can be achieved due to its transparency and electrical conductivity [161, 162]. Moreover, compared to the frangible and rigid indium tin oxide (ITO), rGO is competitive in flexibility and processability for fabrication of electronic devices. RGO based nanocomposites fabricated by encapsulating metal or MO particles as well as polymers have performed efficiently in multifunctional materials to enhance the volume expansion of pure metal or polymer electrodes[163-165].

RGO material has already been accepted as an alternative anode material in lithium ion storage with large capacities of lithium[166]. In addition, the high electrical conductivity as well as electron and lithium ions mobility of rGO sheets are quite compatible for diffusion of lithium ions in electrodes. In addition, C-C bonds of sp^2 region in rGO sheet plane allow a metastable nanostructure during the electrochemical process between the electrodes. As a result, we will briefly introduce the development of rGO based electrodes in LIBs as well as its functionalization with MO NPs and the performance of resultant hybrid materials.

2.7.2 RGO based electrodes for LIBs

RGO is a new promising anode material in LIBs because of its unique physical and chemical properties including:

(i) Excellent electrical conductivity to graphitic carbon;

(ii) A broad electrochemical window. This is a crucial element in enhancing energy density which is proportional to the square of the window voltage;

(iii) The possibility to manufacture flexible electrodes due to the flexibility of the structure;

(iv) The thermal and chemical stability allow it to be used in harsh environments;

(v) High surface area. The specific surface area of monolayer pristine graphene is around 2620 $m^2 g^{-1}$ theoretically;

(vi) The ultrathin thickness distinctly shortens the diffusion distance of ions;

(vii) The high surface-to-volume ratio offers more active sites for electrochemical reactions and/or ion adsorption;

(viii) Abundant surface functional groups make it hydrophilic in aqueous electrolytes, but also provide binding sites with other atoms or functional groups which is important for electrode fabrication of LIBs;

(ix) Cost effective. Mass production of rGO prepared from graphite through chemical oxidation and exfoliation in DI water or polar solvents followed by chemical reduction of GO is relatively low cost, which is crucial for practical applications.

As a commercially used anode material, graphite suffers from its theoretical capacity of 372 mAh g^{-1}, which limits its application in high energy capacity LIBs[167]. In order to increase the energy capacity, efforts have been put into developing other high-capacity carbonaceous materials, such as CNTs [168], carbon nanofibers[169], and hierarchically porous carbons[55]. Yoo *et al.* first reported the specific capacity of rGO sheets could reach 540 mA h g^{-1}which is much higher than that of graphite[166]. They also pointed out that lithium storage properties could be affected by the layer spacing between the rGO individual sheets. By embedding CNTs or fullerene macromolecules into rGO layers, the resultant hybrid materials have higher capacities of 730 and 784 mAh g^{-1} due to the additional sites and the increased interlayer distance provided by embedded carbon materials for lithium ion storage [166]. Wang *et al.* demonstrated a preparation method for flower-like rGO which can improve lithium storage capacity to 650 mAh g^{-1} and cyclic stability of 460 mAh g^{-1} after 100

cycles. Characteristic results indicate that the lithium ions are stored on both surfaces of rGO sheets as well as its edges and covalent sites [170]. Guo *et al.* presented a relatively highly reversible capacity of 672 mA h g^{-1} and good cyclic performance of rGO and explained that numerous functional groups and defective regions on rGO plane can allocate the lithium ions to improve the capacity and cyclic performance [51]. Lian *et al.* reported a high-quality fewer layers (~4 layers) rGO with a large specific surface area (492.5 m^2 g^{-1}) presenting a high initial capacity of 1264 mA h g^{-1} at a current density of 100 mA g^{-1} [54]. The high capacity is approached by storing the lithium ions on its large surface area where many disordered structures including edges, nanopores and curling areas open a broad electrochemical window (0.01–3.5 V) for the storage process. Pan *et al.* systematically investigated the lithium storage affected by structural changes, including surface functional groups, interlayer spacing, specific surface area, defects or degree of disorder, in different chemical reduction process for fabrication of rGO, such as hydrazine reduction, electron beam irradiation, and low-temperature pyrolysis. The results, as shown in Figure 2.19, demonstrated that the intensity ratio between D band and G band of Raman spectra (I_D/I_G) is the primary characteristic to evaluate the reversible capacity and lithium storage properties. In addition, the edges and defects extend the lithium storage sites which allow a better performance in reversible capacity [56].

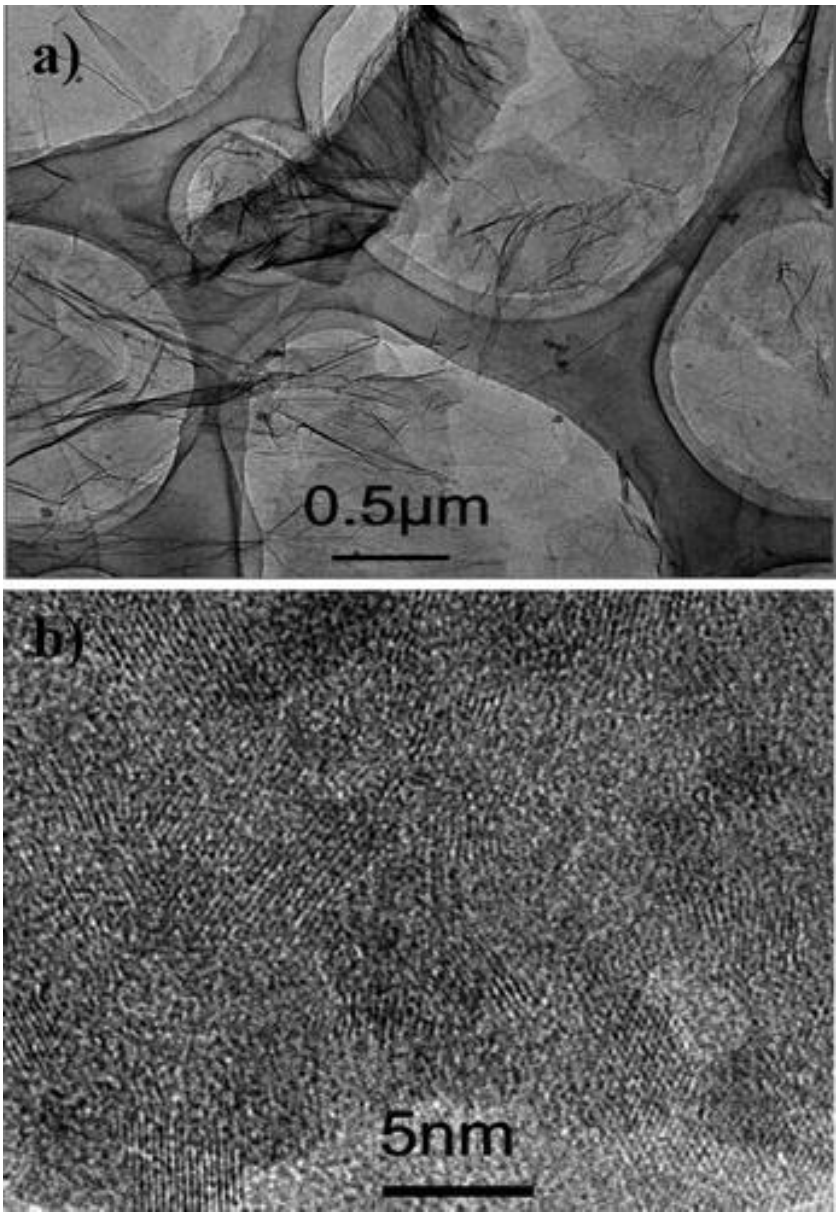

Figure 2.19 (a) Low-magnification TEM and (b) HRTEM images of the electron-beam-reduced GO

This research has revealed the attractive performance of rGO sheets used as electrode materials for LIBs although the detailed mechanisms of lithium storage are still not clear. Due to the variety of possible lithium ion storage sites in a rGO electrode, lithium ions can be stored in the nanopores/cavities and defective regions as well as the layer edges and covalent sites in the form of LiC_6 or react with oxygen functional groups attached on the rGO plane.

2.7.3 MOs based electrodes for LIB

Due to having more than twice the capacity of graphite, MOs have been accepted as the electrode materials for LIBs. [57, 171]. The electrode reaction mechanism of MOs can be divided into three groups: conversion reaction(1), Li-alloy reaction(2), and Li insertion/extraction reaction(3). The mechanism of the conversion reaction is:

$$M_xO_y + 2y^-e + 2y^+Li \leftrightarrow x^0[M] + yLi_2O \quad (1)$$

Where M is a metal, such as Sn, Fe, Cu, Co, Ni, and Mn. Homogeneous distribution of metal NPs are embedded in a Li_2O matrix in the final product. Nevertheless, the poor cyclic performance caused by huge volume expansion and severe aggregation of MOs during charge/discharge significantly hinder this approach in practical application of LIBs. Moreover, large voltage hysteresis is needed between charge and discharge and poor energy efficiency is displayed. The reaction(2) mechanism of Li-alloy is:

$$M + z^-e + z^+Li \leftrightarrow Li_zM \quad (2)$$

For instance, Li_2O and metallic tin is formed after the conversion reaction mentioned above of a tin-based oxide, then lithium ions can be stored and released by the in-situ formed tin distributed in Li_2O due to Li–Sn alloying/de-alloying reactions up to the theoretical limit of $Li_{4.4}Sn$ corresponding to a theoretical reversible capacity of 782 mAh g^{-1} based on the mass of SnO_2 [57]. However, due to large volume changes (up to 300%) during charge/discharge process, it has poor cyclic performance which leads to mechanical disintegration and the loss of electrical connection of the active material

from current collectors. The insertion and extraction process of Li^+ from the MO lattice structure can be described as follows(3):

$$MO_x + y^- e + y^+ Li \leftrightarrow Li_y MO_x \quad (3)$$

For example, following a typical Li intercalation process, TiO_2 is a common anode MO with a volume change smaller than 4% in the reaction(4):

$$TiO_2 + xLi^+ + xe^- \leftrightarrow 4Li_x TiO_2 \ \ (0 \le x \le 1) \quad (4)$$

Small lattice change during the lithium intercalation and extraction process guarantees the structural stability and cycling life. The intercalation potential of lithium is about 1.5 V, in that case, the avoidance of electrochemical Li deposition intrinsically maintains the safety of the electrode. However, the slow ionic and electronic diffusion of bulk TiO_2 leads to low specific capacity, poor lithium ionic and electronic conductivity as well as high polarization. Nevertheless, the capacity of lithium ions can be enhanced by reacting with metallic/semi-metallic elements and metal alloys, such as Si, Ge, Bi, Sn, Cu–Sn, and Ni–Sn.

2.7.4 MO/rGO based electrodes for LIBs

According to the research described in sections 2.7.2 and 2.7.3, the use of MO/rGO composites is expected to be an efficient and practical approach to improving the electrochemical performance of LIBs (Figure 2.20).

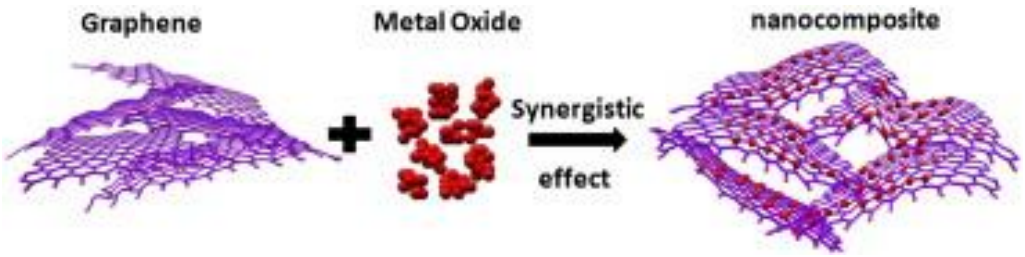

Figure 2.20 Schematic of the preparation of MO/graphene composites with synergistic effects between these two components [142].

RGO sheets are proved to be successfully anchoring MO NPs on its plane edges and surfaces to form MO/rGO nanocomposites. However, the uncontrolled agglomeration and growth of large particles during the preparation cause poor properties of resultant composites. In order to improve the properties of MO/rGO, it is necessary to synthesize MO nanostructures with controlled size, uniform morphology, good crystallinity and high dispersion. As a result, MO/rGO composites are normally prepared by dissolving MO NPs into a GO dispersion. This solution strategy results in a uniform distribution of MO NPs on rGO sheets with controllable size, shape and crystallinity, which is preferred in LIBs.

Table 2-3 lists the research on a variety of MO/rGO composites and their structural and electrochemical properties.

Table 2-3 The electrochemical properties of MO/rGO composites for LIBs [172].

G/MO	Performance improvements	Ref. no.
G/SnO_2	A specific capacity of 810 mA h g^{-1}, 70% capacity retention after 30 cycles	[31]
	A specific capacity of 765 mA h g^{-1} in the first cycle, maintained a capacity of 520 mA h g^{-1}after 100 cycles	[173]
	A reversible capacity of 862 mA h g^{-1}, maintained 665 mA h g^{-1} after 50 cycles	[174]
	An initial reversible capacity of 786 mA h g^{-1}, 71% capacity retention after 50 cycles	[175]
	A reversible capacity of 634 mA h g^{-1} with a coulombic efficiency of 98% after 50 cycles	[52]
	The capacities were 673, 424, 295, 190 and 120 mA h g^{-1} at 130, 450, 1400, 6000 and 8000 mA g^{-1}, respectively	[160]
	600 mA h g^{-1} after 50 cycles and 550 mA h g^{-1} after 100 cycles, 550 mA h g^{-1}at the 2 C rate, and 460 mA h g^{-1} at as high rate as 5 C rate	[176]
	A reversible capacity of 838 mA h g^{-1}, the charge capacity of the hybrid electrode remains at 510 mA h g^{-1} after 20 cycles	[177]
	A reversible specific capacity of 1304 mA h g^{-1} at 100 mA g^{-1} and the reversible capacity was still as high as 748 mA h g^{-1} at	[178]

	1000 mA g^{-1}	
	A charge capacity of 840 mA h g^{-1} (with capacity retention of 86%) after 30 cycles at 67 mA g^{-1}, and it could retain a charge capacity of about 590 mA h g^{-1} at 400 mA $g^{-1}$and 270 mA h g^{-1} at 1000 mA g^{-1} after 50 cycles	[179]
	A reversible capacity of 518 mA h g^{-1} after 50 cycles at 400 mA g^{-1}	[180]
	A capacity of 2140 mA h g^{-1} and 1080 mA h g^{-1} for the first discharge and charge at a current density of 50 mA h g^{-1}, and good capacity retention with a capacity of 649 mA h g^{-1} after 30 cycles	[181]
	A stable capacity of 775.3 mA h g^{-1} after 50 cycles at 100 mA g^{-1}	[182]
G-CNT/ SnO_2	The capacities of 345 and 635 mA h g^{-1} can be obtained at 1.5 and 0.25 A g^{-1} and the flexible SnO_2–G–CNT papers present a stable capacity of 387 mA h g^{-1} at 0.1 A g^{-1} after 50 cycles	[183]
G/Co_3O_4	Large reversible capacity (935 mA h g^{-1} after 30 cycles), excellent cyclic performance, good rate capability	[184]
	A high capacity of 931 mA h g^{-1} was obtained at 4450 mA g^{-1}	[185]
	Reversible capacity after 100 cycles is 975 mA h g^{-1} with the irreversible capacity loss less than 3%	[186]
	>800 mA h g^{-1} reversibly at 200 mA g^{-1}, >550 mA h g^{-1} at 1000 mA g^{-1}	[53]

	941 mA h g^{-1} in the initial cycle at a current density of 200 mA g^{-1} and an excellent cyclic performance of 740 mA h g^{-1} after 60 cycles	[187]
	A capacity of 732 mA h g^{-1} can be obtained after 100 cycles at 150 mA g^{-1}	[188]
	An initial reversible lithium storage capacity of 722 mA h g^{-1} in LIBs and a specific capacitance of 478 F g^{-1} in 2 M KOH	[189]
	High reversible capacity of 1100 mA h g^{-1} in the first 10 cycles, over 1000 mA h g^{-1} after 130 cycles, with excellent cycle performance	[190]
	A first reversible capacity of 915 mA h g^{-1} at C/5, and 84% capacity retention after 30 cycles	[191]
G/Fe_2O_3	The first discharge and charge capacities are 1693 and 1227 mA h g^{-1} at 100 mA g^{-1} and retain a reversible capacity of 1027 mA h g^{-1} after 50 cycles	[192]
	The initial discharge capacity is 1338 mA h g^{-1} and 58% of the reversible capacity can be maintained over 100 cycles at 200 mA g^{-1}	[193]
	A high discharge capacity of 660 mA h g^{-1} during up to 100 cycles at the current density of 160 mA g^{-1} and capacities of 702, 512, 463 and 322 mA h g^{-1} at 400, 800, 1600 and 2400 mA g^{-1}, respectively	[194]
G/Mn_3O_4	A high specific capacity up to 900 mA h g^{-1}, good rate capability and cycling stability	[195]

G/MnO	A reversible capacity of 635 mA h g^{-1} at 0.2 C and the rate capacity retention 5 C/0.2 C>70%	[196]
G/Fe_3O_4	A large reversible specific capacity of 1048 mA h g^{-1}at the 90th cycle, enhanced cycling performances (about 650 mA h g^{-1} after 50 cycles) and high rate capabilities (350 mA h g^{-1} at 5 C)	[197]
	A specific capacity of 1280 mA h g^{-1} at 0.1 C cycling and 860 mA h g^{-1} at 4 C rate with exceptional stability	[198]
	A reversible capacity of 474 mA h g^{-1} at a current density of 1600 mA g^{-1}; a capacity of 637 mA h g^{-1} at 200 mA g^{-1} was retained after 60 cycles	[199]
	The capacity keeps at 796 mA h g^{-1} after 200 cycles without any fading, and the reversible capacity attains ~550 mA h g^{-1} and 97% of initial capacity is maintained after 300 cycles at 1 A g^{-1}	[200]
	A high reversible capacity is about two and a half times higher than that of graphite-based anodes at a 0.05 C rate, and an enhanced reversible capacity of about 200 mA h g^{-1} even at a high rate of 10 C (9260 mA g^{-1})	[201]
	The reversible capacity is 538.7 mA h g^{-1} after 50 cycles	[202]
	A specific discharge capacity of 952.0 mA h g^{-1} in the initial cycle and 842.7 mA h g^{-1} after 100 cycles	[203]
	A high reversible specific capacity approaching 1026 mA h g^{-1} after 30 cycles at 35 mA g^{-1} and 580 mA h g^{-1} after 100 cycles at 700 mA g^{-1} as well as improved cyclic stability and excellent rate capability	[204]

	A stable capacity of 650 mA h g^{-1} with no noticeable fading for 100 cycles	[205]
	A stable high specific reversible capacity of around 900 mA h g^{-1} which was nearly unvarying over 50 cycles	[206]
G/NiO	A capacity of 450 mA h g^{-1} after 100 cycles at 1 C (1 C=300 mA g^{-1}) and a discharge capacity of 185 mA h g^{-1} at 20 C	[207]
	A large initial charge capacity of 1056 mA h g^{-1} at 0.1 C and retained 1031 mA h g^{-1} after 40 cycles; the charge capacities of 872, 657, and 492 mA h g^{-1} were obtained at 718, 1436 and 3590 mA g^{-1}, respectively	[208]
G/TiO_2	87 mA h g^{-1} at a rate of 30 C (2 min of charging or discharging)	[209]
	Negligible fade after 700 cycles at 1 C rate with columbic efficiency reaching 100% over the entire cycling test except for the initial few cycles	[210]
	A reversible capacity of 161 mA h g^{-1} can be retained at 1 C after 120 charge–discharge cycles and delivered a capacity of 125 mA h g^{-1} and 107 mA h g^{-1} at 5 C and 20 C, respectively	[211]
	A reversible capacity of 90 mA h g^{-1} can be delivered at a current rate of 10 C with good cyclic retention up to 180 cycles	[212]
	A first discharge capacity of 269 mA h g^{-1} is achieved at 0.2 C and a capacity of 202 mA h g^{-1} in the charging process, the reversible capacities are retained at 162 and 123 mA h g^{-1} at 1 C and 10 C	[213]
	Specific capacity at the rate of 50 C is as high as 97 mA h g^{-1}	[214]

G/CuO	Reversible capacity of 600 mA h g^{-1} at 65 mA g^{-1} after100 discharge–charge cycles	[215]
	A reversible capacity of 583.5 mA h g^{-1} with 75.5% retention of the reversible capacity after 50 cycles	[216]
	The reversible capacity attains 640 mA h g^{-1} at 50 mA g^{-1} and the capacity retention is ca. 96%. At 1 A g^{-1}, the reversible capacity reaches 485 mA h g^{-1} and remains at 281 mA h g^{-1} after 500 cycles	[217]
G/Cu_2O	1100 mA h g^{-1} in the first cycle	[218]
G/CeO_2	A specific capacity of 605 mA h g^{-1} at the 100th cycle at 50 mA g^{-1} and the capacities of 414, 320, 222 and 146 mA h g^{-1} could be obtained at 100, 200, 400 and 800 mA g^{-1}, respectively	[219]
G/MoO_2	The initial discharge and charge capacities are 468.2 and 342.0 mA h g^{-1} and the capacity reaches 407.7 mA h g^{-1} after 70 cycles at 2000 mA g^{-1}	[220]
G/V_2O_5	An initial specific discharge capacity of 412 mA h g^{-1} at 50 mA g^{-1} and a capacity of 316 mA h g^{-1} at the current density of 1600 mA g^{-1}	[221]
G/SnO_2; G/NiO; G/MnO_2	Specific capacity of 625, 550, 225 mA h g^{-1} are obtained at 0.01, 0.02 and 0.08 A g^{-1} for SnO2–graphene; the capacity of the NiO–graphene composite is stable upon lithiation/delithiation over 100 cycles	[141]
G/TiO_2 at	The specific capacity was 175, 166, 150 and 130 mA h g^{-1} at a rate of C/3, 1 C, 3 C and 12 C, respectively	[214]

TiO_xN_y/TiN		
G/MnO_2	A reversible specific capacity of 495 mA h g^{-1} at 100 mA g^{-1} after 40 cycles and reached a capacity of 208 mA h g^{-1} at1600 mA g^{-1}	[194]
	A discharge capacity of 1105 mA h g^{-1} was observed on the second cycle, remaining 948 mA h g^{-1} after 15 cycles; a reversible capacity of 930, 836, and 698 mA h g^{-1} at 100, 200, and 400 mA g^{-1}, respectively	[206]
G/$Li_4Ti_5O_{12}$	Specific capacities were 164 mA h g^{-1} at 0.2 C and 137 mA h g^{-1} at 8 C	[191]
	A specific capacity of 122 mA h g^{-1} even at a very high charge/discharge rate of 30 C	[213]
G/$LiFePO_4$	A discharge capacity of 160.3 mA h g^{-1} at 0.1 C and 81.5 mA h g^{-1} at 10 C	[222]
G/$Li_3V_2(PO_4)_3$	The specific capacities are 118 mA h g^{-1} and 109 mA h g^{-1} at 5 C and 20 C discharge rates, and 82 mA h g^{-1} at a higher current rate of 50 C, reaching 64% of the initial charge capacity at 0.1 C	[208]

G: Graphene; MO: MOs; NPs: NPs.

The Li-storage mechanism of MOs is based on the lithium conversion reaction or lithium ion intercalation reaction. Therefore, the cycling performance of MOs can be improved by restraining its volume change and enhancing the electrical conductivity in the electrochemical process. Due to its intrinsically excellent electrical conductivity and mechanical flexibility, rGO is considered for anchoring MO NPs on its carbon network to improve the cyclability of the composites. For example, Kim *et al.* decorated echinoid-like SnO_2 NPs uniformly on rGO sheets through electrostatic attraction between the carbon networks and NPs by controlling the surface charge[52]. The resultant SnO_2/rGO composites have a reversible capacity of 634 mAh g^{-1} with a coulombic efficiency of 98% after 50 cycles, which is much higher than that of commercial SnO_2. In order to achieve high-performance LIBs, a chemical in-situ deposition strategy used to directly synthesize NP/rGO composites as the anode material for LIBs was reported by Wu *et al.* [184]. The Co_3O_4 NPs with particle size 10−30 nm are homogeneously distributed on rGO sheets, which separate the individual rGO layers by increasing the interlayer distance. The first discharge and charge capacities of Co_3O_4/rGO composite electrodes has been detected at 1097 and ~753 mAh g^{-1}, which are lower than that of both Co_3O_4 (1105 mAh g^{-1} and 817 mAh g^{-1}) and graphene (2179 and 955 mAh g^{-1}). However, the reversible capacity of the composite electrodes is 900 mAh g^{-1} after 20 cycles, which is much higher than that of Co_3O_4 (650 mAh g^{-1}) and graphene (245 mAh g^{-1}). For the fabrication of high-performance LIBs, Co_3O_4/rGO has been recognized as a potential candidate due

to its great electrical conductivity and mechanical stability caused by interlayer separation of rGO sheets in the composite structure[186].

Moreover, electrical conductivity of rGO is essential for improving the capacity of the electrode materials, especially those high rate anode materials such as $Li_4Ti_5O_{12}$ [223], TiO_2 [209], as well as cathode materials such as $LiFePO_4$ [224]. GO sheets are usually used as an additive by spray-drying and thermal annealing to enhance the electrical conductivity of nano-structured $LiFePO_4$/rGO composites. The resultant composites can deliver a higher specific capacity of 148 mAh g^{-1} at the rate of 0.1C and 70 mAh g^{-1} at 60C while the pure $LiFePO_4$ electrode has a lower capacity of 113 mAh g^{-1} at 0.1C[224]. In addition, the capacity of the composites is maintained at about 70% of the initial capacity after 1000 cycles.

The in-situ reduction process was also reported to produce a Co_3O_4/rGO hybrid material, rGO sheets uniformly covered by Co_3O_4 particles with the size at 5 nm [53]. Its unique nanostructure leads to superior electrochemical performance in lithium ion capacity as high as 800 mAh g^{-1} at a current rate of 200 mA g^{-1} and over 550 mA h g^{-1} at a high current rate of 1000 mA g^{-1}.

In summary, electrochemical performance of MO/rGO composites as the electrodes in LIBs is beneficial due to the elastic, flexible framework of 3D rGO-based structures. The cycling performance of MOs is also improved by binding small-sized particles with rGO, which significantly inhibits the volume change and shortens the transport

distance of lithium ions and electrons. Table 2-4 lists the advantages and disadvantages of rGO and MO as well as MO/rGO for LIBs [142].

Table 2-4 The pros and cons of rGO, MOs, and MO/rGO composites for LIBs [142].

Advantage of rGO	Disadvantage of rGO	Advantage of MO	Disadvantage of MO	Advantage of MO/rGO composites
Superior electrical conductivity	Serious agglomeration	Very large capacity/capacitance	Poor electrical conductivity	Synergistic effects
Abundant surface functional groups	Re-stacking	High packing density	Large volume change	Suppressing the volume change of MO
Thermal and Chemical stability	Large Irreversible capacity	High energy Density	Severe aggregation/agglomeration	Suppressing agglomeration of MO and re-stacking of graphene
Large surface area	Low initial coulombic efficiency	Rich resources	Large irreversible capacity	Uniform dispersion of MO
High surface-to-volume ratio	Fast capacity fading		Low initial coulombic efficiency	Highly conducting and flexible network
Ultrathin thickness	No clear lithium storage mechanism		Poor rate capability	High capacity/capacitance, good rate capability
Structural flexibility	No obvious voltage plateau		Poor cycling stability	Improved cycling stability
Broad electrochemical window	Large voltage hysteresis			Improved energy/power densities

MO: Metal oxides.

2.8 Summary

This literature review provides an overview of the properties, synthesis and functionalization of GO and rGO. GO and rGO is shown to be a unique two-dimensional structure with attached oxygen functional groups which can be removed to improve the properties in electrical conductivity, electrochemical performance, chemical activity and wettability. The review on these properties enables us to further understand the structural changes between GO and rGO sheets. In addition, the description on the synthesis methods is useful in understanding the formation and removal process of functional groups on the GO plane. Furthermore, the recent progress in the functionalization of rGO sheets to fabricate MO NP/rGO composites for energy storage applications is also reviewed. The advantages of chemical oxidation, thermal reduction and MO NPs functionalization of GO have been presented. However, there is a large distance to go before the fabrication of rGO sheets can meet the requirements of industrial applications. Therefore, this study will focus on the synthesis of functionalized rGO sheets and its application.

Chapter 3 Methodology

3.1 Introduction

The experimental details and characterization techniques used for the synthesis and analysis of rGO are described in this chapter. The synthesis methods for GO dispersion, single-layer GO sheets and GO paper are discussed, respectively. The process of thermal annealing and oxygen annealing to produce TrGO and OrGO are presented as are the fabrication details of TrGO and OrGO based LIBs. In order to analyze the properties of rGO, the characterization methods such as AFM, contact angle, Photoluminescence (PL), FTIR, Hall measurements, HRTEM, Raman spectroscopy, SEM, TEM, UV-Vis, X-ray Photoelectron Spectroscopy (XPS), XRD and Electrochemical measurements, along with their background knowledge and associated specimen preparations are all included.

3.2 Preparation of GO dispersion

3.2.1 Pretreatment of graphite powder

In order to oxidize the raw materials completely, the pretreatment step was performed according to the method published by Kaner *et.al* [88]. $K_2S_2O_8$ (10 g) and P_2O_5 (10 g) were added to a hot concentrated H_2SO_4 (90 ℃, 50 ml) solution. The mixture was then allowed to cool to 80 ℃ followed by adding graphite powder (325 mesh, 12 g) to the solution and stirring at 80 ℃ for 4.5 hours to dissolve all the components. Subsequently, the mixture was diluted into DI water (2L). The next day the mixture was filtered through a cellulose ester membrane filter and washed using DI water to

remove all traces of acid. The resultant solid was dried overnight under ambient conditions.

3.2.2 Modified Hummer's Method for oxidation of graphite

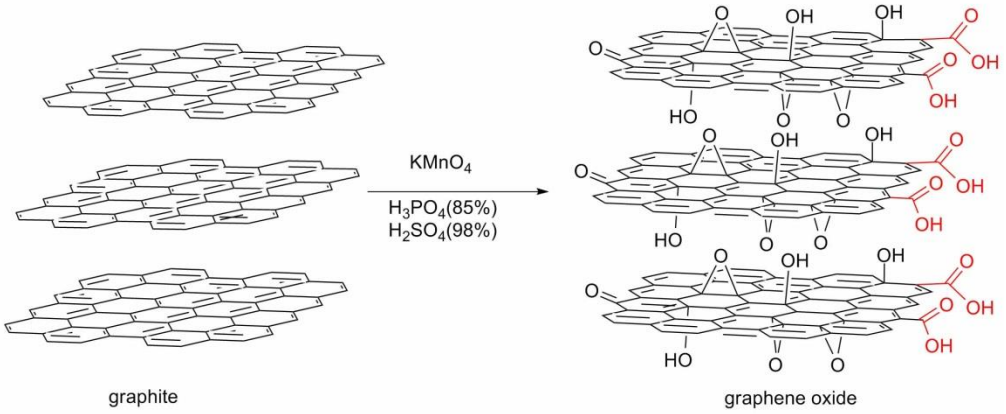

Figure 3.1 Schematic diagram to produce GO sheets by Hummer's Method [225]

The modified Hummer's method was used to synthesize graphite oxide from pretreated graphite powder. As illustrated in Figure 3.1, H_2SO_4 (23 ml) was poured into a 250 ml round bottom flask and then chilled to 0 ℃ in an ice bath. Afterwards, the pretreated graphite powder (1.0 g) and $NaNO_3$ (0.5 g) were added sequentially to the flask followed by mixing $KMnO_4$ (5.0 g) in droplets to keep the temperature below 10 ℃. After stirring at 35 ℃ for 2 hours, DI water (46 ml) was cautiously added to the mixture in small portions to keep the temperature below 50 ℃. Another 140 ml of DI water and 10 ml of 30% H_2O_2 were added to the flask to end the oxidation process after 2 hours stirring. The mixture was settled for at least 24 hours to obtain a clear supernatant. The deposited solid mixtures were collected and repeatedly purified with 500 ml of 10% HCl solution and 500 ml of DI water to remove the acid. The resulting solid was dried at room temperature in a vacuum chamber.

3.2.3 Formation of GO dispersion

GO dispersion (2 mg ml^{-1}) was prepared by dissolving air-dried GO sheets in DI water using an ultrasonic bath cleaner (output power 20 W) for 1 hour, followed by centrifugation (10000 rpm, 10 min) to remove impurities precipitated on the centrifuge tube wall. In order to exfoliate GO sheets completely in the dispersion, a probe ultrasonicator (output power 100 W) was immersed in the resultant transparent light-yellow dispersion for 30 minutes. The resultant dispersion was then left aside for at least one week to obtain a final GO dispersion with a concentration of 2 mg ml^{-1}.

3.3 Preparation of free-standing GO paper

3.3.1 Filtration of GO dispersion

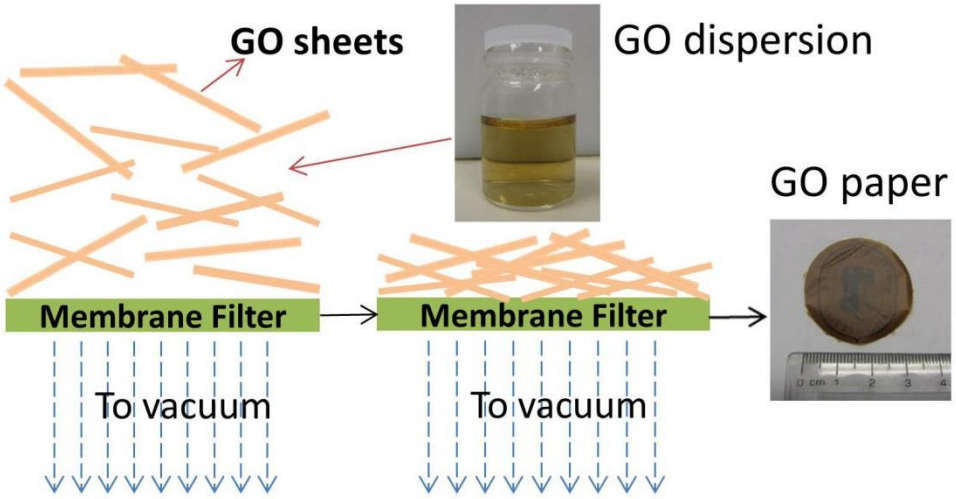

Figure 3.2 Schematic diagram for the fabrication of GO paper by vacuum filtration of GO dispersion through a membrane filter.

Paper-like GO bulk material was prepared simply by a vacuum filtration process. GO dispersion (150 ml) was added to a Buchner funnel which was connected to a vacuum source and then filtered through a membrane filter. During the vacuum filtration, GO

sheets were laid down on the membrane filter plane while the liquid was passing through the pores under a directional flow caused by vacuum suction. GO sheets were interlocked/tiled on top of each other in a nearly parallel manner, as shown in Figure 3.2.

3.3.2 Types of membrane filter

According to the introduction in section 1.5.3, membrane filters are essential to the fabrication of OrGO (Al_2O_3/rGO) paper. In order to confirm the source of Al_2O_3 nanoparticles is the Anodisc membrane filter, two types of membrane filter were used in the preparation of GO paper by vacuum filtration:

i. Mixed cellulose ester membranes (SEM image, Figure 3.3)

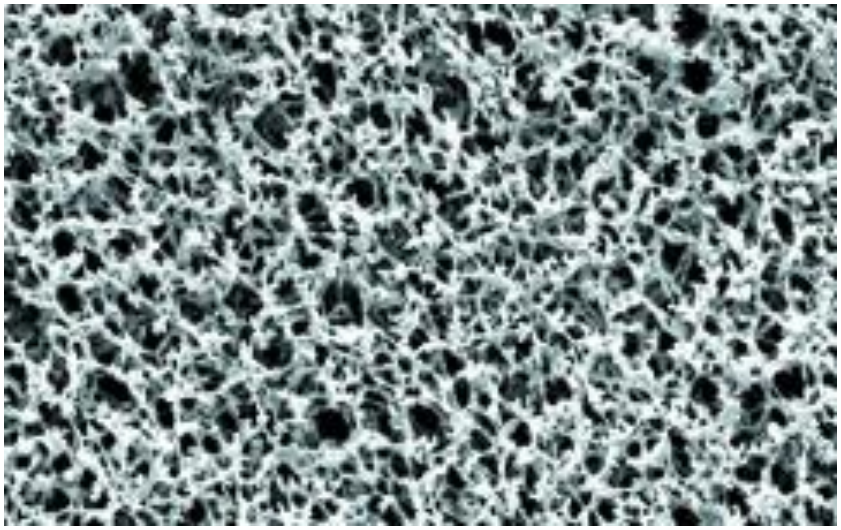

Figure 3.3 SEM image of mixed cellulose ester membrane filters. The pore size is 0.2 μm[226].

ii. Anodisc aluminum oxide membranes (SEM image, Figure 3.4)

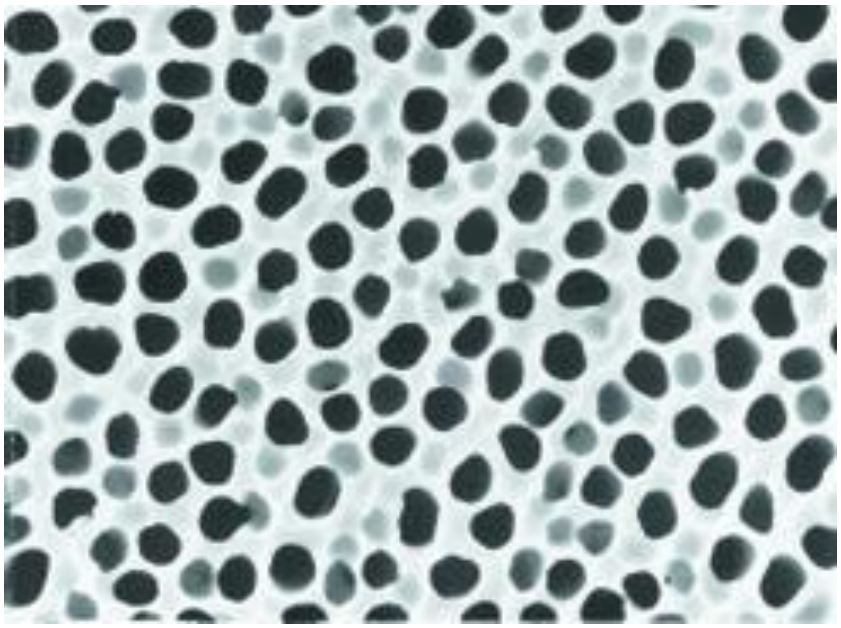

Figure 3.4 SEM image of Anodisc aluminum oxide membrane. The pore size is 0.02 μm[227].

Table 3-1shows the specifications of these two membrane filters.

Table 3-1 Specifications of membrane filters.

Membrane type	**Material**	**Pore size (μm)**	**Diameter (mm)**	**Rectangular**	**Brand name**
Cellulose based	Mixed Cellulose Ester	0.2	47	300×600 mm	
Anopore	Aluminum Oxide	0.02	47	300×600 mm	Anodisc

3.3.3 GO paper peeling off from the membrane filter

3.3.3.1 Mixed cellulose ester membranes

After air-drying overnight at room temperature, GO paper deposited onto mixed cellulose ester membrane was peeled off by immersing the mixture in acetone baths to dissolve the cellulose ester membrane and transferring to DI water baths to wash peeled GO paper, leaving the transparent GO paper floating on DI water. The resultant

GO paper was then transferred onto substrates for air-drying at room temperature to obtain GO film.

3.3.3.2 Aluminum oxide membranes

Unlike the process using mixed cellulose ester membranes, GO paper fabricated by filtering GO dispersion through the aluminum oxide membrane can be peeled off actively during air-drying at room temperature to form transparent free-standing GO paper without using any solvent.

3.3.4 Samples preparation for characterizations

Free-standing GO paper can be directly characterized by measurements such as FTIR, Raman spectroscopy, XPS, and Electrochemical testing. For the characterizations including contact angle, PL, Hall measurements, UV-Vis and XRD, GO paper should be stuck on pretreated quartz plates (pretreatment step described in 3.4.3).

3.4 Preparation of single-layer GO sheets on the substrates

3.4.1 Preparation of diluted GO dispersion

Initially the as-formed GO dispersion prepared in 3.2.3 was diluted in DI water to a concentration of 10 ppm. Afterwards, the probe ultrasonicator was used for further separation of GO sheets, followed by ultrasonication using an ultrasonic bath cleaner for 3 hours. Finally, high speed centrifugation (15,000 rpm, 10 minutes per cycle) was performed for exfoliation of GO sheets and deposition of multi-layer GO.

3.4.2 Fabrication of Al_2O_3/GO monolayer structure

In order to characterize the properties of OrGO, individual piece of Al_2O_3/GO sheet containing a monolayer GO structure was fabricated using the same vacuum filtration system described in section 3.3.1. Before the filtration system was connected to the vacuum pump, the substrate (1×1 cm for cuttable materials) was placed onto a membrane filter, placed in the bottom of a Buchner funnel, and immersed in the diluted GO dispersion (10 ml) added to the funnel for several minutes. Afterwards, a few of the monolayer GO sheets were deposited onto the substrates during vacuum filtration process (Figure 3.5). The deposited GO sheets can be considered as individual sheets of GO paper for characterization.

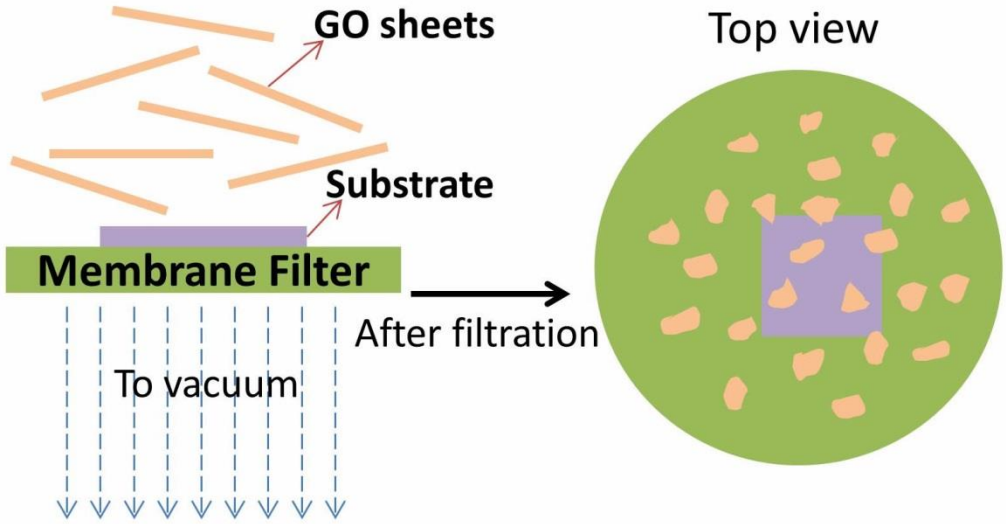

Figure 3.5 The schematic diagram of monolayer of GO sheets deposited on the substrate via a filtration process. The substrate (1×1 cm for cuttable materials) was placed onto a membrane filter and immersed in the diluted GO dispersion (10 ml) added to the funnel for several minutes.

3.4.3 Substrates

The substrates selection was carried out according to the requirements of the characterizations. The substrates used for the deposition process are given below:

i. Holey carbon TEM grids (300 mesh, TEM image Figure 3.6)

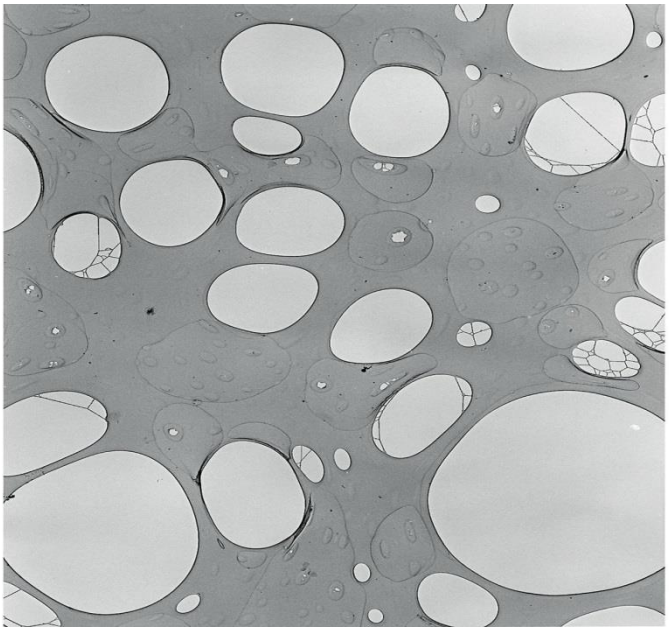

Figure 3.6 TEM image of holey carbon films[228]. The diameter of the holes is around 5 μm in average.

ii. SiO_2 layer (300 nm) coated silicon wafers (optical image, Figure 3.7)

Figure 3.7 Optical image of SiO_2/Si wafer[229]

The SiO_2/Si wafers were cleaned with a piranha solution, a mixture of H_2SO_4 and H_2O_2 used to remove organic residues on the substrates (H_2SO_4: 30 wt. % H_2O_2 = 3:1, v/v). The holey carbon TEM grids were used for the testing of TEM and HRTEM. The SiO_2/Si wafers were used for the characterizations of AFM and SEM.

3.5 Fabrication of TrGO by thermal annealing

Thermal annealing is a conventional method for the reduction of GO to enhance its electrical conductivity. This annealing was carried out in a single zone horizontal tube furnace using a mechanical vacuum pump and a two-channel gas flow system. GO paper or GO sheets deposited on the substrates were placed in an alumina sample holder and loaded in the middle of the furnace. Once the tube had been sealed with stainless steel flanges, a vacuum pump was used to keep the annealing chamber under

vacuum conditions at 15 torr. In order to protect the sample against the air and impurities, Argon gas was utilized as a carrier gas to remove chemical waste out of the chamber during the annealing process. Before thermal annealing was initiated, the GO sample was dried overnight at room temperature under Argon gas flow. The furnace was then heated to 400 ^{o}C with a ramping rate of 2 ^{o}C /min for thermal reduction. When the furnace reached the desired temperature, annealing was performed for 30 min before cooling down to room temperature at the rate of 20 ^{o}C /min. The annealed samples were taken out when the temperature of the tube was below 50 ^{o}C, which avoided any sample damage when exposing to the air at high temperature. The thermal annealing conditions for GO sample reduction are shown in Table 3-2.

Table 3-2: The thermal annealing conditions for GO paper reduction.

Process parameter	**Process condition**
Dwelling temperature (^{o}C)	400
Ramp rate (^{o}C/min)	2
Duration (min)	30
Ending temperature (^{o}C)	Below 50
Pressure (Torr)	15
Size of sample (cm×cm)	1×1
Ar flow rate (sccm)	95

3.6 Fabrication of OrGO by oxygen annealing

Oxygen annealing was carried out in the same tube furnace as thermal annealing, as shown in Figure 3.8. GO samples were placed in an alumina sample holder and loaded in the middle of the furnace, which was sealed with stainless steel flanges. A vacuum pump was used to keep the annealing chamber under vacuum conditions at 15 torr. In order to dry and clean the surface of samples, Argon was utilized as a carrier gas

before the annealing process. Before operation of the heat treatment, the GO sample was dried at room temperature under Argon gas flow overnight. The furnace was then heated to 400 ^{o}C with a ramping rate of 2 ^{o}C /min. When the furnace reached the desired temperature, oxygen gas was introduced into the chamber at a flow rate of 10 sccm to synthesize Al_2O_3 NPs on the rGO plane. After 30 min heat treatment, the cooling rate was 20 ^{o}C /min. GO samples for oxygen annealing included GO paper and single-layer GO sheets deposited onto the substrates. The operating conditions were described in section 3.5.

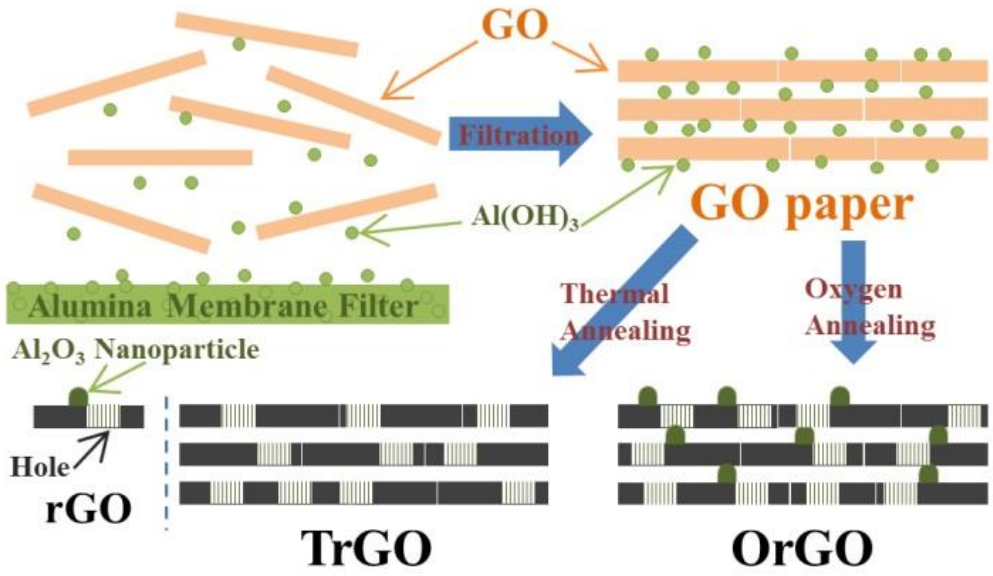

Figure 3.8 The schematic diagram of the fabrication process of TrGO and OrGO papers and individual layer.

3.7 Characterization methods

3.7.1 Atomic Force Microscopy

AFM was used to quantitatively characterize the morphology and roughness of single- or few-layer GO surfaces. Figure 3.9 shows the basic principles of AFM [95]. The tip

is precisely situated on a flexible silicone cantilever which is mounted to a piezoelectric driver for scanning. When the voltage is applied, the tip is brought to a chosen point over the sample surface where the force can repel or attract atoms from the tip leading to a deflection of the cantilever. The degree of cantilever deflection, which is caused by the surface topography, is usually measured using a laser light from a solid state diode reflected from the surface of the cantilever into a position sensitive detector (PSD). In this way, it is possible to map out the roughness of the material surface point by point without any direct contact. AFM promises scanning in the x/y or x/y/z directions to reconstruct the surface image from different viewpoints. Moreover, there is no extra surface treatment, such as metal or carbon coating, required for AFM measurement[230].

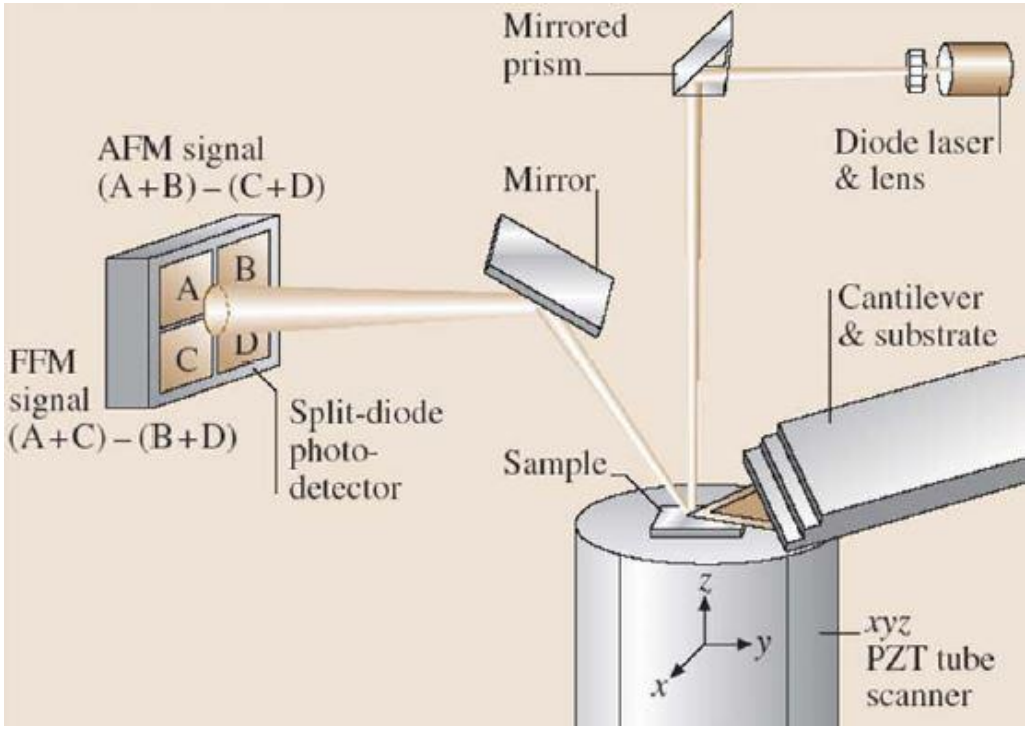

Figure 3.9 The basic principles of atomic force microscopy (AFM) [95]

The surface morphology of GO was characterized using an AFM (Veeco CPII-Research Scanning Probe Microscope) in contact mode at a 512 x 512 scanning resolution. Scan areas ranged from 600 nm x 600 nm to 10 μm x 10 μm. In the contact mode, the tip makes a soft physical contact with the sample surface and scans at a constant small height above the surface where the overall force is repulsive. The force between the tip and the GO sheets is fixed during scanning by maintaining a constant deflection.

3.7.2 Scanning Electron Microscopy

SEM is a microscope that uses electrons instead of light to form an image. In comparison to traditional microscopes, SEM has many advantages such as large depth of field, higher resolution and more control in the degree of magnification[231], which allows it to be used in fracture characterization, microstructure studies, thin film evaluation, surface contamination examination and failure analysis of materials. Generally, a high-energy electron beam is produced from the electron gun in an evacuated column above the sample surface. When the electron beam focuses onto the target surface, the low-angle backscattered electrons interact with the surface atoms and generate a variety of electronic signals. Figure 3.10 shows a schematic diagram of SEM. The types of signals generated secondary electrons (SE), back-scattered electrons (BSE), characteristic X-rays, light cathodoluminescence (CL), specimen current and transmitted electrons as are shown in Figure 3.10[100].

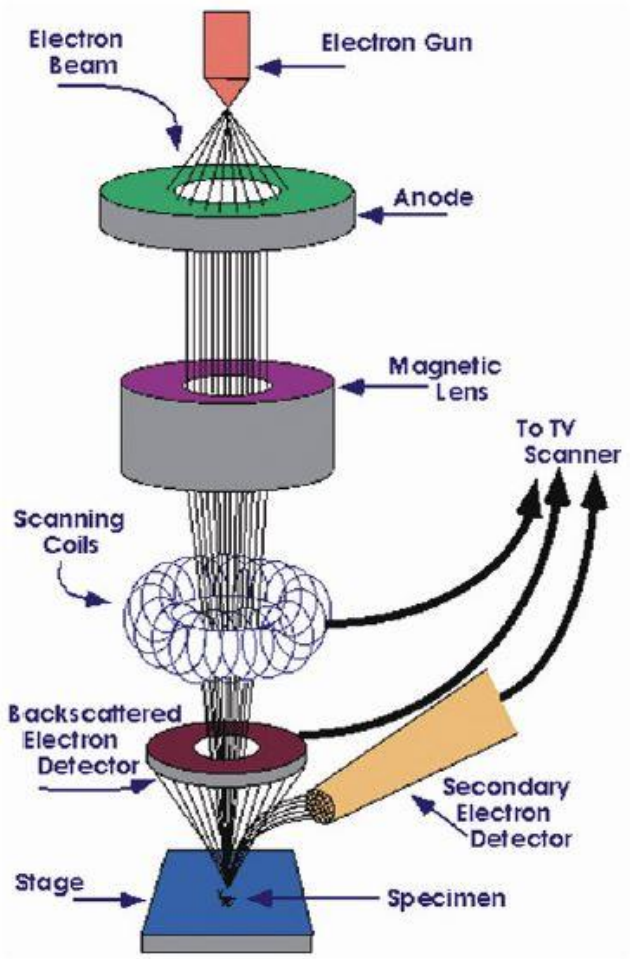

Figure 3.10 Schematic diagram of SEM[100].

For conventional imaging in the SEM, the specimens' surface must be electrically conductive. However, environmental SEM (ESEM) can be used to image uncoated nonconducting specimens by placing the sample in a high-pressure chamber where the working distance between the electron gun and the specimens is short[232].

The SEM samples were fabricated by attaching GO samples to an aluminum stub using a sticky carbon tab. In this study, a secondary electron detector was used. The prepared samples were placed in the vacuum chamber of the microscope. The SEM was

operated with a working energy of 7 k eV, a beam size at a value of 3 and a working distance of 10 mm. Images at a variety of magnifications were collected.

3.7.3 Transmission electron microscopy

TEM is a microscopy technique utilizing a beam of electrons transmitted through an ultra-thin specimen where the electrons are converted to light and form an image. The image is magnified and focused onto an imaging device, such as a fluorescent screen, on a layer of photographic film, or to be detected by a sensor such as a charge-coupled device (CCD) camera.

In this study, two types of TEM were used to characterize GO samples. A lower magnification inspection on GO samples was carried out by a JEOL FX II microscope while an advanced JEOL 2100F model was used to obtain higher resolution TEM (HRTEM) images by the addition of a field emission gun (FEG). This equipment can provide a high brightness and high stability electron source.

The basic components of TEM equipment are illustrated in Figure 3.11[233]. TEM images are produced by inserting photographic film into the back focal plane of the objective lens, which allows selected electrons to diffract in a specific direction. During transmission, the speed of electrons directly correlates to electron wavelength: the faster electrons move, the shorter wavelength and the greater the quality and detail of the image. Bright areas of the image represent places where more electrons have passed through the specimen while dark areas represent the dense areas of the object. In addition, NPs structure can be investigated by HRTEM at an atomic scale[234].

Because of its high resolution, it is a valuable tool for the study of the positions of atoms in TEM images due to differences in the phase of electron waves scattered by a thin sample. The GO samples were prepared according to 3.4.2 and then placed onto a sample holder and inserted into a vacuum chamber in the TEM system. The samples were inspected at various magnifications.

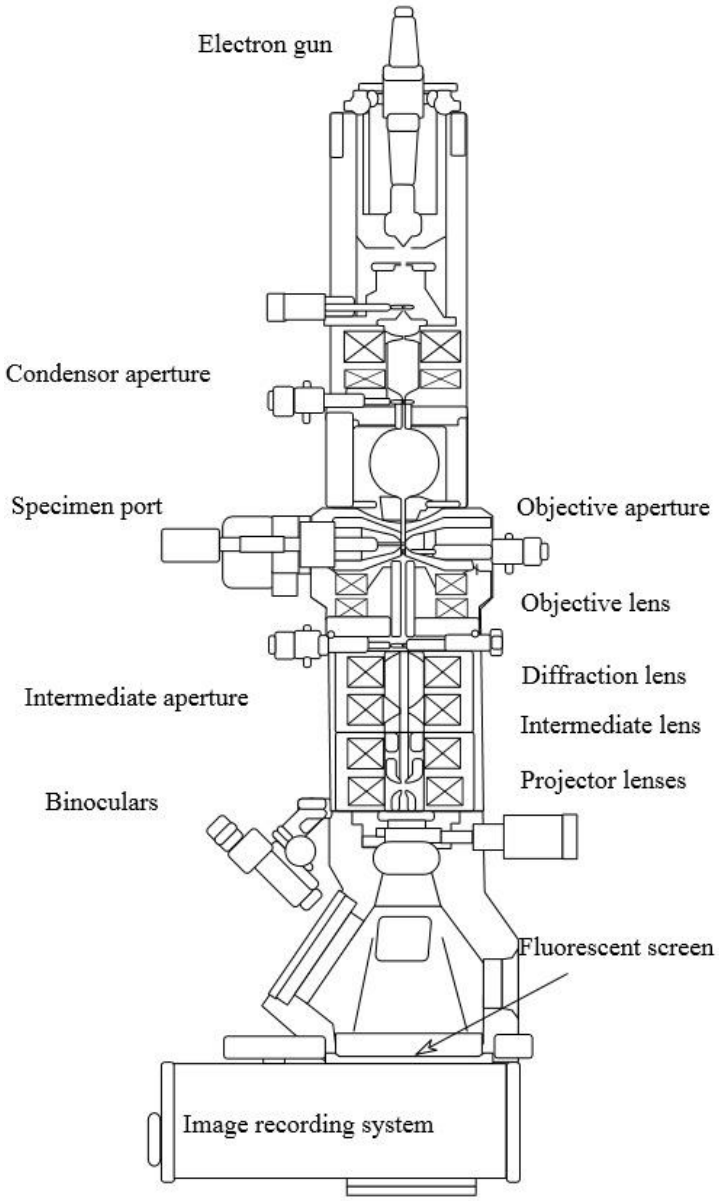

Figure 3.11 The schematic diagram of TEM[233]

3.7.4 Raman spectroscopy

Raman spectroscopy is used to investigate the elementary excitation in GO samples. In this technique, a monochromatic laser is shone onto the sample surface as shown in Figure 3.12[97]. The monochromatic laser with frequency v_0 excites the molecules within the specimen from the ground state to a virtual energy state. When the excited molecules reverts back, they emit light and return to a different rotational or vibrational state. The change in energy between the original state and resulting state leads to three different frequencies when:

1. A molecule is excited by absorbing a photon with frequency v_0 and then returned back to the same basic vibrational state. This elastic scattering of the photon is called Rayleigh scattering.
2. If the vibrational energy of the molecule is increased after absorbing a photon with frequency v_0, the energy of the scattered photons is decreased as part of the photon's energy is transferred to the Raman-active mode with a down-shifted frequency (longer wavelength). This inelastic scattering is called Stokes scattering.
3. If the vibrational energy of the molecule is decreased after absorbing a photon with frequency v_0, the energy of the scattered photons is increased as excessive energy of the excited Raman-active mode is released with an up-shifted frequency (shorter wavelength). This inelastic scattering is called anti-Stokes

scattering. This only happens when the molecule is an excited vibrational state before absorbing a photon.

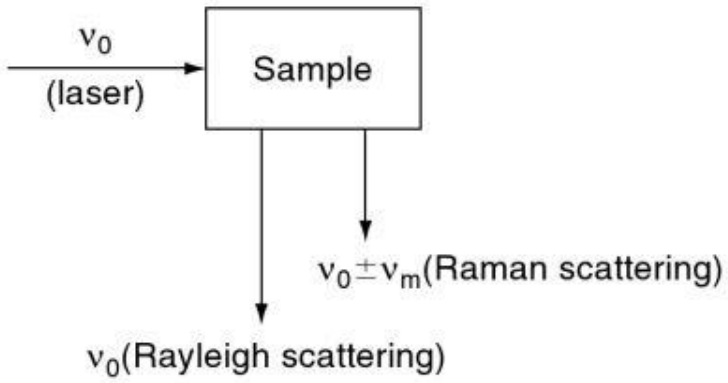

Figure 3.12 Mechanism of Raman scattering[97].

3.7.5 X-Ray Photoelectron Spectroscopy

XPS is a widely used spectroscopic technique for surface elemental composition analysis, empirical formulas, chemical states and the electronic state of the elements which exist within a material[99, 235]. The specimens are illuminated with a monochromatic X-ray source, resulting in the emission of core shell photoelectrons. The electrons can be removed from their orbits at characteristic binding energy values which is unique to the element and particular atomic orbits. As a result, a plot of the number of electrons detected versus the binding energy of the electrons detected is used to identify the elements present and their quality. The characteristic XPS peaks, corresponding to the electron configuration of the electrons within the atoms, e.g., 1s, 2s, 2p, 3s, etc., is used to directly identify the amount of element within the area irradiated. The XPS must be performed under Ultra-High Vacuum (UHV) conditions [236-238]. Figure 3.13 shows the schematic diagram of XPS systems[100].

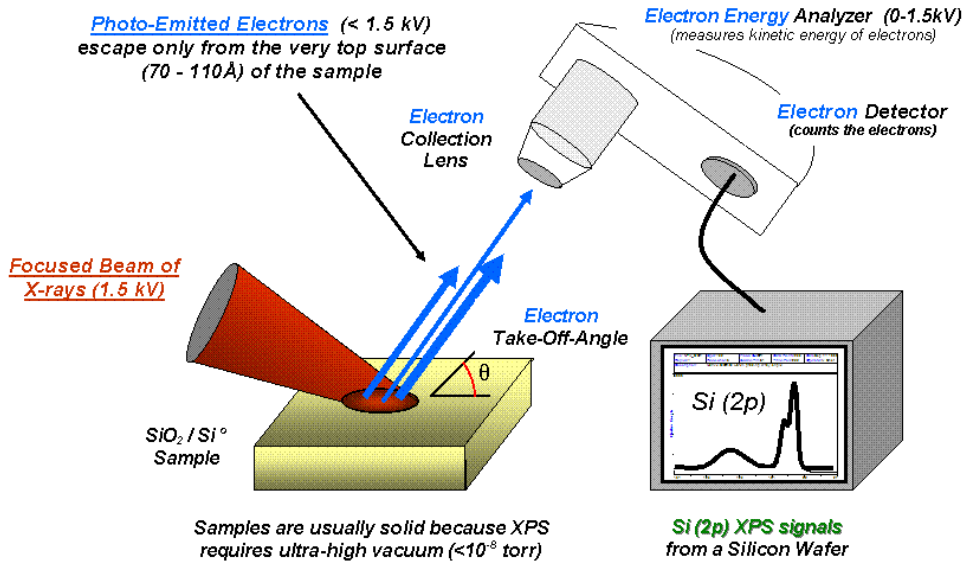

Figure 3.13 The schematic diagram of a monochromatic XPS system[100].

In this study, XPS measurements were performed with a VG Scientific ESCALab Mark II X-ray photoelectron spectrometer using a monochromatic Al Kα x-ray source (hν = 1486.6 eV). Survey spectra were collected covering the full binding energy range 0-1200 eV using a step size of 1 eV and pass energy of 50 eV, whereas the high resolution spectra of C1s, Al 2p and Al KLL were collected using a step size of 0.2 eV and pass energies of 20 eV. To compensate for surface charging, all binding energies were corrected with reference to the C1s peak at 284.5 eV. Peak fitting and deconvolution of the high resolution spectra were achieved using CasaXPS software and were fitted according to mixed Gaussian–Lorentzian components and a non-linear Shirley background.

3.7.6 Fourier transform infrared spectroscopy

FTIR is a technique used to detect the vibration characteristics of chemical functional groups in the materials by obtaining an infrared spectrum of absorption, emission, photoconductivity or Raman scattering of samples. An FTIR spectrometer simultaneously collects spectral data in a wide spectral range which can be categorized as far infrared (4 ~ 400 cm^{-1}), mid infrared (400 ~ 4,000 cm^{-1}) and near infrared (4,000 ~ 14,000 cm^{-1}). When an infrared light interacts with the sample, chemical bonds will stretch, contract and bend. As a result, a molecular fingerprint of the sample can be produced as the chemical functional group tends to absorb infrared radiation in a specific wavenumber range regardless of the structure of the rest of the molecule, which makes infrared spectroscopy useful for several types of analysis.

FTIR spectrometry was developed in order to overcome the limitations encountered with early-stage IR instruments, which use a prism or a grating monochromator and which results in a slow scanning process. FTIR spectrometer employs a very simple optical device called an interferometer to collect an interferogram of a sample signal, which has all of the infrared frequencies “encoded” into it. In order to make an identification, the measured interferogram signal should be interpreted by decoding the individual frequencies. This can be accomplished via a well-known mathematical technique called Fourier transformation[239]. Figure 3.14 shows the principle of FTIR[240].

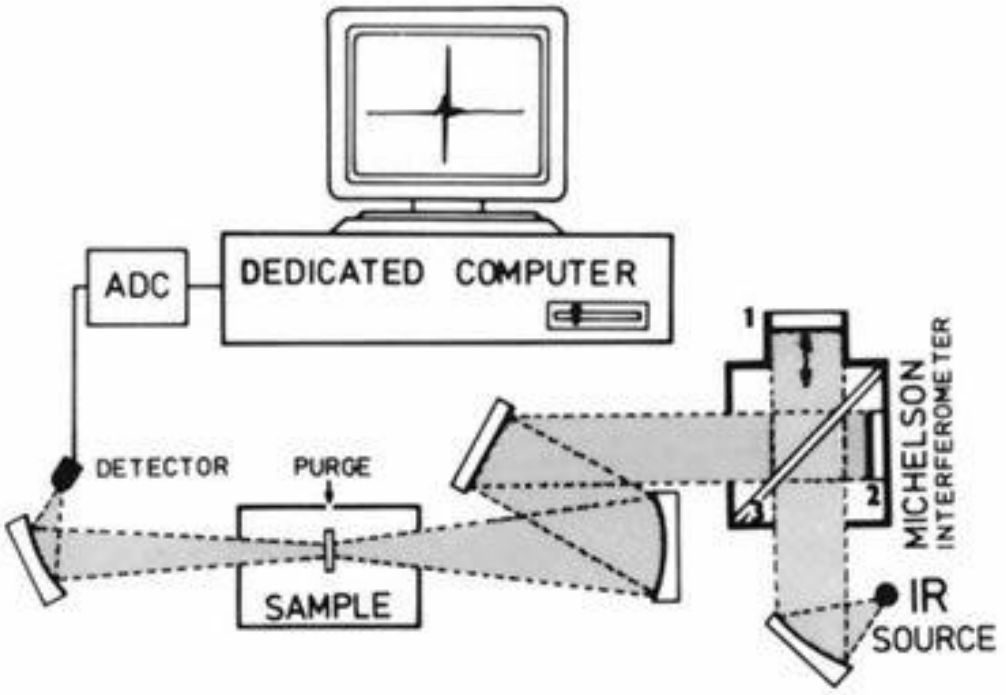

Figure 3.14 Schematic diagram of FTIR[240]

In this study, FTIR spectra of GO samples were measured with a Perkin-Elmer Spectrum One spectrometer. The scanning wavelength ranged from 540cm^{-1} to 4000cm^{-1} using a single reflection horizontal attenuated total reflection accessory which enables samples to be examined directly in the solid or liquid state without further preparation[241].

3.7.7 Sheet resistivity measurement

Sheet resistance is a measure used to determine the resistance of thin films which are nominally uniform in thickness. A four-terminal sensing measurement (also known as a four-point probe measurement) is widely used to measure sheet resistance, which can avoid contact resistance, according to the Van der Pauw method. This method is only used when the conditions below are satisfied:

1. The sample must be flat with a uniform thickness
2. The sample must not have any isolated holes
3. The sample must be homogeneous and isotropic
4. All four contacts must be located at the corners of the sample
5. The area of any individual contact must be at least an order of magnitude smaller than that of the entire sample.

A schematic of a rectangular Van der Pauw configuration is shown in Figure 3.15[242, 243].

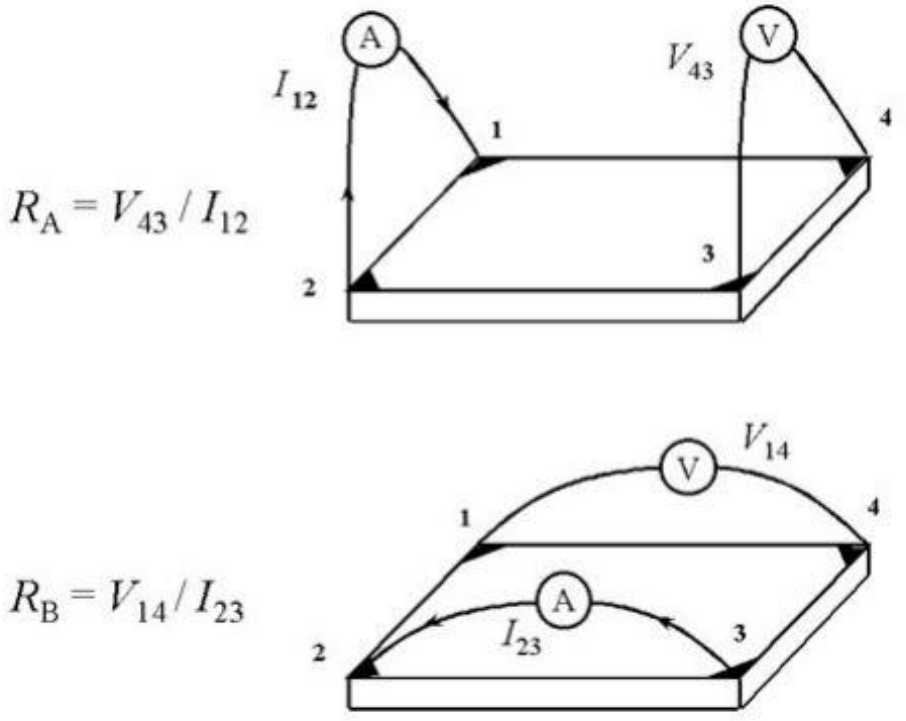

Figure 3.15 Rectangular Van der Pauw configuration[242, 243]

In order to obtain the two characteristic resistances, a direct current (I) is applied to contact corner 1 and 2 while the voltage (V_{43}) from contact corner 4 and 3 is measured.

Next, a current is applied to contact corner 2 and 3 while measuring the voltage (V_{14}) from contact corner 1 to 4. R_A and R_B are calculated by means of the following expressions (5) and (6):

$$R_A = \frac{V_{43}}{I_{12}} \tag{5}$$

$$R_B = \frac{V_{14}}{I_{23}} \tag{6}$$

R_A and R_B are related to the sheet resistance R_S through the Van der Pauw equation (7):

$$e^{-\pi\frac{R_A}{R_S}} + e^{-\pi\frac{R_B}{R_S}} = 1 \tag{7}$$

which can be solved numerically for R_S. The bulk electrical resistivity ρ can be calculated using (8):

$$\rho = R_S d \tag{8}$$

3.7.8 Contact angle measurement

This is the angle measured through a liquid at which the liquid/vapour interfaces with a solid surface. The contact angle is the result of the surface free energies between the liquid, solid and surrounding vapour. Most of the liquid wets the solid surface and shows a contact angle in a static system which can be represented by a small liquid droplet resting on a flat horizontal solid surface. The contact angles are measured by fitting a mathematical expression to the shape of the dropped liquid and then calculating the slope of the tangent to the drop at the liquid-solid-vapour interface line [244, 245].

The contact angle is commonly used in membrane material science to describe the relative hydrophobicity/hydrophilicity of a membrane surface.

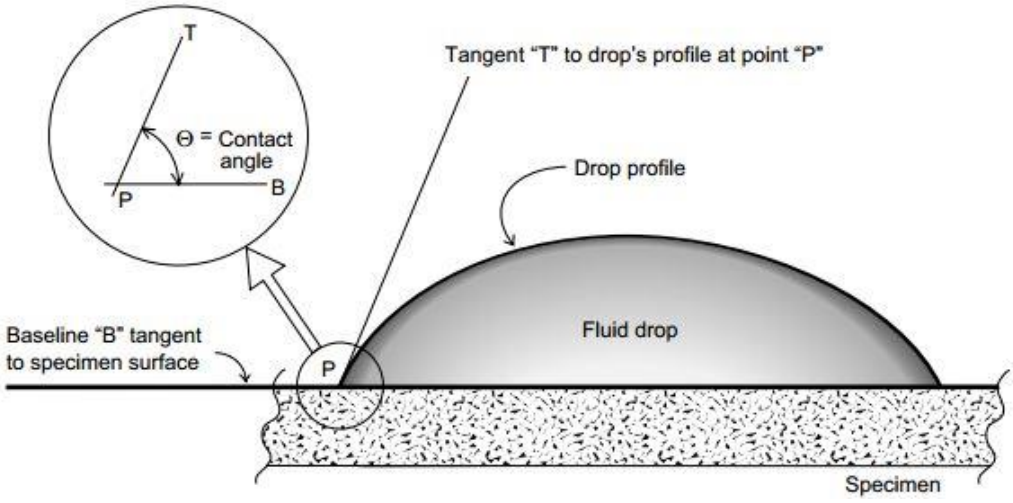

Figure 3.16 The schematic diagram of contact angle measurement[246].

The contact angle of GO was measured with a dynamic contact angle system, as shown in Figure 3.16[246]. This equipment can be used to measure the surface tension, adhesion characteristics, and surface energy as well. This equipment uses drop shape analysis to measure contact angles and thereby determine surface energy. The image of the drop shape was captured by an equipped camera. The shape and size of the droplets were analyzed using FTA 32V 2.0 software. The contact angle was measured 5 times for individual samples and then the average value was calculated. Wettability is divided into three classes: absolute wetting for $\theta = 0°$, partial wetting for $\theta < 90°$, and non-wetting for $\theta > 90°$ [247]. The water droplet was observed spontaneously spreading along the dry surface until an equilibrium angle was established.

3.7.9 Lithium-ion battery test cells assembly and performance evaluation

To evaluate the electrochemical performance of GO samples, split-able test cells (EQ-STC, MTI Corporation) were fabricated. The cells were assembled in an argon-filled dry box by pressing GO paper onto a stainless steel substrate as the working electrode without any binder or conductive additives. Celgard 2400 polypropylene membrane was used as a separator and lithium foil (Alfa Aesar) as the counter electrode. The electrolyte was a 1M lithium hexafluorophosphate ($LiPF_6$) solution in a mixture of ethylene carbonate, dimethyl carbonate and ethylene methyl carbonate (1:1:1 by weight).

3.7.10 Electrochemical measurement

In this study, cycle performance tests were used in a constant current / constant voltage (CC/CV) charging mode, which is an effective way to charge lithium batteries. When a LIB is nearly empty, the charging process is conducted under constant current. During the process, the charging current should be lower than the maximum charging current that the battery can accept. With constant charging, the voltage of the battery slowly rises until the battery voltage reaches the maximum charging voltage, at which point the charger, fixed at a "constant voltage" reduces the charging current until the battery is fully charged. In CC/CV mode, for each cycle, the test cells were charged with a constant current and then with constant voltage at 3.0V till the charge current declined to 10mA. After that, the batteries were discharged at 10 mV at a constant current. Cyclic voltammograms were characterized using an electrochemical cell with

a three-electrode configuration. Metallic lithium was used as a counter and reference electrodes. The experiment was carried out using a Maccor series 4300 Battery and Cell Test system.

3.7.11 Ultraviolet–visible spectroscopy

UV-Vis, an absorption or reflectance spectroscopy in the ultraviolet-visible spectral region, is used to analysize the quantity of different analytes, such as transition metal ions, highly conjugated organic compounds, and biological macromolecules. The analysis of the absorption and/or transmission uses light in the visible and adjacent (near-UV and near-infrared) ranges, the changes of the light intensity causing a variety of polarization of the reflected or transmitted beams. A typical UV-Vis spectroscopic analysis consists of measuring the wavelength dependence of the light transmitted through the sample Figure 3.17[248, 249]. When the light passes through or is reflected from the sample, the amount of light absorbed is the difference between the incident and the transmitted radiation.

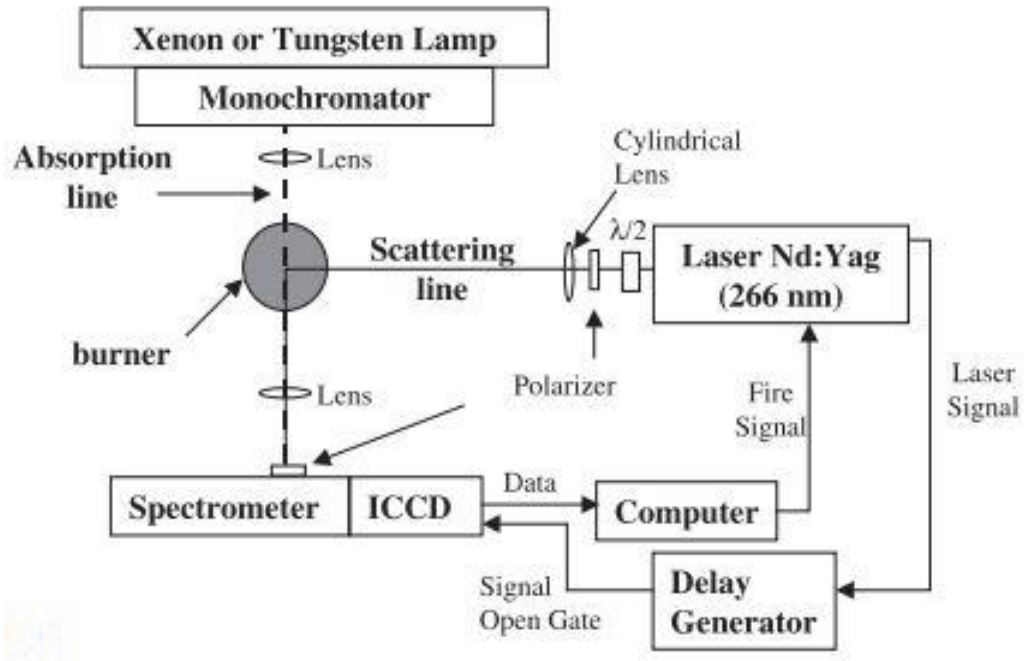

Figure 3.17 Schematic diagram of UV-Vis spectroscopy[248, 249].

A classical semiconductor exhibits minimal optical absorption or high absorption for photons when energies are smaller or greater than the bandgap. As a result, there is a sharp increase in absorption at energies close to the bandgap resulting in an absorption edge /reflection threshold in the UV-Vis absorbance spectrum.

For direct bandgap semiconductors (9):

$$\alpha(h\nu) \propto \frac{\sqrt{h\nu - E_g}}{h\nu} \tag{9}$$

where α is the absorption coefficient, $h\nu$ is the energy of incident photons and E_g is the electronic bandgap of the semiconductor. E_g is the intercept of the straight line obtained by plotting $(\alpha h\nu)^2$ vs. $h\nu$.

For indirect bandgap semiconductors (10):

$$\alpha(h\nu) \propto \frac{(h\nu - E_g)^2}{h\nu} \quad (10)$$

E_g is the intercept of the straight line obtained by plotting the square root of $(\alpha h\nu)^{1/2}$ vs. $h\nu$.

The optical transmittance and absorbance of GO sample were measured by a UV-Vis spectrometer (Biochrom Libra S22, Biochrom Ltd. Cambridge, England). This equipment incorporates on-board application software which enables the production of wavelength scans, substrate concentrations, and standard curves. The transmittance and absorbance scanning wavelength ranged from 200 nm to 900 nm. The results were directly transferred to Excel for calculating the band gap using the absorption coefficient from the transmittance data.

3.7.12 Photoluminescence spectroscopy

PL describes the phenomenon of light emission from materials after the absorption of photons (electromagnetic radiation). PL spectroscopy is a non-destructive analysis technique requiring minimal sample preparation. A typical PL system includes the two stages of photon absorption and re-radiation, as shown in Figure 3.18[250]. To carry out PL measurement, the excitation laser and photomultiplier tube are turned on followed by the installation of the sample onto a sample holder. The position of the excitation beam should be adjusted to guarantee the alignment of the sample, condenser and monochromator slit. The PL signal of the sample can be enhanced to increase the signal-to-noise ratio by increasing the size of the monochromator slit. In

this study, the Fluorescence Spectrophotometer (FL-2500, Luminescence (200 to 800 nm), Hitachi, Tokyo, Japan), was used to characterize the optical features of GO samples.

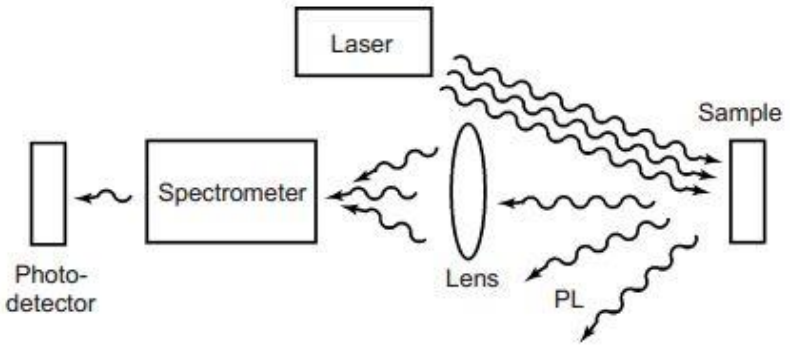

Figure 3.18 The schematic diagram of PL [250].

3.7.13 X-Ray Diffraction

XRD is a non-destructive method used for revealing information about the atomic and molecular structure of a crystal. In this method, crystalline atoms cause a beam of X-rays to diffract in many specific directions which can produce a three-dimensional picture of the density of electrons within the crystal. From this map of electron density, the physical properties, chemical composition and crystal structure of materials can be determined[251, 252]. Figure 3.19 shows the principle of XRD based on the Bragg model of diffraction[252].

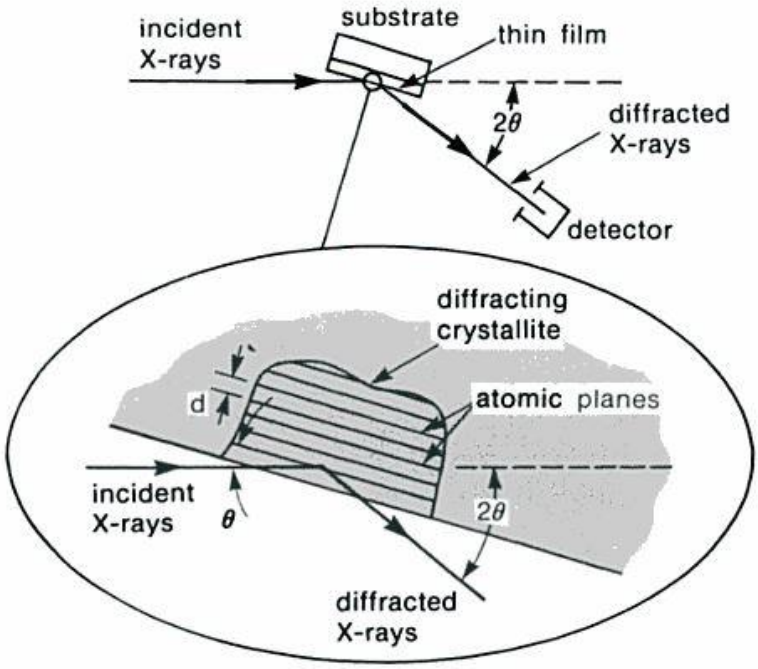

Figure 3.19 Basic features of a typical XRD [252].

In this model, Bragg's Law refers to the simple equation (11).

$$n\lambda = 2d\sin\theta \tag{11}$$

where the variable d is the distance between atomic layers in a crystal, and the variable λ is the wavelength of the incident X-ray beam while n is an integer, and θ is the incident Bragg angle.

The XRD was operated at 40 K and 25 mA using Cu Kα radiation with a wavelength of 1.5406 Å. Data was collected with step intervals of 0.05˚over 2θ in the range 10-90˚ for each GO sample with an acquisition time of 2s. Before XRD analysis, the samples were placed onto the sample holder followed by loading onto the sample plate in the XRD chamber. The crystal size of GO samples can be calculated by the Scherrer equation (12) using the full width at half maximum (FWHM) of XRD peaks.

$$\tau = \frac{K\lambda}{\beta \cos\theta} \tag{12}$$

where τ is the mean size of the ordered (crystalline) domains, which may be smaller or equal to the grain size, K is a dimensionless shape factor, λ is the X-ray wavelength, β is the FWHM in radians, and θ is the Bragg angle.

Chapter 4 Characterization of individual monolayer OrGO sheets

4.1 Introduction

A modified Hummer's method is the most commonly used procedure for the synthesis of GO. The modification is a pre-treatment step using phosphorus pentoxide and potassium peroxydisulfate in sulphuric acid to the pre-oxidize graphite. After the preparation of the pre-oxidized graphite by the strong acids and oxidants, hydrophilic GO sheets which can be well-dispersed in DI water are produced by Hummer's method. This uniform GO dispersion is then filtered through a membrane filter under vacuum to deposit GO sheets on the substrates or form GO paper. Although a variety of membrane filters have been used in vacuum filtration [14, 253, 254], Anodisc membrane filter is the most widely used by many of research groups [10, 50, 255-257].

The Anodisc membrane filter is an extremely precise membrane composed of a high purity alumina matrix that is manufactured electrochemically with high pore density and narrow pore size distribution. As a result, we used this alumina membrane filter to fabricate Al_2O_3/rGO composites by oxygen annealing without introducing any extra Al_2O_3 precursor. In other words, GO sheets are capable of growing Al_2O_3 NPs on their carbon basal plane by oxygen annealing after filtering through the Anodisc membrane filter. In order to understand the structure of monolayer TrGO and OrGO, optical microscopy, SEM, AFM, TEM and HRTEM were used for characterizations.

4.2 Results and discussion

4.2.1 Optical microscopy of OrGO layers

In order to image single layers, bi-layers or several layers of GO/rGO, various measurements are made using procedures such as optical microscopy, AFM, SEM and TEM. Normally, different layers of GO/rGO should be imaged by combining two or more of the above techniques. The optical microscope is primarily used to characterize GO/rGO samples as it is a low cost and non-destructive method in laboratories. Being a transparent material with the thickness in the nano-scale, it is necessary to mount GO on a SiO_2 substrate before annealing and carrying out optical imaging. Based on the research into substrate design to enhance the visibility of deposited thin films [258-260], the mechanism behind the contrast between rGO and substrate is explained in terms of the Michelson contrast (C) relation[261]:

$$C = \frac{R_{\text{material}} - R_{\text{dielectric}}}{R_{\text{material}} + R_{\text{dielectric}}} \tag{5}$$

where R_{material} is the reflected intensity from the material and $R_{\text{dielectric}}$ is the intensity without the material. If C=0, the material is “invisible” under the optical microscope; if 0<C<1, the material is brighter than the substrate, and if -1<C<0, the material is darker than the substrate.

SiO_2 is the most widely used coating material on silicon to enhance the distinguishing of graphene monolayers. Another governing factor that modulates contrast is the wavelength of the incident light. Blake *et al.* demonstrated that graphene layers can be

visualized on top of a SiO_2/Si wafer of with any thickness by using filters[262]. For ready viewing by naked eye, thicknesses of the SiO_2 coating of 90 and 280 nm are most appropriate when using green filters as well as white light. Consequently, the thickness of SiO_2 coating was 300 nm in our study.

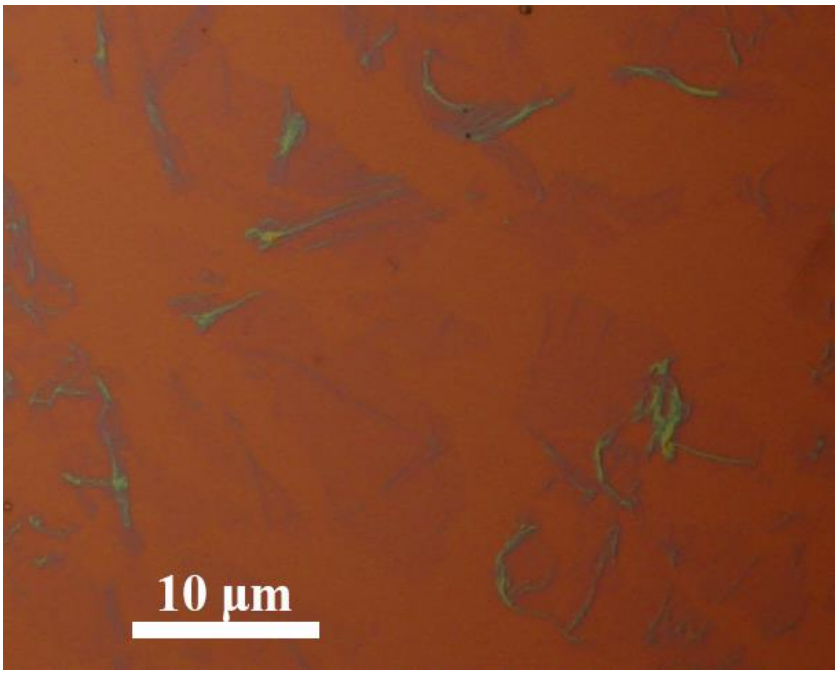

Figure 4.1 Optical microscopy image of GO at low magnification.

The optical image of GO on SiO_2/Si substrate shows the diameter of sheets ranging from a few hundred nanometers up to 20 µm, as shown in Figure 4.1. The drop-casting process deposited GO sheets onto the substrate with a large coverage density consisting of independent sheets.

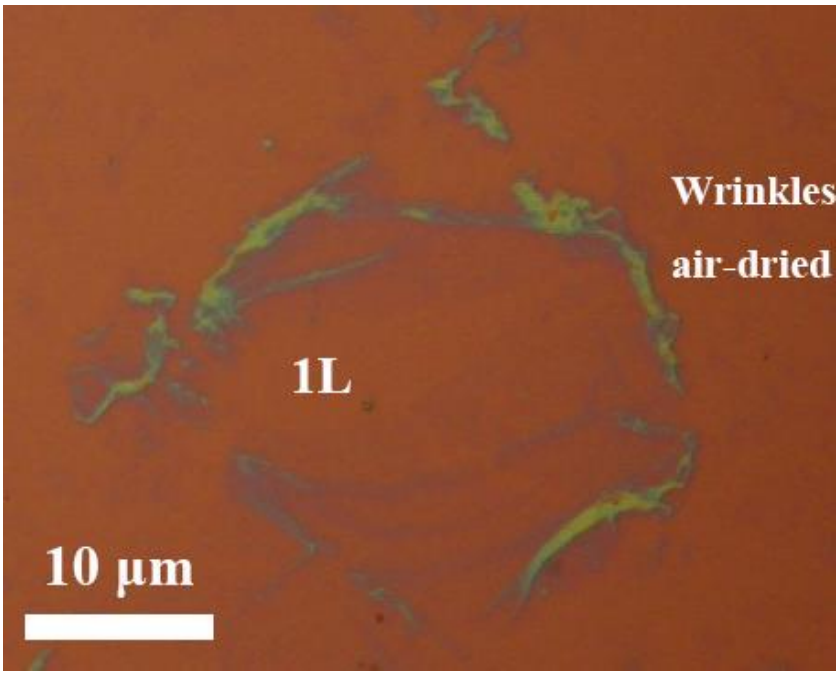

Figure 4.2 Optical microscopy image of GO at high magnification.

Investing an individual piece of GO sheet under the optical microscope however, we found residual water produced ring/wrinkle at the edge of the film although the samples had been dried in a glove box for 24 hours (Figure 4.2).

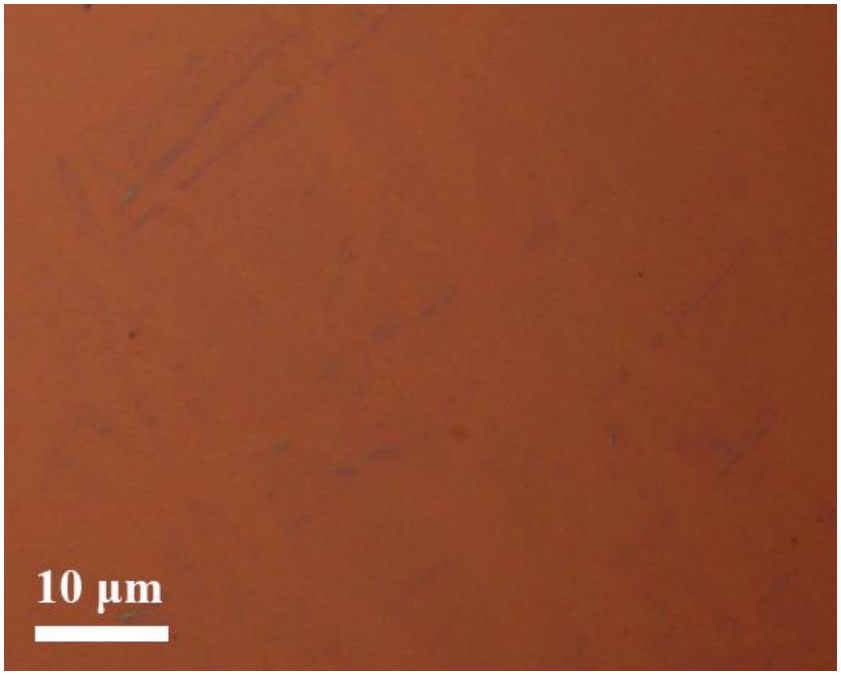

Figure 4.3 Optical microscopy images of OrGO at low magnification. Most of areas were coated by monolayer OrGO layers.

These amorphous wrinkles could be further dried by annealing under vacuum to form flat layers with small and narrow wrinkles, as shown in Figure 4.3.

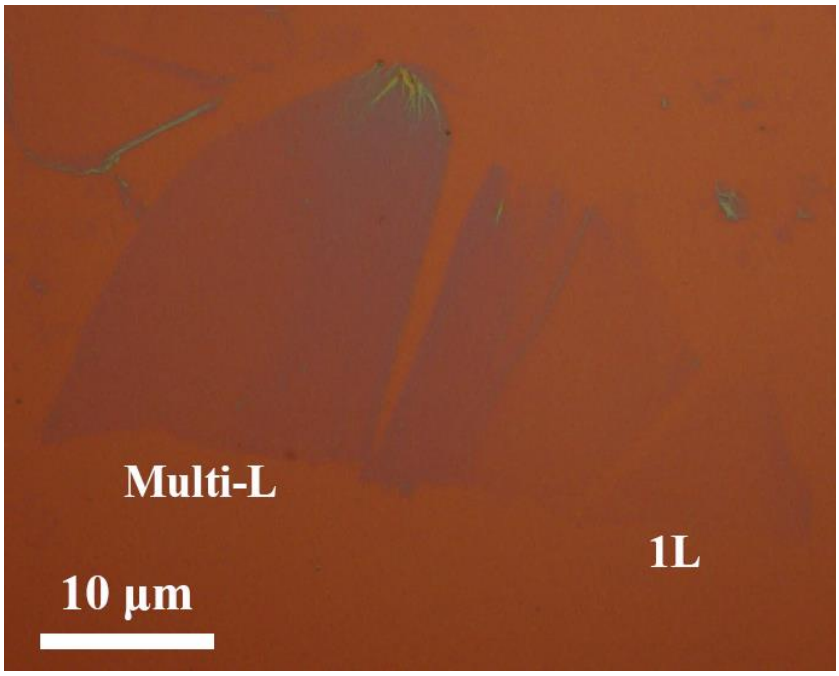

Figure 4.4 Optical microscopy image of TrGO at high magnification. The monolayer (1L) and multilayer (Multi-L) TrGO have different contrast to the substrate.

In order to detect the numbers of GO layers reduced by the physical exfoliation process, one sample was exfoliated with a conventional technique while another sample was treated with high speed centrifugation and probe ultrasonication at a very diluted concentration of 10 ppm. Figure 4.4 shows that normal peeled TrGO sheets were found to contain part of a single-layer GO and a multi-layer structure, indicating the traditional exfoliation process is capable of fabricating monolayer GO although it is difficult to reduce most multi-layer samples to single-layer structures.

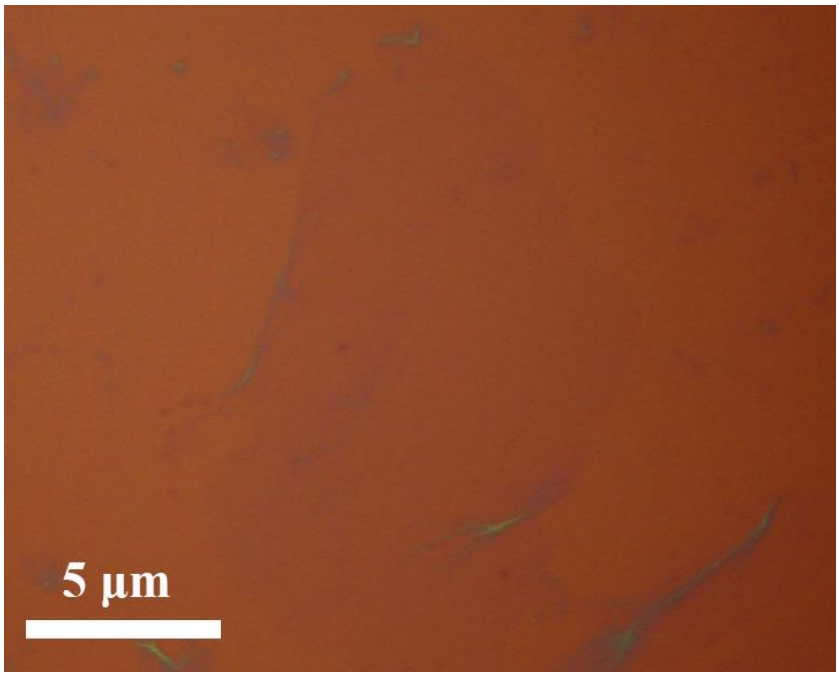

Figure 4.5 Optical microscopy image of OrGO at high magnification. The size of this monolayer OrGO sheet is around 10 µm.

Although wrinkles were still found in the monolayer OrGO under optical measurement (Figure 4.5), a new exfoliation process is a useful method to produce a single-layer GO contained dispersion which provides the opportunity for characterizing GO/rGO properties with a variety of measurements.

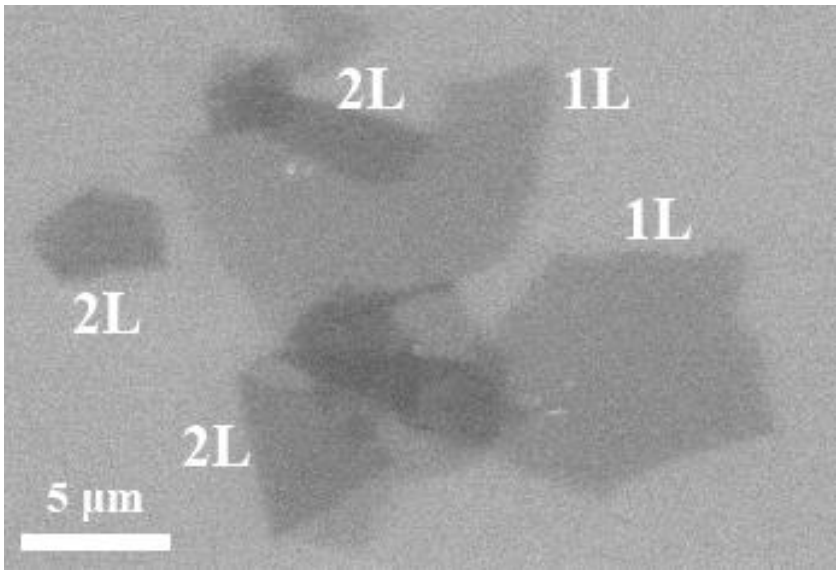

Figure 4.6 SEM image of TrGO deposited on the SiO_2/Si substrate. The abbreviations of "1L" and "2L" indicate the monolayer and bilayer areas of TrGO sheets.

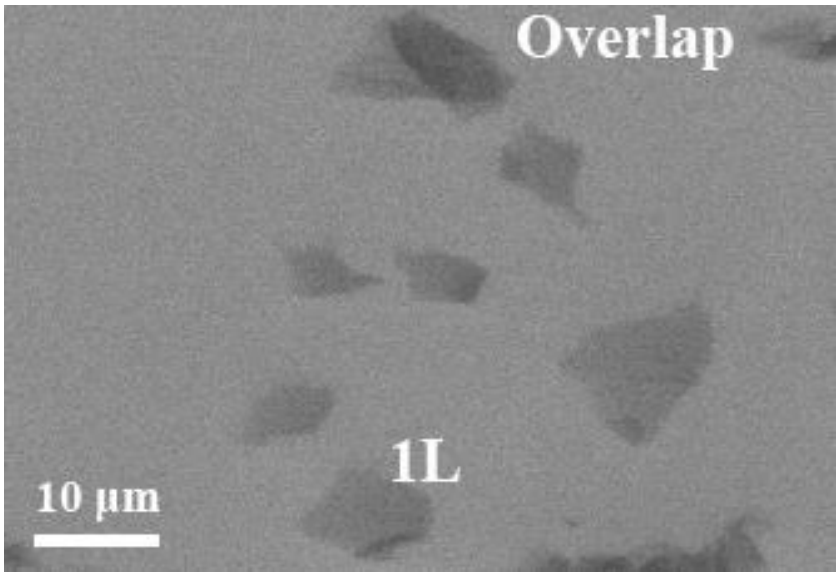

Figure 4.7 SEM image of OrGO deposited on the SiO2/Si substrate. The abbreviation of "1L" indicates the monolayer area of TrGO sheets. The overlapped multi-layer TrGO sheets have been marked as well.

The TrGO and OrGO samples have also been investigated by SEM. Figure 4.6 and Figure 4.7 show SEM images of TrGO and OrGO on SiO_2/Si substrates where monolayer, bi-layer and overlapped layers in samples are clearly visible.

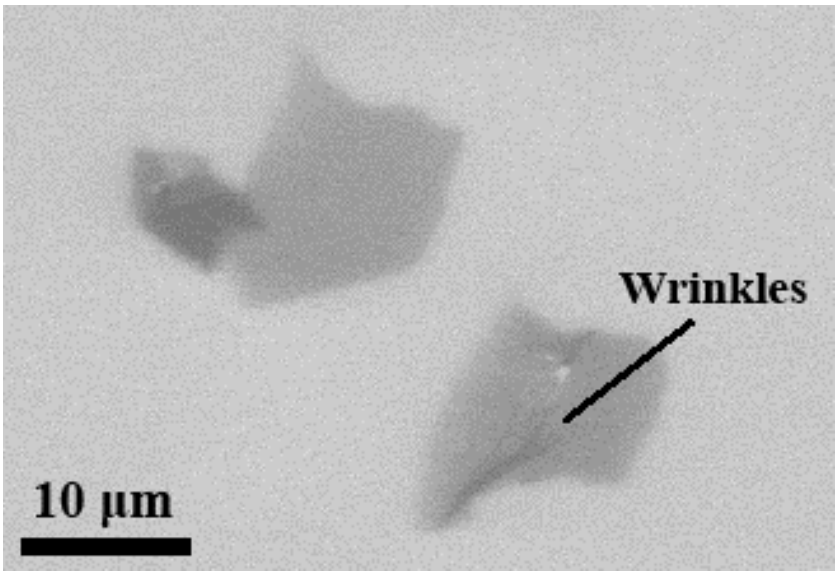

Figure 4.8 SEM image of TrGO deposited on the SiO_2/Si substrate. The wrinkles in monolayer sheet of TrGO are marked.

These SEM images show the two types of GO sheets are present: independent flat GO sheet with “wrinkles” and overlapped forms which are similar to the images under the optical microscope, as shown in Figure 4.8. The folding and overlapping areas of a single layer are less transparent under SEM. According to the above report, the wrinkles were produced by the thermal expansion coefficient difference between substrate and graphene sheets during the annealing process[9].

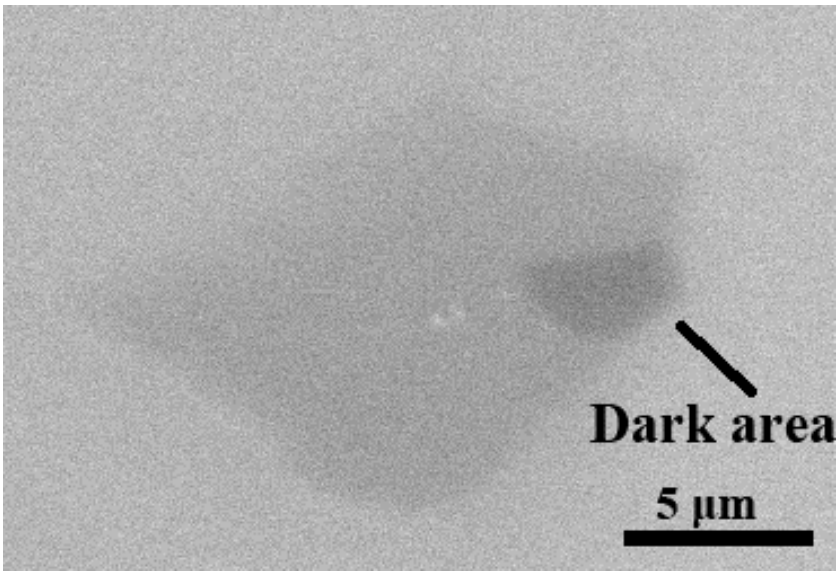

Figure 4.9 SEM image of TrGO deposited on the SiO_2/Si substrate. The multi-layer structure of dark area in monolayer sheet of TrGO is detected.

Further SEM analysis indicates the detailed information on individual TrGO flake about layer numbers and layer edge arrangement of the "dark" graphene flakes. Figure 4.9 presents some typical multi-layered graphene flakes attached to TrGO planes. The number of layers can be confirmed by the distinct contrast obtained in SEM images. However, a smaller distance between graphene edge structures limits the ability to identify the flakes of more than 3 layers. All grey flakes of the isolated TrGO on the SiO_2/Si substrate surface show single layer characteristics of graphene[263], while the darker areas indicate multi-layer GO features. These results suggest that most isolated GO sheets were single layer, which can be further confirmed by TEM and AFM height analysis.

4.2.2 TEM analysis of OrGO

One of the key innovations in this study was the fabrication of TEM samples by vacuum filtering an ultra-diluted GO dispersion through an alumina membrane filter, which allows suspended GO sheets to be deposited onto a holey TEM grid in a similar way to producing GO paper. This “simulation” process provides the opportunity to understand the structure and distribution of Al_2O_3 NPs on individual monolayers of OrGO planes. Moreover, fabrication of TEM samples by vacuum filtration enables a gentle transfer of GO sheets onto the TEM grid without using polymer support and their further removal with liquid solvents or thermal annealing [264].

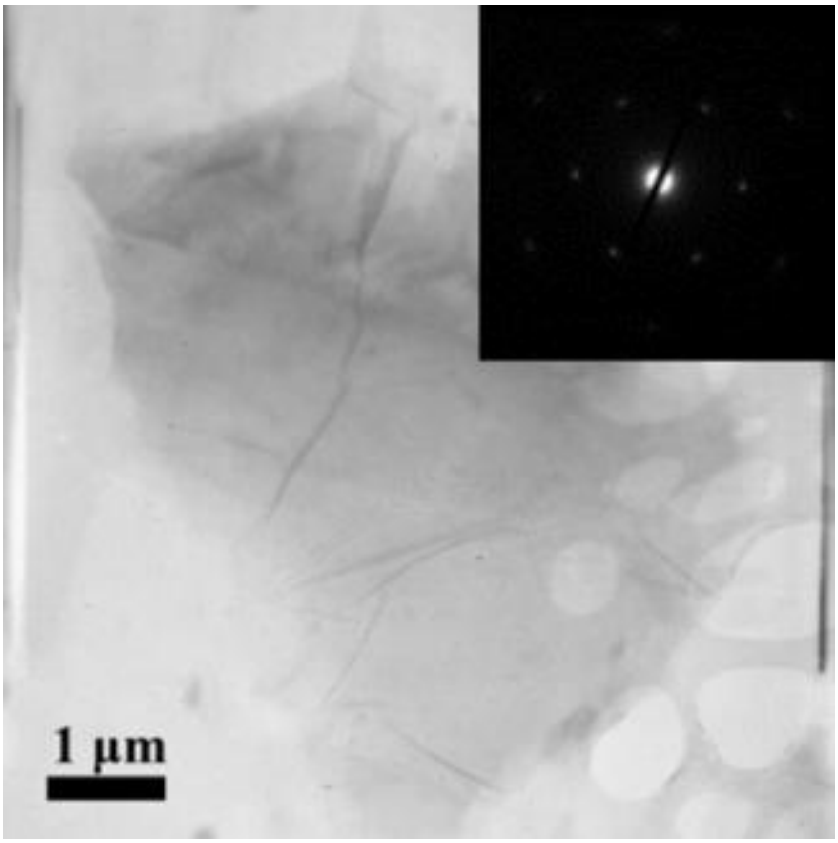

Figure 4.10 TEM characterization of TrGO. The inset shows the related SAED pattern. The number of graphene layers in a sheet can be easily determined based on related SAED pattern of the TEM.

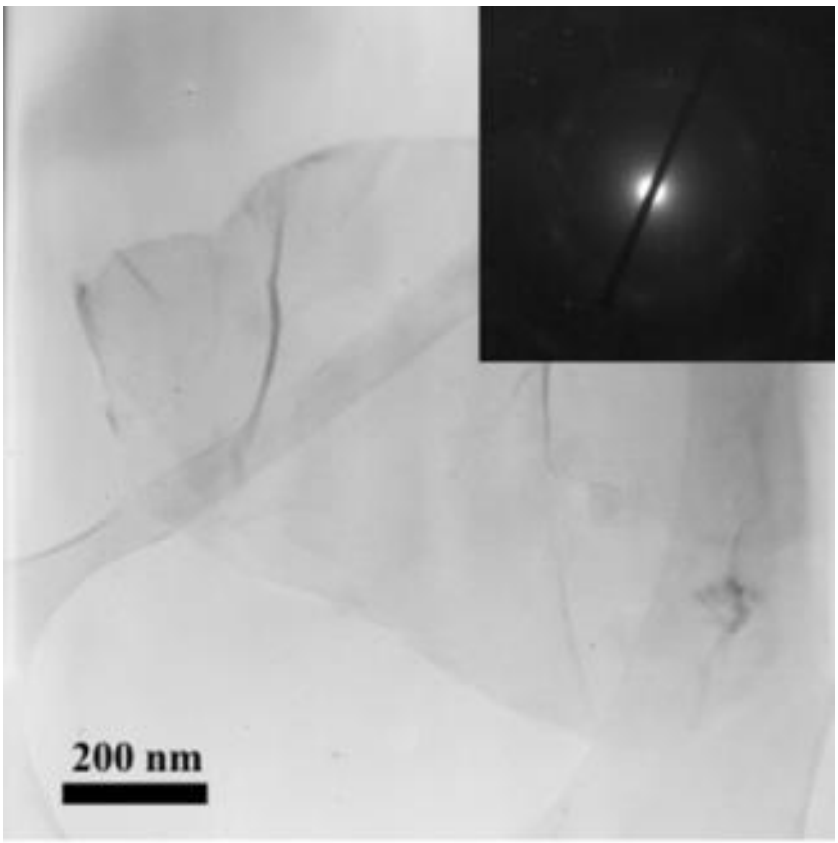

Figure 4.11 TEM characterization of GO. The inset shows the related SAED pattern.

Figure 4.10 shows an optical micrograph of a monolayer of TrGO sheet on the TEM grid with the coverage visible as grayish patches. Diffraction analysis was carried out to exhibit a hexagonal pattern, indicating a long-range orientational hexagonal order in the single layer of TrGO. Recent studies of graphene electron diffraction pattern [265, 266] have reported that the intensity of the diffraction spots could be interpreted as indicating the number of layers of a graphene sheet. The single-layer structure of graphene has the equivalent relative intensities between the inner and outer hexagons diffraction spots.

It is observed that the sheets are folded in some locations, and the number of graphene layers in a sheet can be easily determined based on the clear TEM signature provided by these regions. Folded regions are locally parallel to an electron beam, and single-layer TrGO has been found to exhibit one dark line, similar to TEM images of single-walled carbon nanotubes[267]. Compared with TEM analysis of TrGO, the SAED pattern of GO samples show diffraction rings and less resolved diffraction dots, indicating that the crystallinity of the graphene sheet has been significantly diminished before thermal annealing although both of these two samples have similar TEM images, as shown in Figure 4.11.

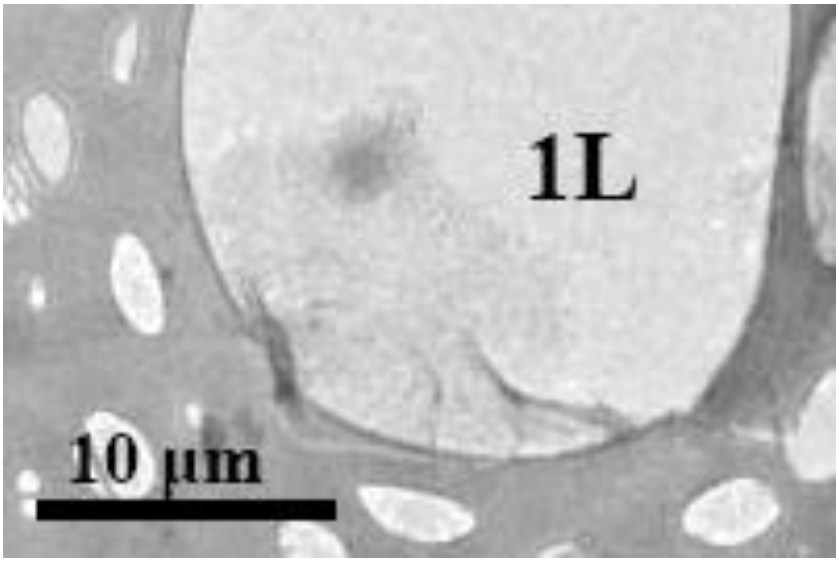

Figure 4.12 HRTEM image of OrGO deposited on the holey TEM grid. The abbreviation of "1L" indicates the monolayer area of OrGO sheet.

HRTEM was performed to determine the structure and distribution of Al_2O_3 NPs on OrGO sheets. Figure 4.12 shows a piece of monolayer OrGO partially covering the hole of a TEM grid. As in the optical images of TrGO, we have found dark area and wrinkles in the OrGO plane confirming the layered structure and shape of rGO are introduced by the exfoliation process and subsequent annealing process under vacuum. Therefore, oxygen gas used to produce OrGO has no influence on the layered structure and wrinkles of rGO.

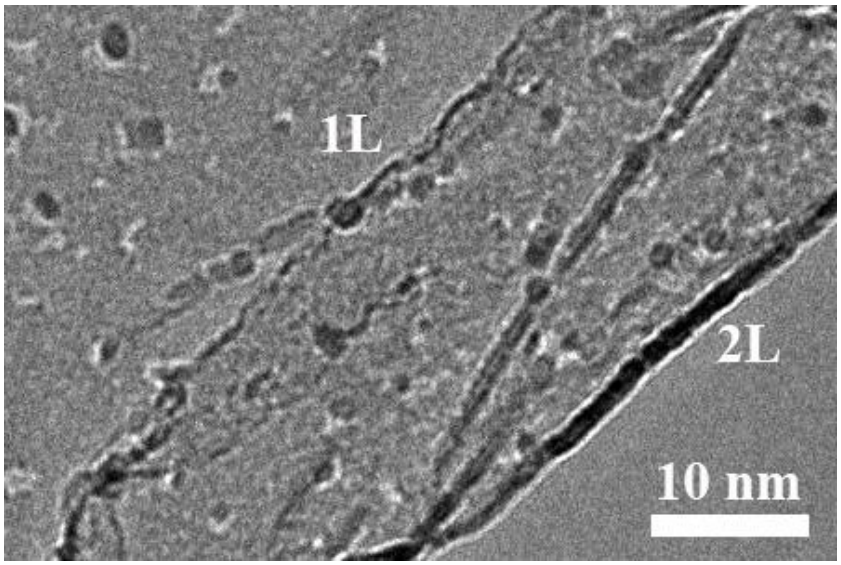

Figure 4.13 HRTEM image of folded bilayer area in OrGO at high magnification. The dark area and wrinkles confirm the layered structure of the OrGO.

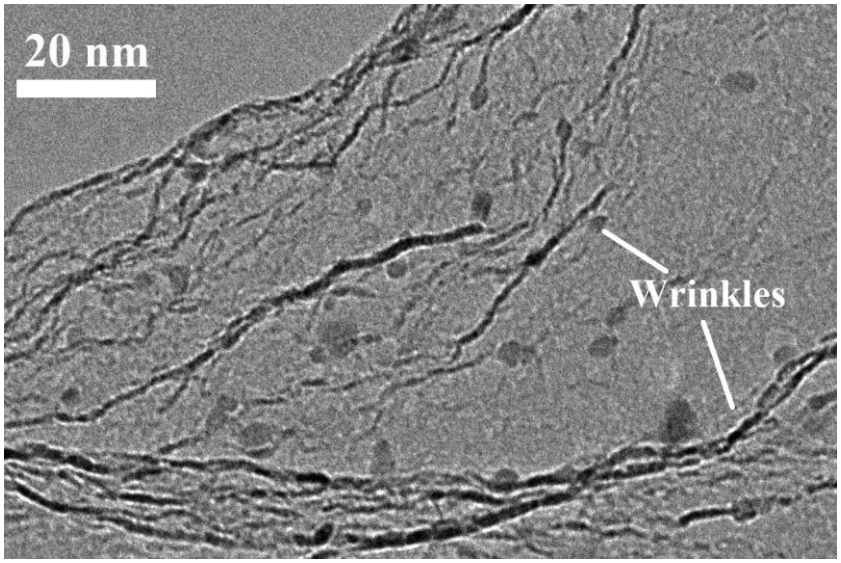

Figure 4.14 HRTEM image of monolayer in OrGO with wrinkles at high magnification.

Further evidence of the monolayer structure of OrGO was provided by analyzing the edges of single-layer and folded area, as shown in Figure 4.13. Folded monolayer (bilayer) sheets have been found to exhibit uniform multiple/thicker dark lines in folded regions, as in the case of multi-walled nanotubes[268] while the monolayer graphene sheets synthesized in our experiments have a single dark line. Figure 4.14

shows the same single dark line at the edges of unfolded monolayer structures where the wrinkles have a variety of width. Thus these two HRTEM images illustrate the different structure of edges, wrinkles and folded areas.

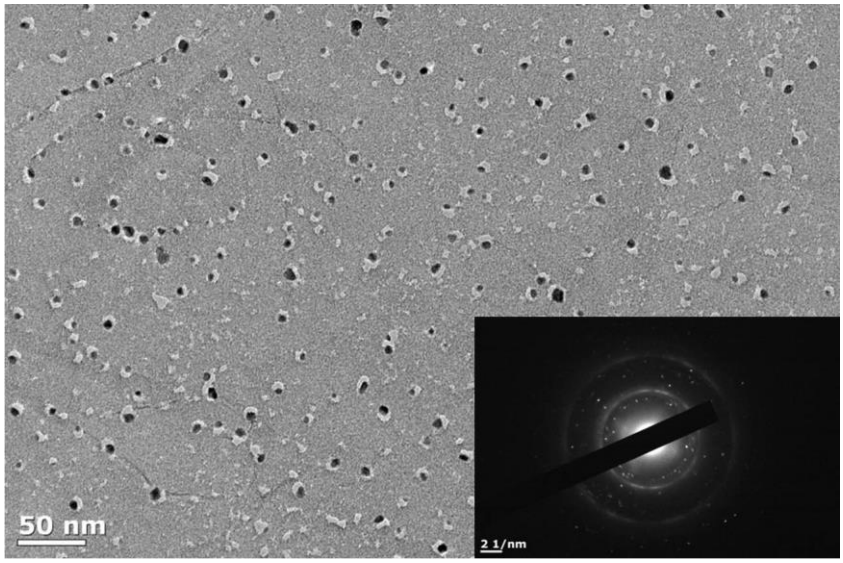

Figure 4.15 HRTEM image of OrGO showing the distribution of aluminium oxide NPs. The inset is the fast Fourier transform pattern of the selected region in OrGO plane.

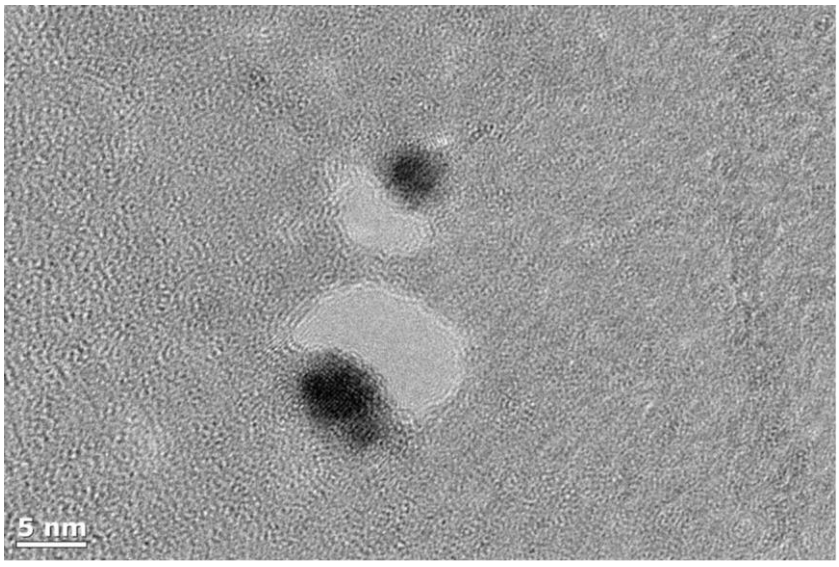

Figure 4.16 HRTEM image of Al_2O_3 NPs located at the edges of holes in OrGO plane. The particle sizes are less than 10 nm.

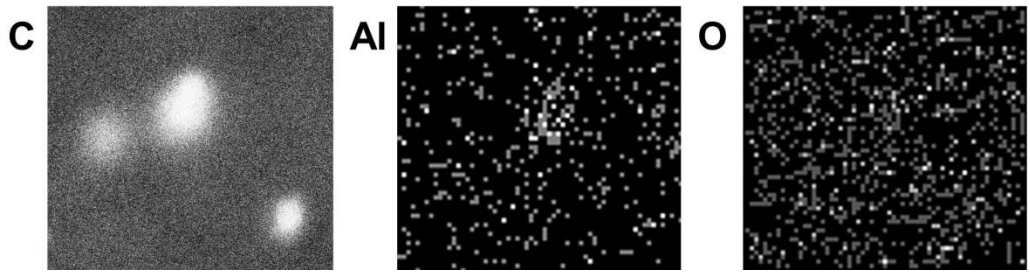

Figure 4.17 The EDX mapping of the NPs showing the components of NPs.

Figure 4.15 shows a homogeneous distribution of Al_2O_3 NPs on the OrGO plane. The inset is the corresponding selected area electron diffraction (SAED) pattern. More than 95% of the black spherical NPs, surrounded by flexible OrGO sheets, have an average particle size of less than 10nm. Higher magnification of this composite presents three major features: holes, graphitic regions and NPs (Figure 4.16). Holes or vacancies were possibly created by widely distributed carbon loss throughout the sheet where CO, CO_2, and water was formed and released during thermal annealing [16, 269, 270]. On the contrary, chemical reduction using hydrazine can partially recover the aromatic double-bonded structure of carbon by removal of oxygen functional groups without removing carbon [11, 77]. However, these defects may serve as adsorption sites to bind alumina molecules along the edges of the holes. Energy dispersive X-ray spectroscopy (EDX) mapping demonstrates a clear distribution of each element and that the black spots were rich in Al and O (Figure 4.17).

4.2.3 AFM analysis of OrGO

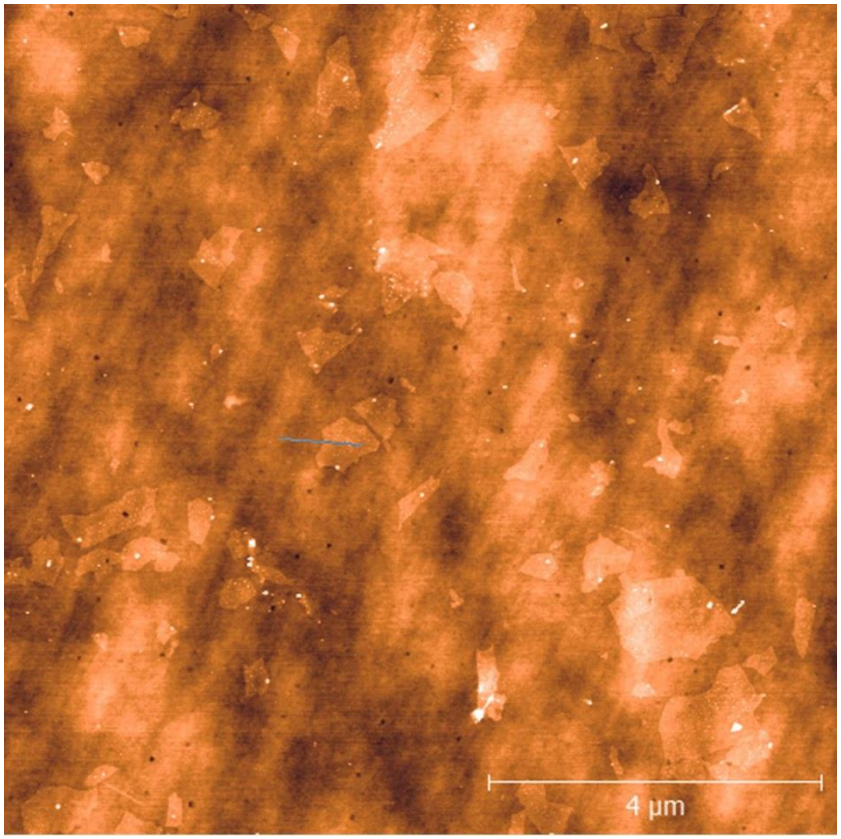

Figure 4.18 AFM image of OrGO sheets on 300 nm SiO_2 coated Si wafer. The average thickness of OrGO sheets is 0.7-0.8 nm, matching well with the reported apparent thickness of the as-exfoliated graphene.

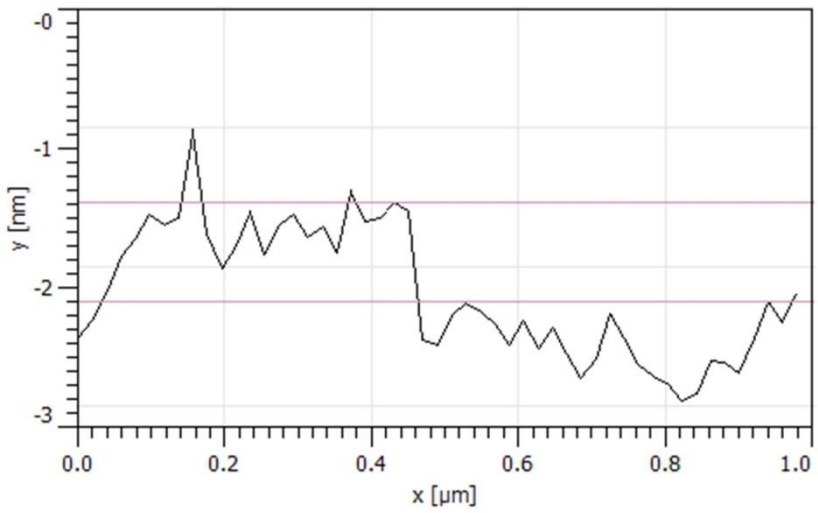

Figure 4.19 The corresponding height profile obtained from the line in Figure 4.18, indicating a single OrGO sheet.

Figure 4.18 shows an AFM image of alumina NPs decorated OrGO sheets deposited on SiO_2 substrate which are well dispersed with a lateral extent of a few hundred nanometers. The thickness of the individual OrGO sheets and the dispersion of the NPs can be visualized by the AFM operating in the tapping mode. The average thickness of OrGO sheets is 0.7-0.8 nm, matching well with the reported apparent thickness of the as-exfoliated graphene (Figure 4.19) [1, 10]. A great amount of AFM analysis confirmed that most of the flakes observed are single sheets.

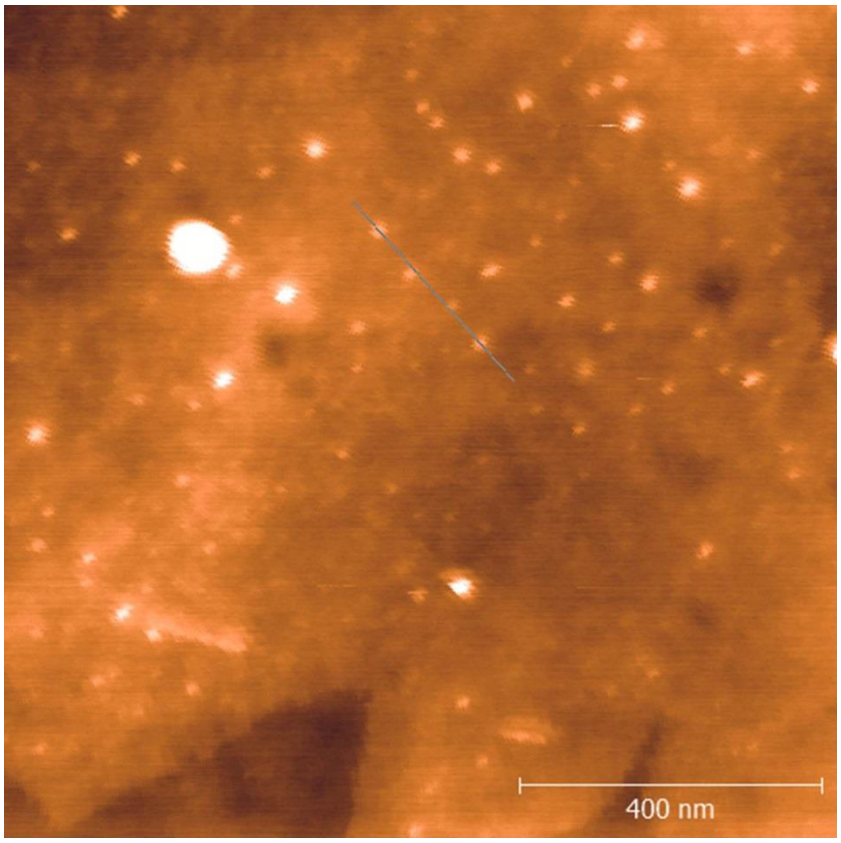

Figure 4.20 AFM image of Al_2O_3 NPs on OrGO sheet plane. The alumina NPs decorated OrGO sheets deposited on SiO_2 substrate which are well dispersed with a lateral extent of a few hundred nanometers.

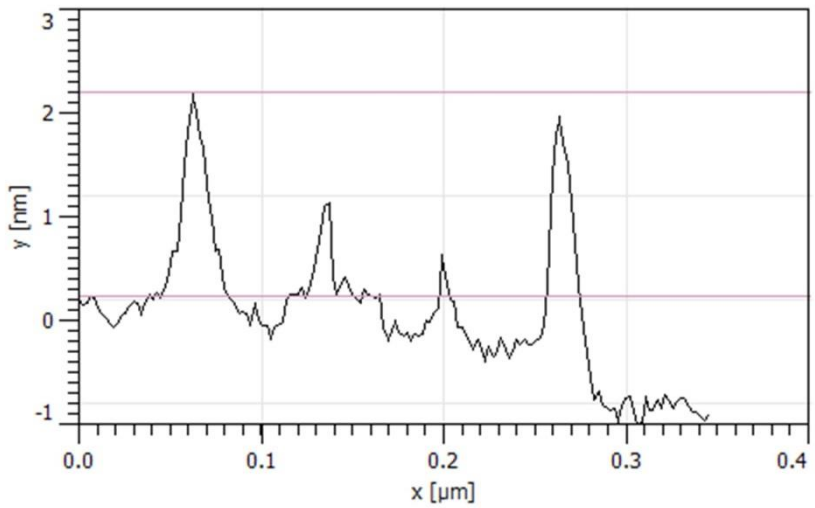

Figure 4.21 The corresponding height profile obtained from the line in Figure 4.20, indicating the height of Al_2O_3 NPs is less than 2 nm.

The AFM analysis further confirms the uniform distribution of Al_2O_3 NPs anchored on the OrGO plane (Figure 4.20). Besides the diameter being determined by HRTEM images, the height of NPs, as seen in height profile from line scan, is about 2 nm (Figure 4.21). Therefore, HRTEM and AFM analysis clearly elucidate the 3D architecture of OrGO. It is also demonstrated that the NPs are isolated from each other on single- or bi-layer rGO sheets with a typical high interparticle distance of between 60-80 nm, whereas the layer-to-layer distance is approximately 3.4 Å that is equal to the interlayer separation in graphite. Therefore, it can be concluded that our innovative exfoliation process can produce single-layer graphene. There are two reasons that the histogram (Figure 4.19) shows the average height of OrGO sheets is higher than graphene. First of all, as the AFM probe (~20nm) is larger than some of the scales, the tip is prevented from reaching the lowest point, resulting in an overestimate of the sheet thickness. On the other hand, the value of graphene is determined from layered bulk material. However, the van der Waals force is reduced for a single functionalized graphene

sheet on top of an Highly oriented pyrolytic graphite (HOPG) substrate[47]. Thus OrGO sheets on a SiO_2 substrate present an increased spacing [1, 271].

In order to confirm that the Anodisc membrane filter is the only source of Al^{3+} for the formation of Al_2O_3 NPs, rGO sheets filtered through mixed cellulose ester membranes have also been investigated by HRTEM (Figure 4.22). However, no NPs can be found on the rGO plane reduced by the same oxygen annealing process as in the fabrication of OrGO. These HRTEM images, along with the characterization of TrGO, indicate that the Anodisc membrane filter provides the Al^{3+} during the filtration and the oxygen annealing converted these ions to Al_2O_3 NPs on the rGO plane.

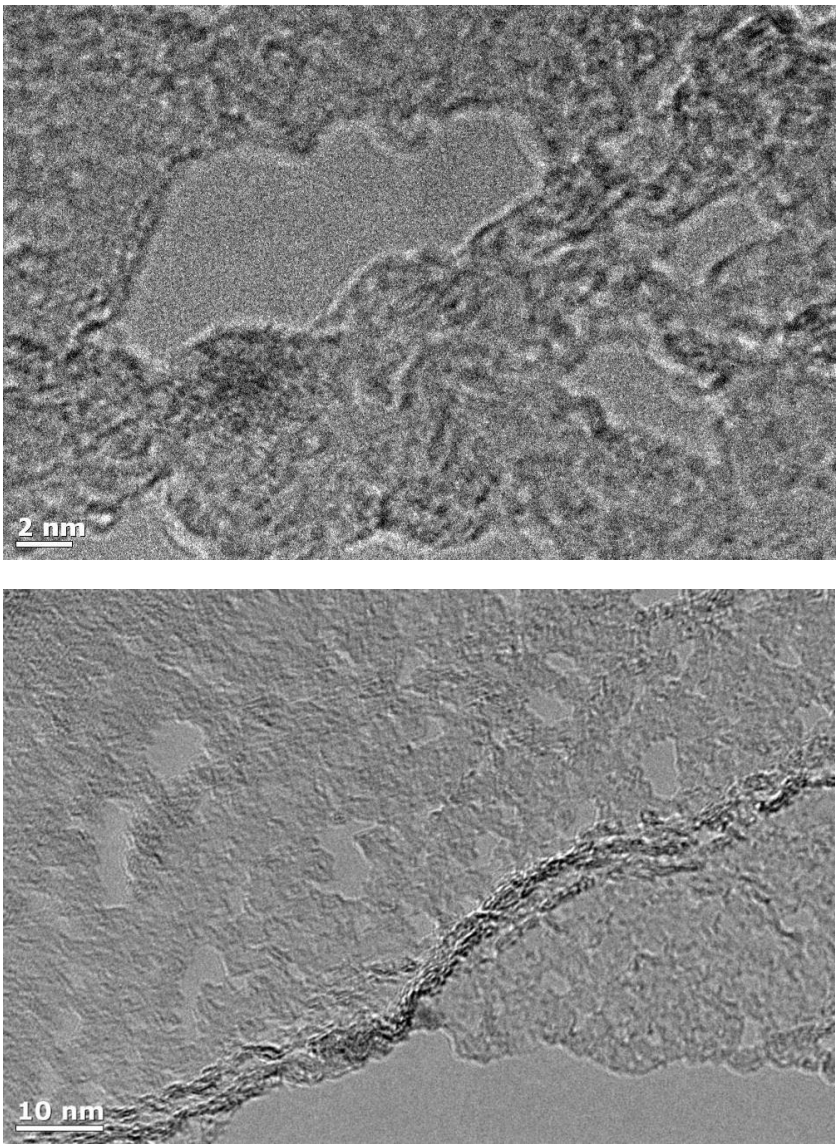

Figure 4.22 HRTEM images of rGO sheet filtered through mixed cellulose ester membranes and reduced by oxygen annealing. No any Al_2O_3 nanoparticle can be found on rGO plane.

4.3 Summary

GO allows rich chemical reactions both within the intersheet and along the sheet edges due to its layered structure and to the fact that it allows the attachment of a great number of oxygen functionalities such as epoxide and hydroxyl groups on the basal plane and carbonyl and carboxyl groups along the edges. Thus the structure can synthesize many graphene-based materials. The innovative exfoliation process using

high speed centrifugation and probe ultrasonication to reduce the number of GO layers has successfully produced monolayer GO sheets. TEM samples fabrication, by vacuum filtering ultra-diluted GO dispersion through an alumina membrane filter, easily deposited suspended GO sheets onto a holey TEM grid. The similarity between this process and that for preparing GO paper, provides the opportunity to determine the structure and distribution of Al_2O_3 NPs on an individual single layer of the OrGO plane.

A better understanding has been achieved by imaging GO, TrGO and OrGO samples with a variety of characterization methods such as optical microscopy, SEM, TEM, HRTEM and AFM.

(i) The monolayer structure of GO/rGO produced by the exfoliation process has been confirmed with the above mentioned measurements. The "grey" flakes of the individual TrGO samples shows a single-layer structure in SEM images while the darker areas indicates multi-layer features. The SAED pattern of TEM images shows the very obvious 12 diffraction spots with equivalent relative intensities between the inner and outer hexagons indicating the single-layer structure. The uniform single dark line at the edges of unfolded monolayer of OrGO HRTEM images further confirms the single-layer structure. Moreover, the height profile of AFM images provides further evidence of the single-layer structure of OrGO sheets.

(ii) The structure and formation of wrinkles in GO, TrGO and OrGO planes has also been analyzed. The wrinkles were introduced due to the difference of thermal expansion coefficient between substrate and graphene sheets during the annealing process. Unlike the uniform thickness of wrinkles at the edges of folded bilayer structure, the winkles in a monolayer GO/rGO sample varies in width.

(iii) The monolayer structure along with bilayer and overlapping multi-layer structure have been investigated in detail to establish a simple system for distinguishing the single-layer sheets.

(iv) The distribution and structure of Al_2O_3 NPs synthesized in OrGO have been characterized with HRTEM and AFM. The diameter of NPs is less than 10 nm with a typical high interparticle distance between 60-80 nm. The NPs are located at the edges of holes produced during the annealing process. Furthermore, height profiles of AFM images determined the height of NPs is less than 2 nm.

Morphology analysis established a fundamental understanding of the monolayer structure of GO, TrGO and OrGO samples which are the basic units in GO paper. The method we used for producing a single-layer GO dispersion provided a better process for the production of GO paper.

Chapter 5 Characterization of OrGO paper

5.1 Introduction

Although its good electronic, thermal, and mechanical properties allow for a range of possible applications[1, 72, 164, 272], graphene originally fabricated by the mechanical cleavage method lacks the ability to produce large quantities of the material, making it unrealistic for practical applications. Therefore, large-scale production of high quality graphene sheets is one of the difficulties to be overcome. Although a variety of methods to scale up graphene output have been investigated [20, 272, 273], the modified Hummer's method used by Ruoff and co-workers seems to provide an efficient way to fabricate large quantities of graphene. In this method, colloidal suspensions of individual graphene oxide sheets can be achieved by exfoliating in water, the graphite oxide which can be obtained in bulk quantities by oxidizing graphite [11, 14]. Furthermore, these GO sheets can be chemically functionalized, doped with NPs, and combined with polymer in GO dispersion to yield novel composites[164].

GO allows chemical reactions both in the inter-sheet and the sheet edges[274, 275] due to its layered structure containing a great number of oxygen functional groups such as epoxide and hydroxyl on the basal plane as well as carbonyl and carboxyl along the edges[62, 64]. These active functional groups provide places to synthesize many graphene-based materials. Additionally, individual GO sheets, which are prepared from GO, can be reassembled into thin films [276]or free-standing and

foil-like GO paper through flow-directed filtration of an electrostatically stabilized aqueous GO dispersion[163]. The resulting GO paper keeps all the functional groups and their native chemistry in the GO planes.

Even if GO paper could be obtained by an easy chemical method, its electrical conductivity could not be enhanced without thermal annealing which is considered to convert it into TrGO paper[132]. In order to produce functionalized graphene paper from graphene oxide sheets with enhanced electrical conductivity and to investigate the related properties, we envisioned two strategies to fabricate reduced GO paper based materials including thermal annealing and oxygen annealing. The characterizations consisting of SEM, TEM, XPS Raman spectroscopy and FTIR were used to reveal the mechanism in the formation of Al_2O_3 NPs on the rGO plane.

5.2 Results and discussion

5.2.1 SEM images of OrGO paper

GO paper was fabricated by filtering a GO dispersion containing separated monolayer GO sheets through an alumina membrane filter. After vacuum filtration, the resulting bulk material contained restacked GO layers with a different structure from graphite. In order to understand the morphology of GO/rGO paper, the raw material, individual pieces of HOPG were characterized by SEM. The graphene flakes were prepared using scotch-tape to repeatedly peel HOPG which were then deposited onto the SiO_2/Si substrate. The samples were then released in acetone followed by washing with an ample amount of DI water and propanol. After air drying, the substrates were

subjected to further cleaning in an ultrasound cleaner bath of propanol, removing most of the thick flakes captured on the wafer's surface. The remaining thin flakes were found to be attached strongly to the surface of the SiO_2/Si wafer, presumably due to van der Waals and/or capillary forces.

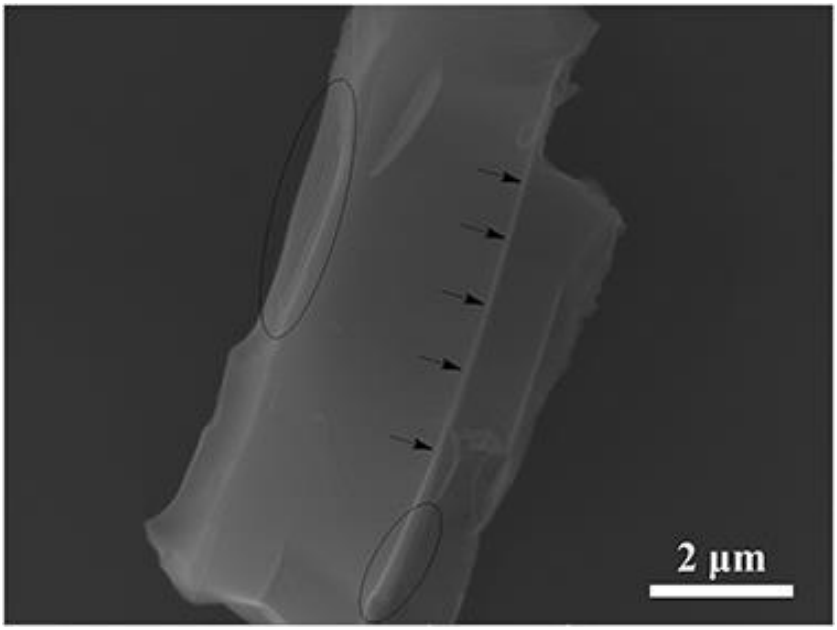

Figure 5.1 SEM image of graphite. The highly oriented lamella forms indicate the stacked layer structure of graphite flakes.

Figure 5.1 shows an individual piece of graphite flake with a stacked layer structure. The sample consisted of multiple-layered films (marked by the circles), which were uniformly oriented into lamella forms (marked by the arrows).

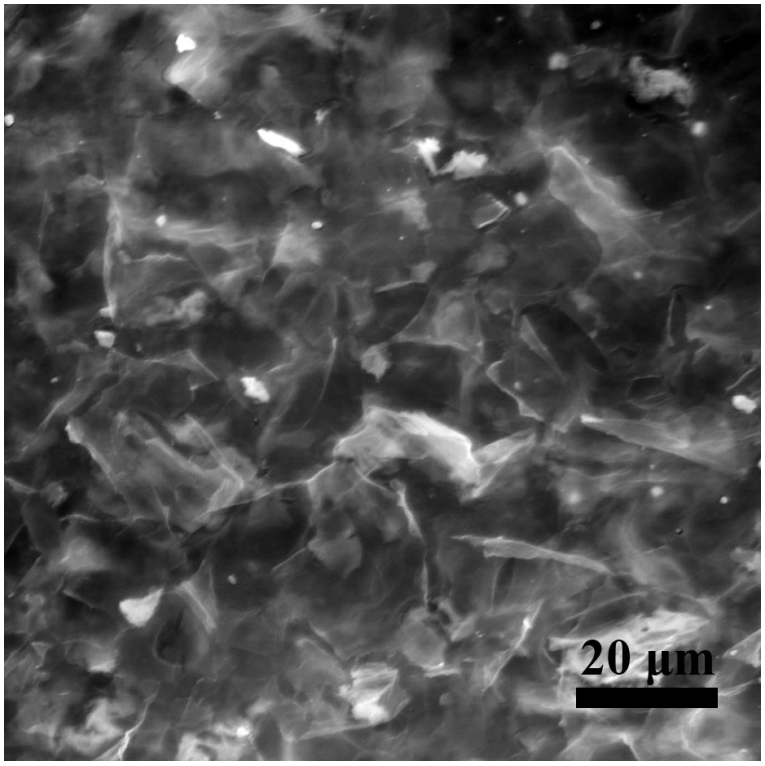

Figure 5.2 Top view of SEM image of GO.

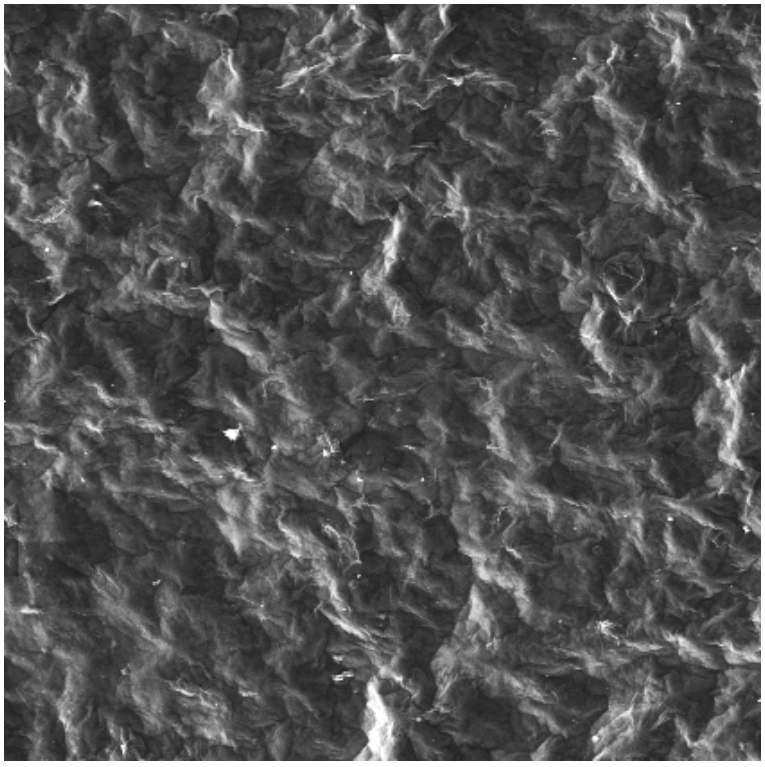

Figure 5.3 Top view of SEM image of TrGO. Vacuum filtration of GO dispersion produces a paper-like material with an interwoven structure in a nearly parallel manner.

The oriented stacked layers of graphite are easy to separate into small pieces due to their delicate structure, unlike the interwoven structure of GO paper where layers interweave with one another on a larger scale (Figure 5.2 and 5.3). As a result, GO paper is stronger than graphite foil and bucky paper made from carbon nanotubes[163]. Vacuum suction of a GO dispersion produces GO paper with an interwoven structure where individual layers shift over each other in a nearly parallel manner, the resulting layers therefore becoming flexible. In its solid form, GO sheets tend to form thin and extremely stable paper-like structures which can be stretched and folded, indicating that free-standing GO paper can be considered for applications such as flexible film batteries, hydrogen storage or electric membranes.

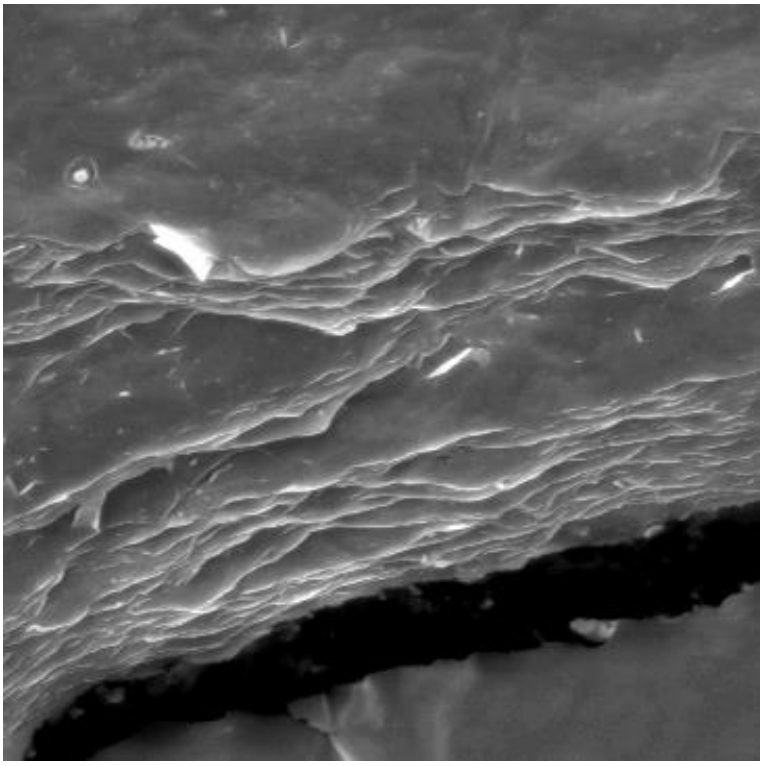

Figure 5.4 Cross-sectional view of SEM image of GO.

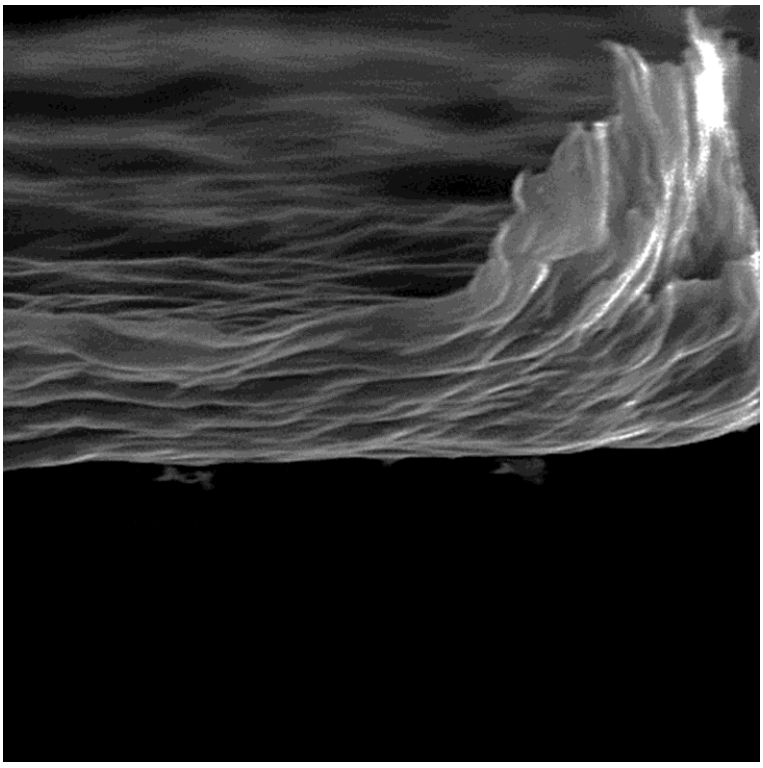

Figure 5.5 Cross-sectional view of SEM image of TrGO. TrGO paper has an apparently uniform and smooth surface with a well-packed layered structure due to removal of oxygen-containing functionalities.

When GO paper is reduced by thermal annealing, the resulting TrGO paper has an apparently uniform and smooth surface with a well-packed layered structure which allows the formation of a tighter package of sheets due to removal of oxygen-containing functionalities. Moreover, both sides of the as-prepared TrGO paper show a shiny metallic lustre (Figure 5.3) with a smooth surface under SEM, suggesting this material has a highly ordered macroscopic structure.

According to the above topography characterizations, the raw material graphite has a highly oriented layer structure while the individual layers of graphene stack in a nearly parallel manner. This flexible paper-like structures can be stretched and folded. Figure 5.6 shows the schematic of graphite and graphene layers decorated with Al_2O_3 NPs. However the mechanism behind the interlayer effects of NPs embedded graphene still remains unknown and further research is necessary.

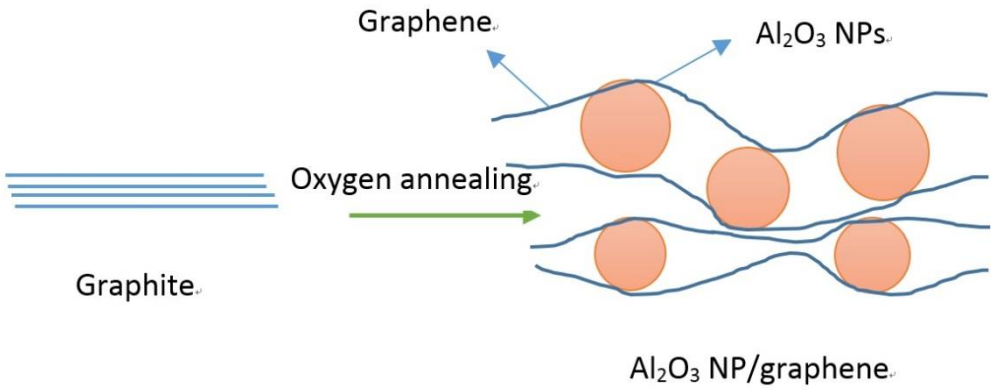

Figure 5.6 The schematic of graphite and graphene decorated with Al2O3 NPs. The paper-like graphene composite embedded with NPs are flexible and stretched.

5.2.2 XPS analysis of OrGO paper

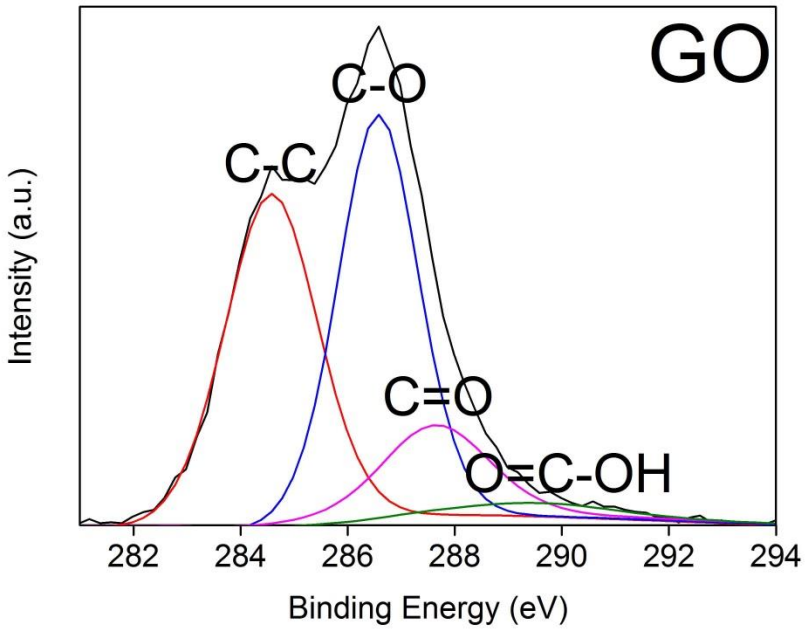

Figure 5.7 C1s XPS spectra of GO.

The chemical state of elements in the GO, TrGO and OrGO were extensively characterized by XPS. Figure 5.7 shows the two types of C1s band shapes which are usually mentioned in the literature concerning GO XPS data. The first one is a markedly asymmetric wide C1s band on the high-binding-energy side [11, 277]. The second C 1s band has two clear maxima in a relatively narrow band [253, 278]. In principle, the different proportions of chemical functionalities shown here may result from the different methods used to convert graphite oxide into graphene sheets. Moreover, the difficulty in electrically insulating samples in XPS measurement cause a surface charging effect on the graphite oxide resulting in a shift to higher binding energies in the XPS bands and this could be another reason for the differences. Additionally, graphite oxide is electrically heterogeneous on a local scale resulting in

differential charging. Above all, an artificially widened XPS band is introduced by the individual components of a given band in different compounds shifting to different extents.

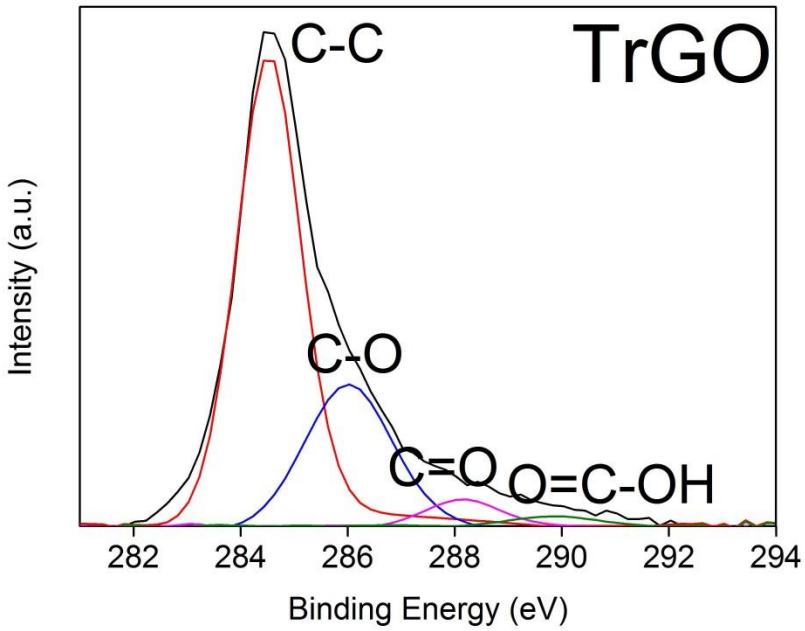

Figure 5.8 C1s XPS spectra of TrGO.

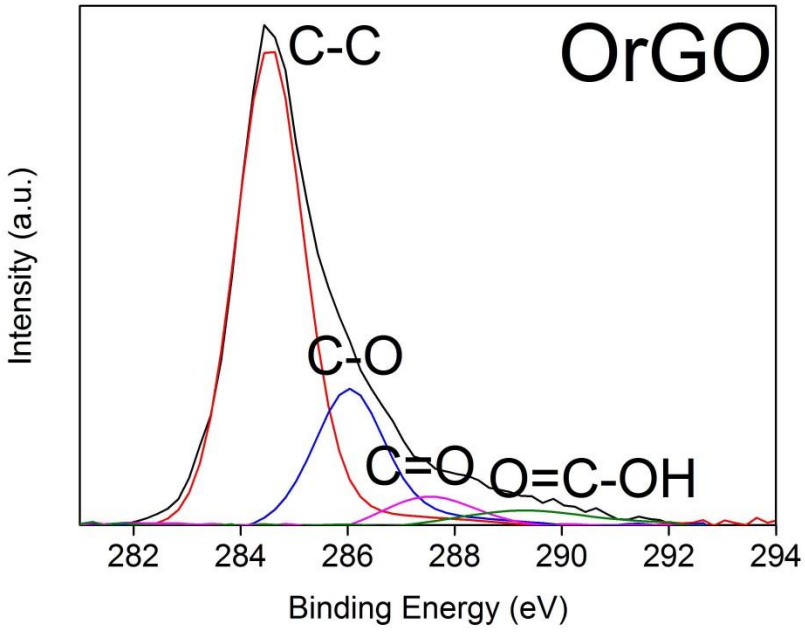

Figure 5.9 C1s XPS spectra of OrGO.

The binding energy of the C–C is assigned at 284.5 eV, Figure 5.7, and the binding energy at 286.5 eV, 287.6 eV and 289.6 eV are typically assigned for the C–OH, C=O, and O=C–OH functional groups, respectively [15, 279]. The peaks of oxygen functional groups are apparently decreased after the thermal annealing (Figure 5.8) and oxygen annealing process (Figure 5.9), the content of oxygenated carbon decreasing from 58.34% to 32.27% and 28.63%. The C-C peak corresponds to the number of sp^2 carbon components, while the oxygen functional groups corresponding to the amount of sp^3-hybridized carbon. The reduction efficiency can therefore be illustrated by the variation of the sp^2/sp^3 hybridization ratio [13, 67, 76, 280]. The sp^2/sp^3 ratios are 0.7, 2.1 and 2.5 for GO, TrGO and OrGO, respectively, indicating more oxygen functional groups have been removed during oxygen annealing. This result indicates that OrGO has a higher reduction efficiency than that of TrGO.

The shift of sp^2-carbon peaks in the XPS indicates a major modification of the electronic structures of graphene sheets due to the charge transfer between the graphene sheets and NP molecules [127, 281, 282]. It has been reported that the Fermi level of rGO, represented by the main sp^2-peak position in C1s XPS peak, should shift upward when the charge transfers from the NPs to rGO sheets due to covalent interaction. As a result, the C1s binding energy of the nanocomposite is increased [26, 282]. However, the OrGO XPS shows the C-C bond is very stable without any shift, indicating noncovalent interaction of Al_2O_3 NPs with the OrGO plane [24, 283].

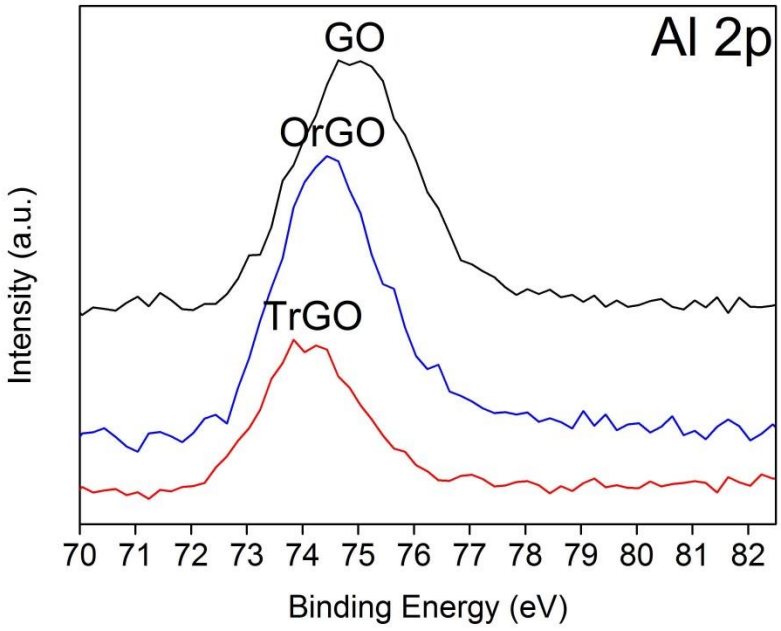

Figure 5.10 Al 2p XPS spectra of GO, TrGO and OrGO, respectively.

Figure 5.10 shows the High-resolution Al 2p XPS spectra of GO, TrGO and OrGO. After filtering the GO dispersion through an alumina membrane filter, the Al 2p scans of GO paper show an Al 2p peak at 74.5 eV that is nearly coincident with that of TrGO

(74.3 eV) and OrGO (74.5 eV). Thus it was extremely difficult to distinguish clearly between these three species using the primary aluminium photoelectron line.

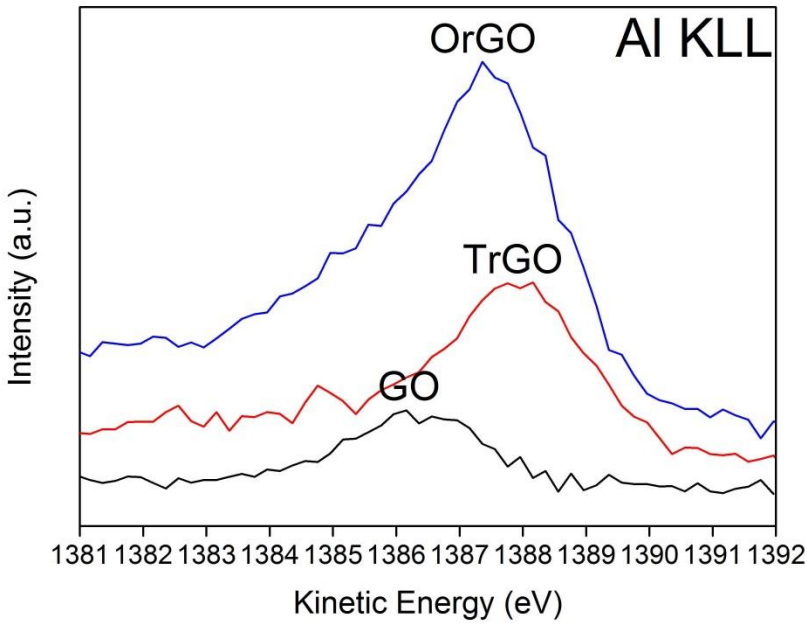

Figure 5.11 Al KLL XPS spectra of GO, TrGO and OrGO, respectively.

As a result, we collected high resolution spectra of the Al KLL Auger peak to further understand the element states of GO, TrGO and OrGO [284, 285]. The Al KLL Auger peaks were measured at a kinetic energy of 1386.8 eV (GO), 1387.8 eV (TrGO) and 1387.6 eV (OrGO) (Figure 5.11). The Al 2p and Al KLL energies indicate that aluminium incorporated in GO sheets is aluminium hydroxide ($Al(OH)_3$) which is then oxidized to form Al_2O_3 by thermal and oxygen annealing, respectively [286]. However, we could no visible NPs of Al_2O_3 in TrGO, indicating that oxidation of $Al(OH)_3$ occurred at a molecular level with no further aggregation of these molecules to form NPs by thermal annealing.

5.2.3 Raman spectroscopy analysis

Raman spectra is a non-destructive tool to characterize the structure of mono- and few layer GO such as thickness, defects and the degree of orderliness. In order to determine the structural changes in GO paper and reduced GO paper including TrGO and OrGO after thermal annealing and oxygen annealing, respectively, Raman spectroscopy was carried out to interpret the change in D, G, and 2D peaks around 1350 cm^{-1}, 1580 cm^{-1} and 2700 cm^{-1}, as shown in Figure 5.12.

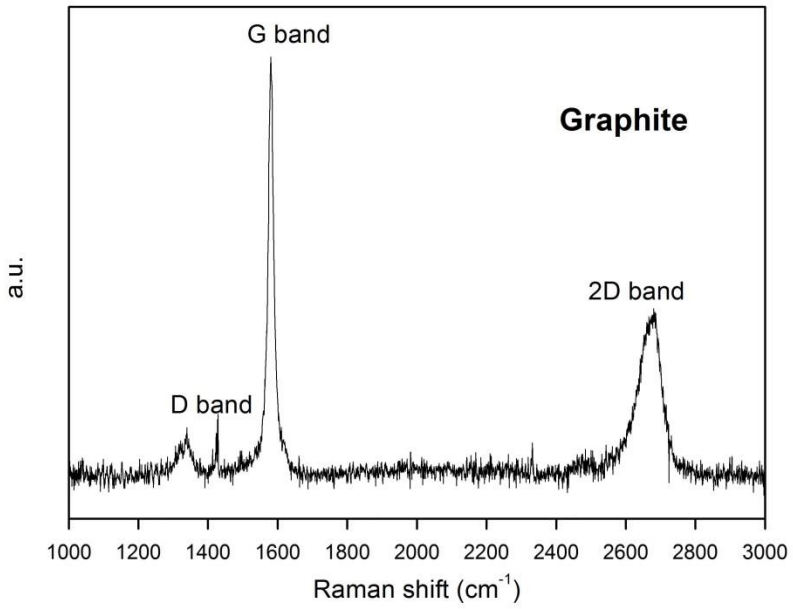

Figure 5.12 Raman spectrum of graphite shows the D, G, and 2D peaks around 1350 cm^{-1}, 1580 cm^{-1} and 2700 cm^{-1}

The G-band of graphite materials is associated with the doubly degenerate phonon mode (E_{2g} symmetry) at the Brillouin zone center[287], whereas the D-band is due to the in plane vibration of the sp^2 carbon atoms[288]. The D band, which indicates the defect density of the graphite material, appears to be due to the presence of atom

disorder in planes or edges as well as charge puddles and ripples. The 2D band, which is normally at double the frequency of the D band, represents the second order Raman scattering process. Compared with the graphite samples, the Raman spectrum of GO paper shown in Figure 5.13 represents a D peak with a higher relative intensity than the G peak, confirming the existence of defects after the chemical oxidation process.

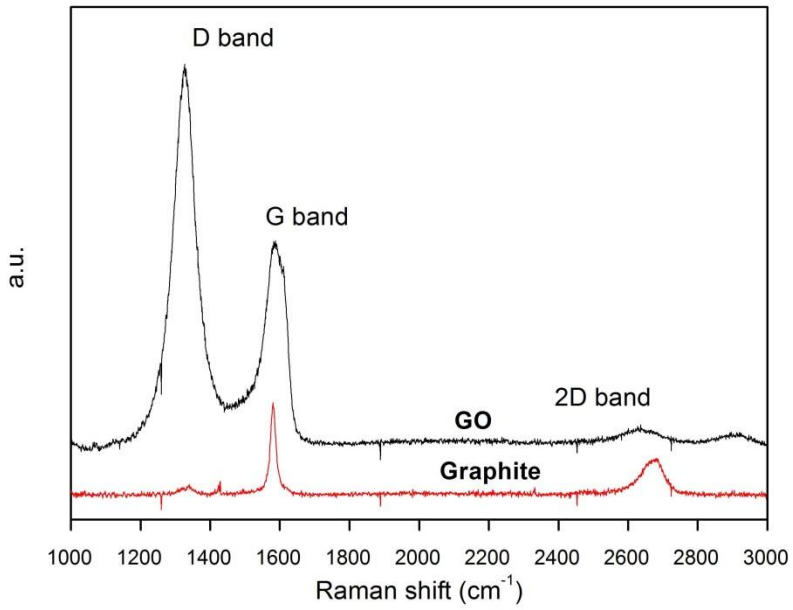

Figure 5.13 Raman spectra of graphite and GO show an obvious D band after chemical oxidation of graphite.

The intensity ratio I_D/I_G in Raman spectroscopy can be used to reveal the structural evolution whereby the sp^2 ring clusters contain sp^3 and sp^2 bonded carbon. The I_D/I_G values of graphite samples were lower than those for GO paper obtained by the modified Hummer's method, indicating that, by this method, part of the sp^2 carbon areas were oxidized to form sp^3 carbon. In addition, both G and D bands in the GO

Raman spectrum are broadened, indicating a disordered network of carbon atoms due to fractions of sp^3 carbons forming in oxidized graphite samples.

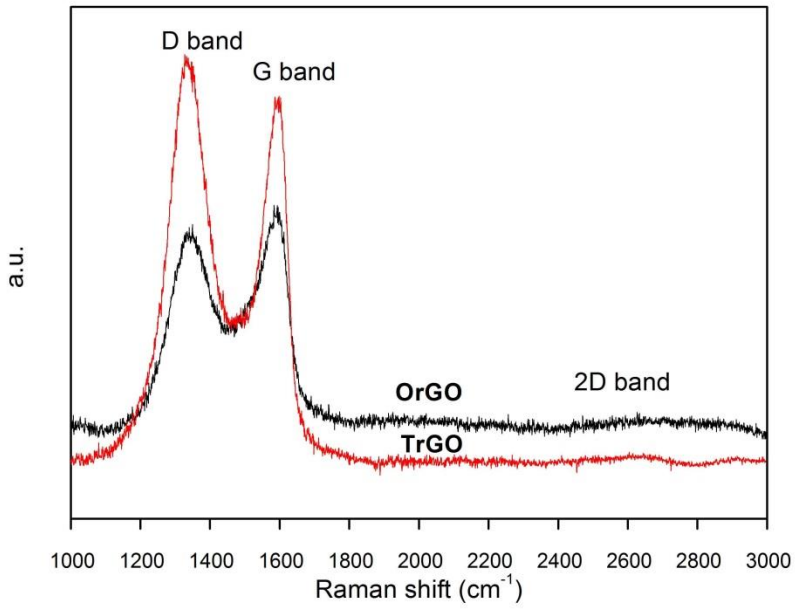

Figure 5.14 Raman spectra of TrGO and OrGO.

After reduction of GO paper by thermal and oxygen annealing, the degree of orderliness in the resulting TrGO and OrGO was characterized with the 2D-band shift and I_D/I_G ratio. Figure 5.14shows the 2D-band peak of OrGO has slightly shifted from 2692 cm^{-1} to 2697 cm^{-1}. Furthermore, the slightly higher I_D/I_G intensity ratio of TrGO indicates a possible smaller average size of the sp^2 domains. Compared with the G-band, the lower relative intensity of the D-band and its broader width indicates the higher orderliness of TrGO and OrGO papers. These phenomena suggest that traditional thermal annealing can remove oxygen functional groups from the GO basal plane during the thermal reduction process. However, the new graphitic domains have

smaller size but greater number than those of OrGO due to a slight decreasing in the I_D/I_G intensity ratio after our innovative oxygen annealing process. In another words, Al_2O_3 NPs growth under this oxygen annealing further removed oxygen functionalities in GO sheets. Table 5-1represents the ratio of sp^2 to sp^3 carbon areas in graphite, GO, TrGO and OrGO samples [287].

Table 5-1 sp^3/sp^2 carbon ratio by calculating I_D/I_G ratio

Graphite material	**sp^3/sp^2 ratio**
Graphite	0.101
OrGO	0.896
TrGO	1.116
GO	1.879

Distinct blue peak shifts for the D-band and the G-band were observed after the heat and oxygen treatment, which is usually attributed to the presence of isolated double bonds resonating at higher frequencies.

5.2.4 FTIR analysis

The structural changes of GO, TrGO and OrGO papers were also characterized by FTIR spectra analysis. Furthermore, this measurement provided information on Al_2O_3 NPs growth under oxygen annealing. For oxygen functional groups attached onto the GO sheet planes, the FTIR spectrum, shown in Figure 5.15 [278, 289, 290]. , illustrates the characteristic absorption bands corresponding to the C−O stretching at 1053 cm^{-1}, the C−OH stretching at 1231 cm^{-1}, the C−H stretching at 1389 cm^{-1} and the C=O carbonyl stretching from carbonyl and carboxylic groups at 1720 cm^{-1}.

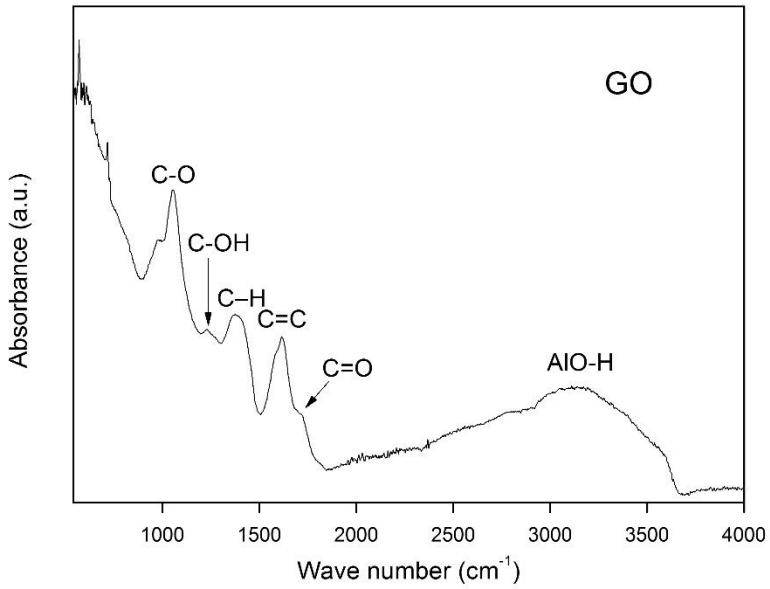

Figure 5.15 FTIR spectrum of GO

The GO spectrum also shows a C=C peak at 1616 cm^{-1} and this may be due to skeletal vibrations of unoxidized graphitic domains. After treating GO paper by thermal and oxygen annealing, FTIR peaks at 1053 cm^{-1}, 1231 cm^{-1}, and 1720 cm^{-1} of the resulting TrGO and OrGO papers are severely attenuated as to be almost undetectable, implying the removal of epoxide and the hydroxyl groups that were attached to the GO basal plane (Figure 5.16 and Figure 5.17).

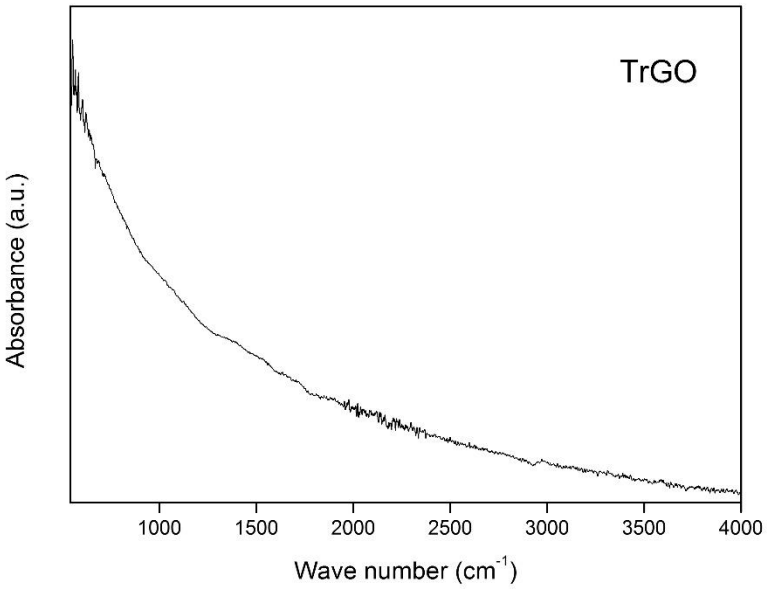

Figure 5.16 FTIR spectrum of TrGO

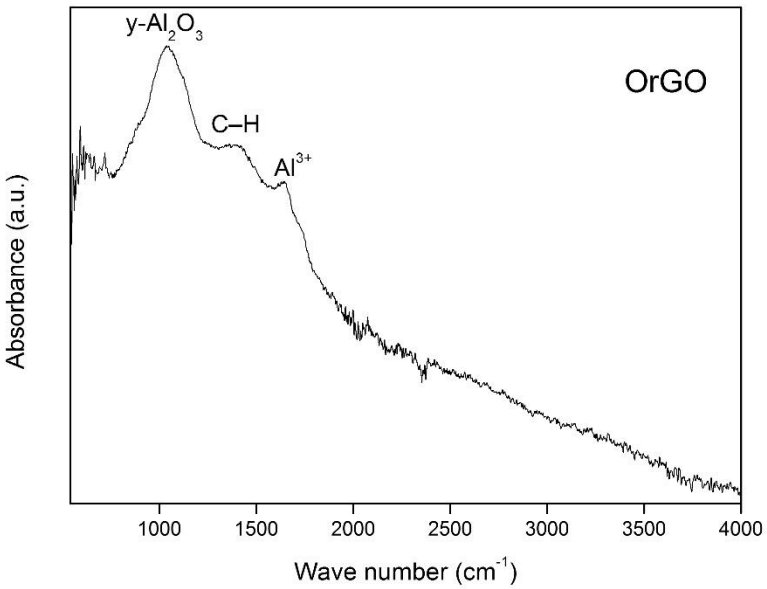

Figure 5.17 FTIR spectrum of OrGO

Moreover, the FTIR spectrum of OrGO reveals the process of Al_2O_3 NPs growth on the OrGO plane as shown by the absence of a broad absorbance between 2368 cm^{-1} and 3667 cm^{-1} resulting from AlO-H stretching vibrations. Concurrently, there is an

enhanced infrared absorbance centered around 1645 cm^{-1} [291] resulting from aluminium ions (Al^{3+}) and a broad absorption band at 1036 cm^{-1} [292] corresponding to the bulk phonon modes of y-Al_2O_3. It thus seems reasonable to assume that the AlO-H stretching vibrations are attributed to the molecules of $Al(OH)_3$ probably produced through the dissolution of Al_2O_3 in water[293, 294]. The heat treatment removed –OH along with some of the oxygen functional groups and the exposed active Al^{3+} reacted with oxygen molecules under oxygen gas flow to aggregate as visible NPs on the edges of holes in the OrGO plane due to the dangling bonds or oxygen functional groups located at the edges of the graphite lattice structure which energetically captured Al^{3+} ions to afford aluminum oxide growth[295, 296]. In other words, under oxygen gas flow, Al^{3+} ions are most likely to anchor at the highly reactive areas of structural defect edges promoting oxidation to form Al_2O_3 NPs. Unlike the aqueous chemical reduction of $AuCl_4^-$ ions used for gold particle/GO[297] or palladium acetate used for palladium NP/GO (/rGO)[298], which deposits the NPs mostly anchored on the functional groups of GO or the rGO plane, the oxygen annealing of Al^{3+}/GO in a vacuum chamber synthesizes the NPs at the edges of defects in OrGO sheets. According to the above analysis of XPS and Raman spectra, $Al(OH)_3$ molecules, formed by filtering the GO dispersion through an alumina membrane filter, reacted with the active dangling bonds sited at the edge of lattice structure defects to remove oxygen functional groups. The oxygen annealing which followed oxidized the $Al(OH)_3$ molecules and the resulting Al_2O_3 molecules aggregated to form visible NPs at the edge of holes. The aggregation of Al_2O_3 molecules enables more of the sp^3 carbon domain to be restored to sp^2 carbon

during the oxygen annealing process. Therefore, because of the use of a low temperature treatment during which no extra oxygen functionalities were introduced by oxygen gas flow, this oxygen annealing method increased the sp^2/sp^3 carbon ratio instead of oxidizing the carbon lattice structure.

5.3 Summary

A GO dispersion prepared from graphite by Hummer's Method, was reassembled into free-standing paper-like material through flow-directed filtration under vacuum. The resultant GO paper keeps all the functional groups and their native chemistry in its layered structure. Although GO paper can be obtained by an easy chemical method, it is still electrically insulating without thermal reduction. In addition, the structural integrity of the TrGO paper obtained in this way is affected by the thermal treatment so that holes in the lattice structure can be found in the TrGO sheet plane. As a result, we improved the traditional thermal annealing method by introducing an oxygen gas flow in the thermal reduction process to fabricate OrGO sheets in which the defective regions were recovered. In this method, colloidal suspensions of individual GO sheets can be produced by exfoliating the graphite oxide in DI water, namely Hummer's Method, resulting in GO sheets doped with NPs which are then formed into novel bulk paper-like composites via vacuum filtration through an Anodisc membrane filter.

A better understanding of these processes has been achieved by imaging GO, TrGO and OrGO samples with a variety of characterization methods such as SEM, XPS, Raman and FTIR:

(i) The results presented here demonstrate a convenient method for synthesizing Al_2O_3 NPs on rGO sheets with uniform particle size.

(ii) Upon the introduction of Al^{3+} as seeds anchored on the GO plane by vacuum filtration through an alumina Anodisc membrane filter, the Al_2O_3 molecules aggregated to form NPs and grew on the edges of holes or vacancies during thermal annealing.

(iii) XPS spectra confirm the reduction efficiency of TrGO and OrGO as well as the element states of aluminium in GO or rGO plane.

(iv) The Raman and FTIR results reveal dangling bonds or oxygen functional groups of GO binding to the Al^{3+} to allow aluminium oxide aggregates and growth which lead to a further reduction.

Chapter 6 Properties of OrGO paper

6.1 Introduction

The study of the electronic properties of OrGO paper promises to open new opportunities for the manufacture of industrial electronic devices. We have shown that GO-based paper-like material can be synthesized by chemical exfoliation of graphite using an oxidizing agent and then dispersion in DI water, down to single sheets through ultrasonication and centrifugation followed by filtration. It may be possible to implement this process on an industrial scale. The challenge of GO paper implementation is restoring electrical conductivity which is dramatically lowered to insulation after oxidation of graphite.

Previous electrical conductivity research of graphene has been intensively carried out on individual sheets. These experimental measurements [299-301] enable us to understand the electrical conductivity properties of two-dimensional graphene based materials. In order to achieve large-scale production of electrically conductive graphene based materials to meet industrial requirements, more attention has recently focused on highly disordered GO papers [67, 77, 131, 253].

As a non-stoichiometric compound, GO sheets consist of both sp^2-hybridized and sp^3-hybridized carbon atoms, such as hydroxyl and epoxide functional groups on either side of the basal plane, and carboxyl and carbonyl groups at the edges. The properties of GO are attributed to the conditions of synthesis and following treatments. The missing carbon atoms (holes or vacancies) in the hexagonal ring-based carbon

network and the corrugation of sheets are formed by local chemical structure where the saturated sp^3 bonds and their bonded electronegative oxygen atoms as well as other "defects" enhance the energy gap in the electron density [302], resulting in GO becoming non-conducting. Therefore, in order to modify these structural and electronic properties, the recent focus has been on attempting to enhance the electrical conductivity of chemically oxidized GO sheets by a variety of chemical and thermal processes[67, 77, 131, 253].

In this section, we explore the electrical conductivity of TrGO and OrGO papers, respectively, to understand how the reduction process affects the electronic properties. We designed short-time annealing experiments to investigate the efficiency of heat treatment on GO paper. The results of these experiments provide more details on the improvement of electrical conductivity of TrGO and OrGO papers by this method rather than the use of a long-term reduction process to achieve the highest electrical conductivity value.

Water wettability of various graphitic surfaces, for instance, graphite and carbon nanotubes ae currently intensely studied. The wettability of graphite is commonly accepted to be between 84–86 ° which is also used to calibrate the force field for water–graphite interaction [303-306]. The wettability of the outside surface of carbon nanotubes obtained from the wetting force measured of an individual carbon nanotube was 80.1 ₹[307]. Additionally, water molecules can be transported into a

single-walled carbon nanotube at high speed, indicating that carbon nanotubes have a hydrophilic interior surface with small-diameter [308-310].

The environmental compatibility of the surface of these materials is normally determined by formation of hybrid materials, coating and composites which affect the surface charge and wettability[132]. Even though the surface properties play a key role in practical applications, limited research has been done on rGO surface properties. Herein, the wettability of TrGO and OrGO papers is investigated by measuring the water contact angle to understand more about Al_2O_3/rGO structure.

6.2 Results and discussion

6.2.1 Electrical conductivity of OrGO

6.2.1.1 Electrical conductivity recovered by oxygen annealing

GO paper is nonconductive and its resistance values were beyond the measuring range of our electrical conductivity equipment. The electrical conductivity of TrGO and OrGO was measured in five places for one sample, five samples being taken for each material. The results show that OrGO has a higher electrical conductivity at 7250 S m^{-1} than that of TrGO at 5900 S m^{-1} (Table 6-1). In addition, the measured values of TrGO paper are mostly in the range of 4500-5500 S m^{-1} while OrGO samples have a narrower range of electrical conductivity - mostly between 6500 and 7250 S m^{-1}, indicating a more uniform structure and a better reduction level of OrGO produced by oxygen annealing (Figure 6.1).

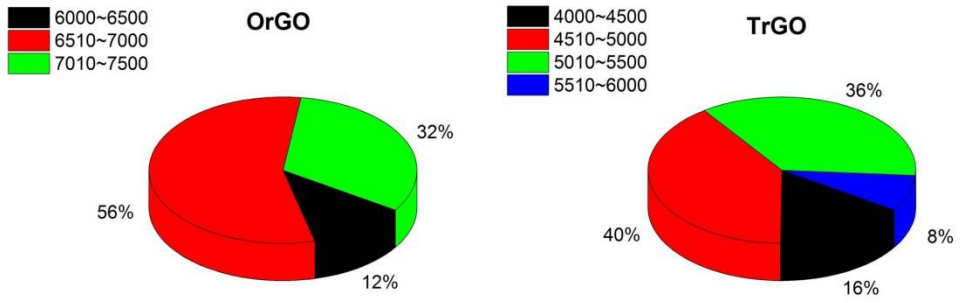

Figure 6.1Percentage of the electrical conductivity in the different ranges for OrGO and TrGO.

Table 6-1 Electrical conductivity (S m^{-1}) of TrGO and OrGO produced with low temperature ramp rate at 2 ^{O}C/min under vacuum.

Samples No.	TrGO (S m^{-1})	OrGO (S m^{-1})
1	5480	6690
	4830	6270
	4320	6480
	4750	7190
	5900	6180
2	4340	7080
	4960	6810
	4570	7250
	5650	7090
	5190	6970
3	4950	6740
	5330	6850
	4480	6980
	5120	7150
	4880	6570
4	4820	7050
	5260	6820
	4920	6790
	4480	6680
	5390	7210
5	5350	6740
	5270	6890
	4930	6830
	5090	7160
	4780	6650

GO containing both sp^2 and sp^3 carbon networks can be considered as possessing a quasi-two-dimensional structure where the amorphous sp^3 regions functionalizing GO sheets with hydroxyl−hydroxyl and hydroxyl−epoxide hydrogen bonding interactions[311]. Paci *et al.* simulated the molecular dynamics of hydrogen bonding and revealed that the high tunnel barriers between the sp^2 carbon networks were formed by disordered sp^3 bonded structures [312]. Therefore, heat treatment forces more individual sp^2 regions to be connected by removing functional groups to form a two-dimensional graphene plane. According to the analysis of TrGO and OrGO sheets in Chapter 5, the significant increase in the electrical conductivity of OrGO can be presumably attributed to more of the graphitic network of sp^2 bonds being restored by oxygen annealing reduction. The better electrical conductivity results for OrGO paper are likely associated with the higher sp^2/sp^3 carbon ratio caused by Al_2O_3 NPs aggregated at the edges of defective regions in the OrGO plane during oxygen annealing.

When paper GO is reduced by thermal annealing, the removal of oxygen functionalities allows a tighterpacked structure for TrGO sheets. Evolving gas such as CO and CO_2 molecules would disturb this packed structure and prevent TrGO sheets from forming a well-ordered structure, as seen in SEM images of TrGO paper (section 5.2.1). However, the formation of Al_2O_3 NPs can alleviate this issue. The NPs present in the interlayer maintain a larger intersheet spacing and allow the emission of evolved

gas molecules out of the stacked OrGO sheets with a minimal disturbance of the initial sheet packing order.

As a result, the values and ranges of electrical conductivity of OrGO reveal that the formation of Al_2O_3 NPs on OrGO sheet planes produce a uniform restacking structure of rGO sheets with a higher sp^2/sp^3 carbon ratio.

6.2.1.2 Short duration reduction for GO paper

Although electrically insulating GO paper can be reduced by thermal or oxygen annealing at 400 ^{O}C for 30 minutes to fabricate electrically conductive TrGO or OrGO, the details of this conversion from insulating to conducting during the 30 minutes annealing are still not clear. As a result, we designed short-duration annealing experiments to fabricate TrGO and OrGO to investigate the reduction mechanism in this process. Unlike the process described in section 3.5 and 3.6, the short-duration annealing was carried out for only 30 minutes without vacuum. In addition, for extra control and detail, the samples were put in the furnace at the desired temperature and taken out and examined every 5 minutes.

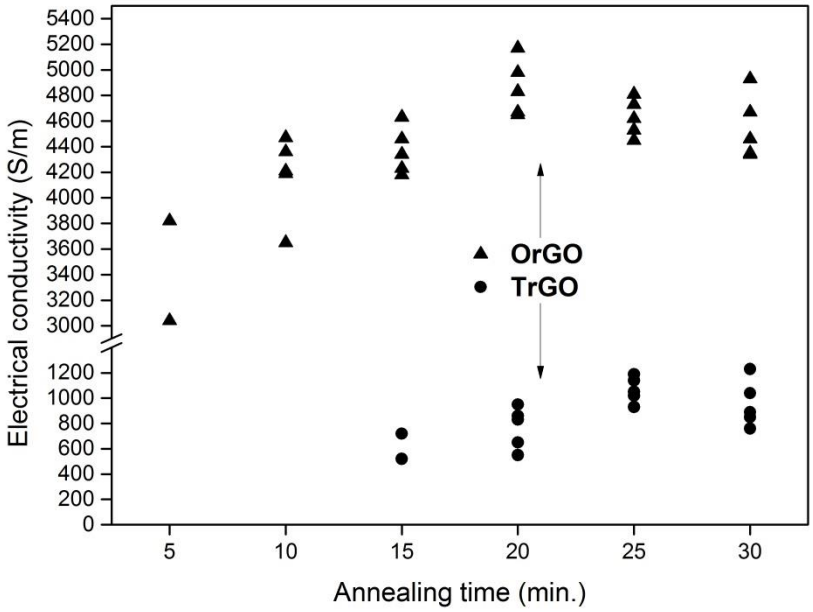

Figure 6.2 The electrical conductivity of TrGO and OrGO for a short-time annealing process.

Figure 6.2 shows the results of the electrical conductivity for TrGO and OrGO samples. The electrical conductivities of OrGO samples were in the range of 3040~5170 S m^{-1} and are apparently higher than that of TrGO papers. During thermal annealing process to fabricate TrGO samples, electrical conductivity was not detected until 15 minutes had elapsed, indicating that the heat treatment could not reduce GO paper to obtain electrical conductive TrGO paper in a very short time. On the other hand, the conversion of OrGO from insulating to conducting are carried out within the first 5 minutes, although only 2 out of 5 samples could be successfully measured. However, the electrical conductivity of one sample was measured as high as 3820 S m^{-1}. Moreover, the average values of electrical conductivity of OrGO increase dramatically to 4830 S m^{-1} in the next 15 minutes. Surprisingly, the highest value of electrical conductivity detected was at 5170 S m^{-1}, which is close to that of TrGO

papers prepared by traditional thermal annealing. Compared with OrGO papers, the electrical conductivity of TrGO papers are gradually improved from 550 to 1230 S m^{-1} in last 15 minutes of thermal annealing. However, the electrical conductivity of TrGO paper is still lower than that of OrGO samples, although the electronic properties of OrGO show a small fluctuation in the last 10 minutes. Consequently, the higher electrical conductivity of OrGO can be attributed to the oxygen gas flow which is introduced during thermal annealing to efficiently reduce GO paper leading to the recovery of the electronic property. In another words, the growth of Al_2O_3 NPs exclusively at the edges of defective regions in the OrGO plane has increased the sp^2/sp^3 ratio to obtain a better electrical conductivity, which is proved by the characterizations in Chapter 6.

Due to numerous oxygen functional groups attached onto the GO plane as well as the structural defects, the electrical conductivity of GO paper is severely decreased to insulating, the oxygen functional groups attached to the plane mainly influencing the electrical conductivity. Hence, the reduction of GO can be performed by removing the oxygen functionalities and healing the structural defects of the basal plane. Kim *et al.* calculated the binding energy between graphene planes and attached oxygen functional groups by density functional theory [313]. They found that hydroxyl groups have a lower binding energy at 15.4 kcal/mol and epoxy groups have a higher binding energy at 62 kcal/mol. Gao *et al.* further reported that hydroxyl groups attached to the interior basal plane have a lower binding energy than hydroxyl groups

located at the edge [314]. Based on their calculations, the hydroxyl groups attached to the edges can be fully dissociated from the GO plane above 650 ℃. However, the characterizations of OrGO demonstrate that the further deoxygenation of GO can be successfully approached through chemical reaction between $Al(OH)_3$ molecules and oxygen functional groups located at the edges, resulting in a higher electrical conductivity of OrGO. As a result, the aggregation of Al_2O_3 NPs on the OrGO plane by oxygen annealing has dramatically improved the electronic properties of rGO material without extra thermal energy consumption.

Experimental work on thermal reduction reveal that the oxygen functional groups can be eliminated at a lower temperature than the calculated temperature used in a long-term annealing process. Jeong *et al.* reported a low temperature thermal annealing at 200 ℃ can remove most oxygen functionalities from the GO plane under low-pressure argon conditions.(550 mTorr) [128]. FTIR results show that epoxy and carboxyl groups apparently decrease while hydroxyl groups completely disappear after thermal annealing for 6 h. Furthermore, the remaining epoxy and carboxyl groups can be dramatically eliminated by low temperature thermal annealing up to 10 h with a C/O ratio of around 10. Therefore, long-duration thermal annealing of GO paper can increase its electrical conductivity by removal of most of the oxygen functional groups. However, the electrical conductivity of short-duration annealed OrGO (Figure 6.2) is close to that of TrGO (Figure 6.1) produced by traditional

thermal reduction, indicating that the formation of Al_2O_3 NPs by short time oxygen annealing approaches a reduction level similar to thermal annealing.

The electrical conductivity of short-duration annealed TrGO and OrGO confirm that oxygen functional groups attached on the GO plane can be removed at 400 ℃ without vacuum in 30 minutes. Although many of the functional groups are thermodynamically stable, the aggregation of Al_2O_3 NPs has the capability to facilitate the dissociation of these functionalities from the GO plane by reacting with functional groups at the edges under an oxygen condition. The removal of oxygen functionalities is more likely to occur in the first 5 minutes while no electrical conductivity can be detected for TrGO samples. Therefore, the reduction pathway for oxygen annealing includes two categories: a. heat treatment in traditional thermal reduction and chemical reaction between $Al(OH)_3$ and functional groups to remove more functionalities resulting in the increase of sp^2/sp^3 ratio. Oxygen annealing has opened a simple and efficient way to improve the reduction level of GO material based on traditional thermal annealing without introducing extra MO precursors to prepare MO/rGO composites.

6.2.2 Wettability of OrGO

GO, TrGO and OrGO were subjected to wettability measurements by testing their static contact angle with water. According to the analysis of their structures, the hydrophilic GO sheets can be converted to hydrophobic rGO sheets by elimination of oxygen functional groups with thermal reduction. Figure 6.3 shows that the contact

angle of GO paper is 43.8 °, indicating a hydrophilic property of GO paper produced by Hummer's Method.

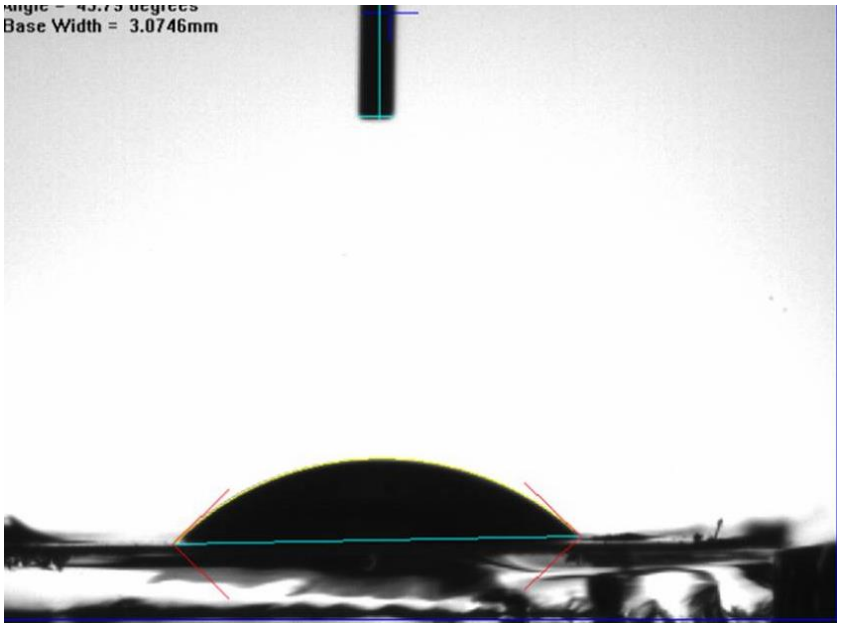

Figure 6.3 Water contact-angle measurements on GO

TrGO paper prepared from thermally reduced GO paper had a contact angle of 88.3 °. Also indicating its hydrophobic properties. (Figure 6.4).

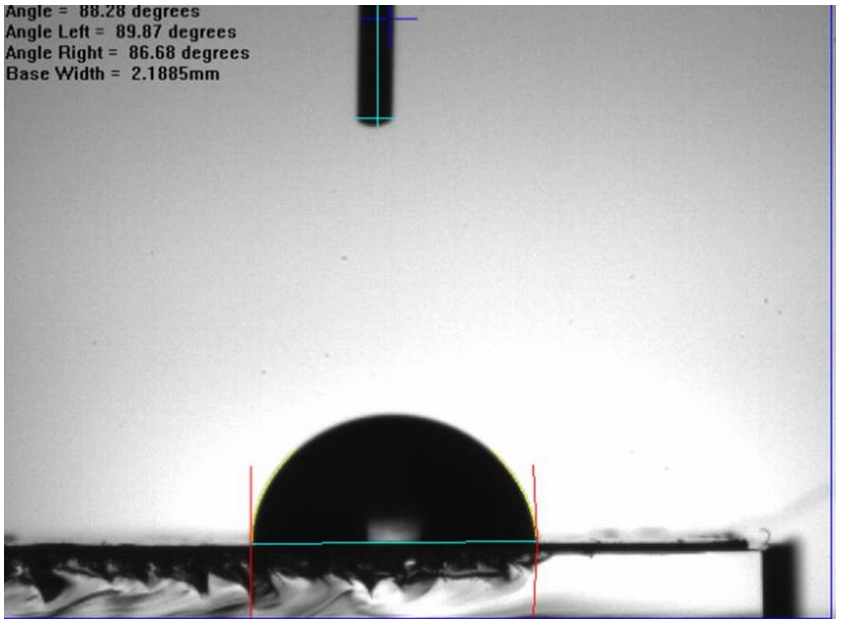

Figure 6.4 Water contact-angle measurements on TrGO

OrGO paper has a different surface wettability from GO and TrGO. The image shown in Figure 6.5, shows a contact angle of around 71.5 °, much less than 90 °, indicating good hydrophilic properties.

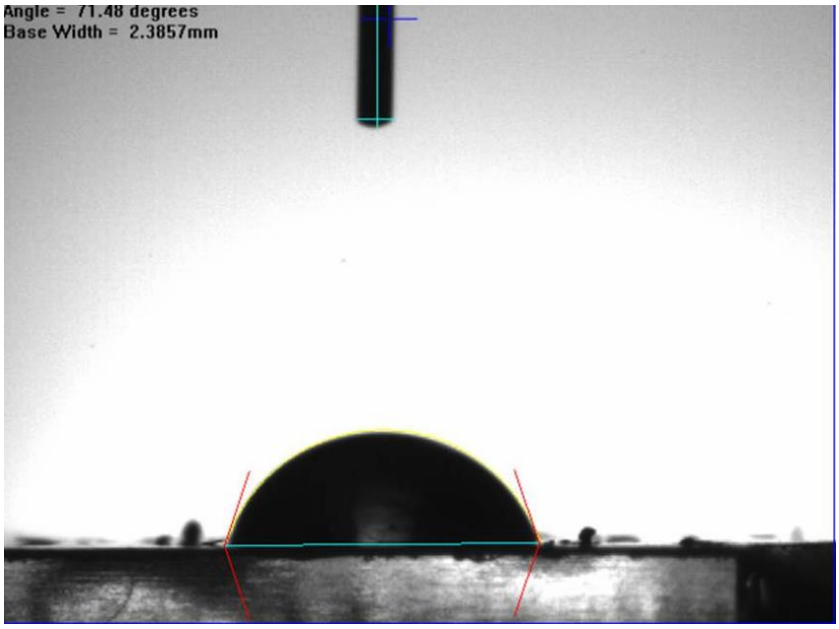

Figure 6.5 Water contact-angle measurements on OrGO

It is interesting to note that the contact angle of OrGO paper is smaller than that of TrGO paper while its electrical conductivity is higher than TrGO. According to structural analysis, the polar oxygen functional groups attached onto the GO plane change the surface wettability from hydrophobic to hydrophilic and decrease the electrical conductivity from conductive to insulating. The elimination of these polar groups by thermal reduction can recover the electronic properties and restore the surface wettability from hydrophilic to hydrophobic. However, the hydrophilic properties as well as the good electrical conductivity provides the material with a better environmental compatibility for the fabrication of electrodes. Therefore,

hydrophilic and electrically conductive OrGO paper fabricated by oxygen annealing may provide a suitable medium for wide application in electronic devices.

It is well known that Al_2O_3 is hydrophilic by nature due to its numerous hydroxyl (OH−) groups [315]. During oxygen annealing, GO is coated with as-formed Al_2O_3 NPs by electrostatic attraction. The heterocoagulation of GO sheets and Al_2O_3 NPs improve the hydrophilic property of the composites[316]. Although the elimination of oxygen functional groups by heat treatment and aggregation of Al_2O_3 NPs on the GO plane weaken the hydrophilic property, the Al_2O_3/rGO composites still exhibit the hydrophilic property with a contact angle of around 71.5 °. Tadanaga *et al.* prepared a superhydrophilic Al_2O_3 film based composite by thermal annealing at 500 ℃ [317]. The water contact angle of the films was smaller than 5 °, indicating the natural hydrophilic property of Al_2O_3 cannot be converted to hydrophobic by heat treatment. Bang *et al.* reported a similar wettability conversion process on poly-4-vinylphenol (PVP) and PVP/Al_2O_3 dielectrics [315]. PVP has a strong hydrophilic property due to its structure consisting of many hydroxyl groups. However, these functional groups can be removed by a condensation process to enlarge the water contact angle of the PVP film to 70 ° while the PVP/Al_2O_3 composite has a water contact angle at 29 °.

6.3 Summary

OrGO has a higher electrical conductivity at 7250 S m^{-1} with a narrower range of the electrical conductivity mostly between 6500 and 7250 S m^{-1}, which can be attributed to a more uniform structure and a better reduction level caused by oxygen annealing.

The formation of Al_2O_3 NPs on the rGO plane can form a well-ordered stacked structure of OrGO paper due to the NPs enlarging the intersheet space which, in turn, facilitates the emission of evolved gas molecules during heat treatment. Short-duration annealing was investigated to elucidate the reduction mechanism. Similar to the electrical conductivity results of TrGO and OrGO, short-duration annealed OrGO still has a higher electrical conductivity at 5170 S m^{-1}, which is close to that of TrGO papers prepared by traditional thermal annealing. The analysis of the annealing mechanism indicates that the increase in the $sp2/sp^3$ carbon ratio caused by the formation of Al_2O_3 NPs at the edges of defective regions in OrGO plane creates its excellent electrical conductivity. In summary, oxygen annealing has two functions: heat treatment for tradition thermal reduction and chemical reaction between $Al(OH)_3$ and functional groups to remove more functionalities resulting in the increase of sp^2/sp^3 ratio.

The wettability measurements revealed that thermal annealing and oxygen annealing methods can be used to fabricate rGO with a tunable wettability, which gives rGO based materials great potential in practical applications. The contact angle of GO paper was measured at 43.8 °, indicating a hydrophilic property. After thermal reduction, the resultant TrGO paper has a hydrophobic property with a contact angle of 88.3 °due to the elimination of oxygen functional groups during the heat treatment. However, OrGO paper has a different surface wettability from TrGO due to its unique Al_2O_3 NP/rGO structure. The contact angle of OrGO sheets is measured around 71.5 °, much less than

90 °, indicating a good hydrophilic property. The analysis further reveals that hydrophilic Al_2O_3 NP decorated on rGO planes improve the hydrophilic property of rGO paper while its electronic property changes from insulating to conducting.

Chapter 7 Application of OrGO paper for LIBs

7.1 Introduction

LIBs have been in high demand for mobile electronic devices and pure or hybrid electric vehicles for many years [318-320]. Anode and cathode materials have a great influence on the energy density and electrochemical performance of LIBs due to their chemical and physical properties[113, 321, 322].Consequently, a lot of effort has been made over the years to improve the properties of electrode materials [316-320, 323]. As a carbonaceous allotrope, rGO sheets are superior for energy storage applications due to their chemical activity, high surface area, broad electrochemical window and extreme electrical conductivity [324-326]. These excellent properties allow rGO sheets a better reversible charge and discharge performance with higher specific capacity than that of current electrode materials such as graphite and $LiCoO_2$.

The carbon atoms in a graphene plane can capture Li^+ ions in a LiC_6 formation to achieve a theoretical energy capacity of 372 mA h g^{-1} for one-side absorption and 744 mA h g^{-1} for both-side absorption[170, 322, 327]. However, graphene nanosheets are easily aggregated to form paper-like materials due to their large surface area and interlayer adhesion by Van der Waals force, which decreases the cross-plane diffusivity of Li^+ ions although the in-plane diffusivity is high [166, 319]. This diffusivity mechanism limits the electrochemical performance especially at high current density [319, 324, 325, 328-330].

MOs such as SnO_2 [331]and Co_3O_4 [171]are used for LIBs as anode materials due to their high theoretical capacity. However, the pulverization and capacity decay of these MO electrodes caused by dramatic changes in specific volume during the cycling processes have affected their electrochemical performance. Therefore, MO/rGO composites with high electrical conductivity and flexibility, such as SnO_2/rGO [31, 176], TiO_2/rGO [209] and Co_3O_4/rGO [332] have been accepted as electrode materials to improve the cycle performance and specific energy capacity. Compared with other carbonaceous materials including graphite [333, 334] and carbon nanotubes [335], rGO sheets are able to effectively restrict the volume change of MOs and maintain the overall high electrical conductivity during the charge and discharge cycles. Unfortunately, due to a weak connection between rGO sheets and MOs, the active NPs still tend to aggregate during the cycling process[31, 85, 176, 204, 336, 337], which decreases their reversible capacity by 20–50 % after 30 cycles[31, 176, 337]. As a result, the preparation of rGO based composites having both high electrical conductivity and good electrochemical performance is still a great challenge today.

Herein we report the lithium storage capability of OrGO based nanocomposite as well as traditionally prepared TrGO. The cycle performance and capability of OrGO indicate that oxygen annealing not only recovers the electrical conductivity of GO but also improves the energy storage capability by fabrication of Al_2O_3 attached hybrid materials. In this research, higher lithium ion storage capacity was proved to be possible by controlling layered structures of TrGO paper.

7.2 Results and discussion

7.2.1 Charge and discharge performance of OrGO electrodes

Figure 7.1 shows the first four charge and discharge profiles of TrGO versus Li^+/Li at a current density of 10 mA g^{-1} between 3.0 and 0.01 V . The first discharge process of TrGO differs from the second in showing a capacity of around 0.6 V, indicating a solid electrolyte interface (SEI) layer formed on the TrGO electrode surface and the reaction of Li^+ ions with the attached oxygen functionalities [334, 335, 338] . The first charge and discharge capacities of TrGO electrode were measured at 952 and 1137 mAh g^{-1}, respectively, which are higher than that of graphite and graphene sheet electrodes [170, 322, 327]. The high reversible capacity of TrGO can be probably attributed to its large surface area and stacked sheets providing numerous active sites including edges and nanopores anchoring Li^+ ions [339]. Furthermore, as a highly disordered carbon material, TrGO electrodes exhibit a broad electrochemical window (0.01–3.0 V) which allows higher Li^+ ion capacity values than that of graphite [340-343] and greater hysteresis between charge and discharge voltage. The specific capacity of the TrGO electrode has been reduced to 867 mAh g^{-1} in the fourth cycle, indicating a stable cyclic performance due to an SEI layer formed in the first cycle.

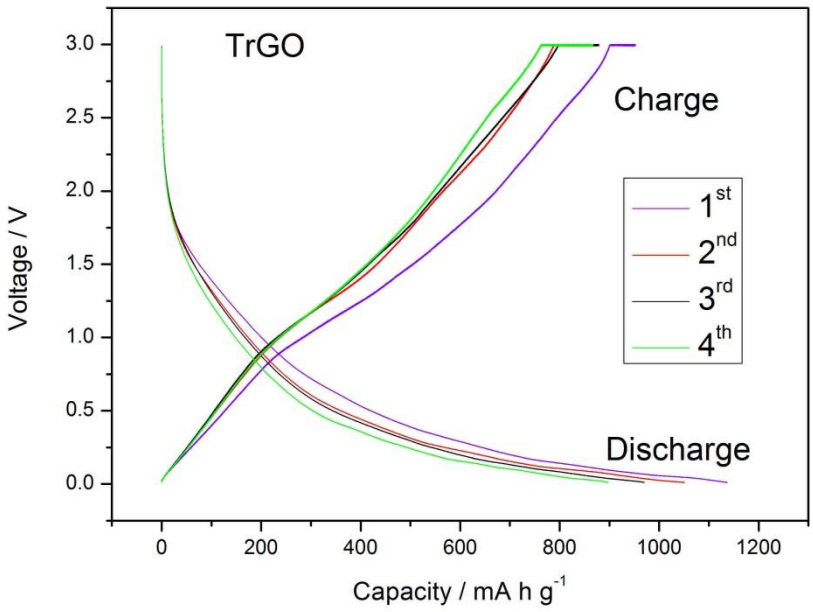

Figure 7.1 First four charge and discharge profiles of TrGO electrode at the current density of 10 mA g^{-1}.

The reversible insertion and extraction of Li^+ ions in the OrGO electrode through the surface was measured to compare the electrochemical performance of rGO paper with and without Al_2O_3 NPs. Figure 7.2 shows the first four charge and discharge profiles of OrGO versus Li^+/Li at a current density of 10 mA g^{-1} between 3.0 and 0.01 V. Unlike the behaviour of graphene-based anode materials or TrGO , the voltage plateau of the first discharge curve around 0.6-0.9 V is not observed [170, 328, 344], indicating that the formation of Al_2O_3 NPs probably suppresses the SEI layer [345]. However, the potential of the four discharge curves decreases dramatically and then forms a plateau around 1.2–1.3 V, which can be attributed to the Li^+ ions reacting with the Al_2O_3 NPs. The first charge and discharge capacities of OrGO electrodes were measured at 1328 and 1364 mAh g^{-1}, respectively, which are higher than that of TrGO. The higher reversible and stable capacity of OrGO can be probably attributed to the

ion conductive Al_2O_3 NPs facilitating Li^+ ion diffusion. Furthermore, the lower degree of hysteresis between charge and discharge voltage of OrGO electrodes represents higher electrical conductivity and a less disordered structure than that of TrGO electrodes [345].

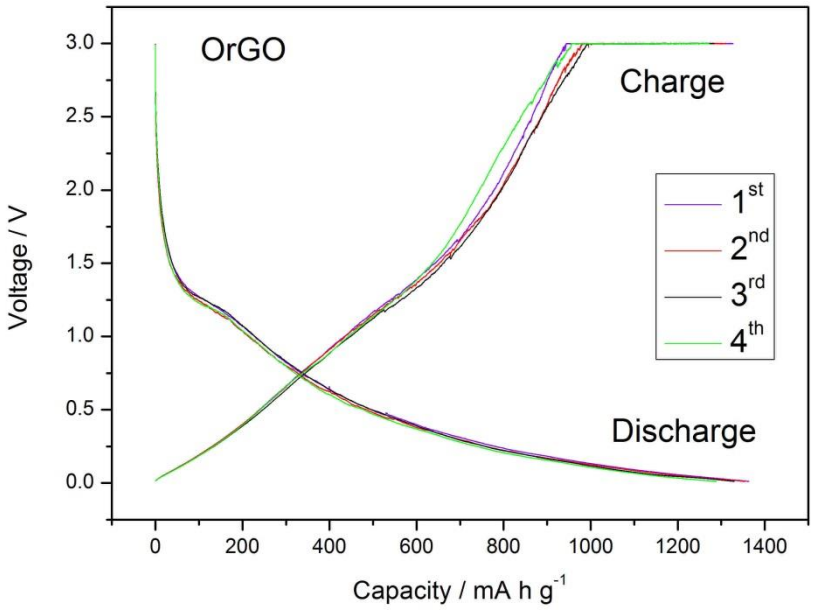

Figure 7.2 First four charge and discharge profiles of OrGO electrode at the current density of 10 mA g^{-1}.

The cyclic voltammograms (CV) of OrGO sheets are shown in Figure 7.3. The results of the CV curves match well with the charge and discharge profiles of OrGO electrodes, exhibiting the reversible insertion and extraction of Li^+ ions. Compared to Li^+/Li, the insertion process begins at a very low potential around 0 V, while the extraction process begins in the range of 0.2–0.3 V. Comparing these four cycles, the reduction current of the first cycle is close to the subsequent cycles without an obvious

irreversible cathodic peak, which can be attributed to the formation of Al_2O_3 NPs probably suppressing the SEI layer and the Li^+ ions reacting with the Al_2O_3 NPs.

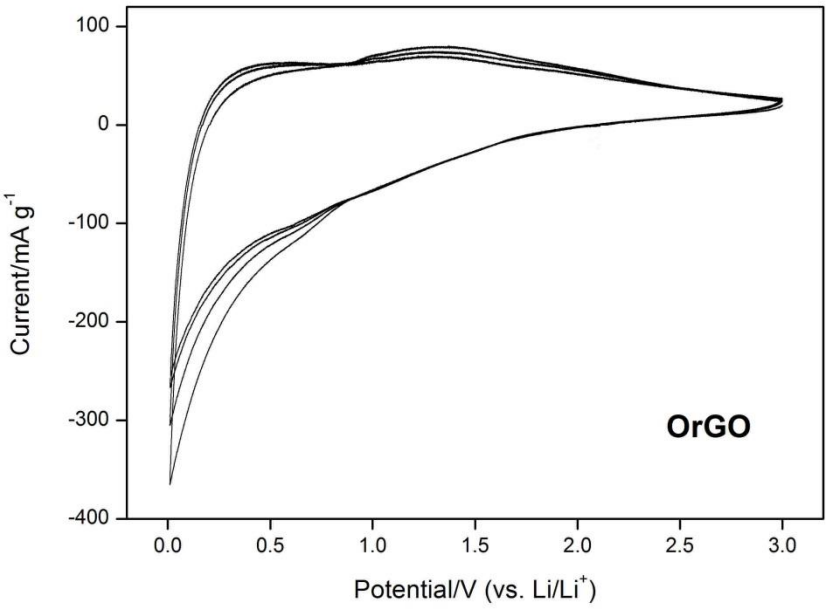

Figure 7.3 Cyclic voltammograms (CV) of OrGO paper.

The rate capability results shown in Figure 7.4 and Figure 7.5 indicate that OrGO paper is an excellent electrode material for LIBs. The reversible specific capacity of OrGO electrode measured at the current density of 10, 20, 40 and 80 mA g^{-1} are 1319, 939, 789 and 762 mAh g^{-1}, respectively, while the reversible specific capacity of TrGO electrodes are 952, 761, 559 and 448 mAh g^{-1}, respectively. Furthermore, the OrGO electrodes still had a higher reversible specific capacity of 909 mAh g^{-1} than that of the TrGO electrodes even for the last 5 cycles with a current density back to 10 mA g^{-1}. The reversible capacity of OrGO electrodes is also dramatically higher than that of formerly reported graphene sheets [337, 346]. As discussed above, the better

rate capability performance of OrGO electrodes can be attributed to their large surface area and less disordered structure as well as the formation of ion conductive Al_2O_3 NPs which probably suppresses the SEI layer. This in turn facilitates Li^+ ion diffusion, shortens the electronic and ionic transport distance and improves the charge and discharge performance at high current density.

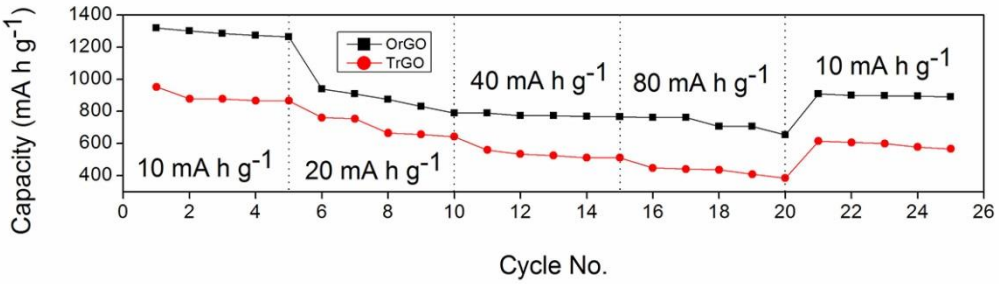

Figure 7.4 Rate capability and cycling performance of OrGO and TrGO electrodes at current densities from 10 to 80 mA g^{-1}.

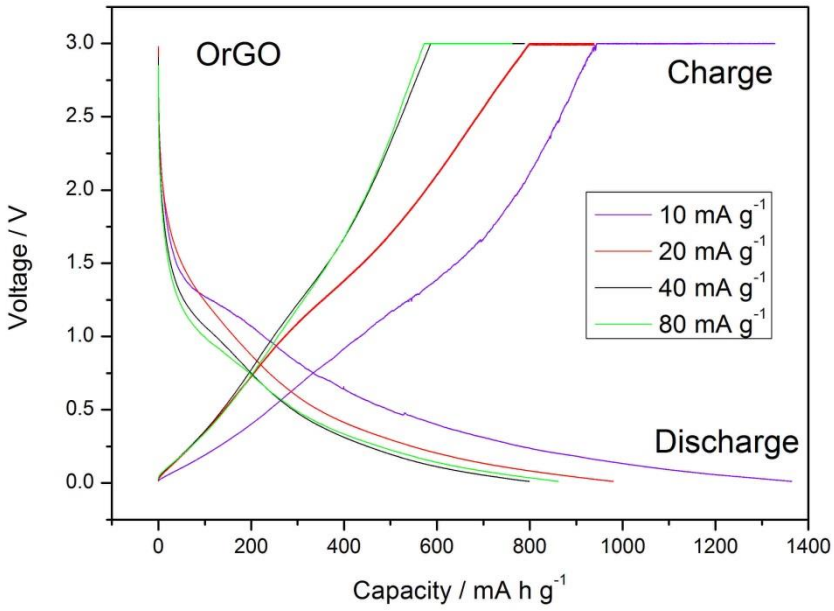

Figure 7.5 Galvanostatic charge and discharge profiles of OrGO at the different current density from 10 to 80 mA g^{-1}.

7.2.2 Cycling performance of OrGO electrode

The cycling performance of OrGO and TrGO electrodes was then investigated. Figure 7.6 shows the cycling performance of these electrodes and their coulombic efficiency (CE) at a current density of 80 mA g^{-1} for 30 cycles. The cycling performance results of OrGO electrodes exhibit a specific capacity of 797 mAh g^{-1} after 30 cycles, which is higher than that of TrGO electrodes as well as the formerly reported graphene sheets [166, 346]. Although the TrGO electrodes also had a stable cycling performance with a specific capacity maintained at 766 mAh g^{-1} after 30 cycles, its CE was slightly lower than that of OrGO electrodes. The average CE of OrGO electrodes for 30 cycles was 99.608%, indicating a superior reversibility of the Li^+ ion insertion/extraction process. The higher CE probably can be attributed to the surface modification by Al_2O_3 NPs and electrolyte.

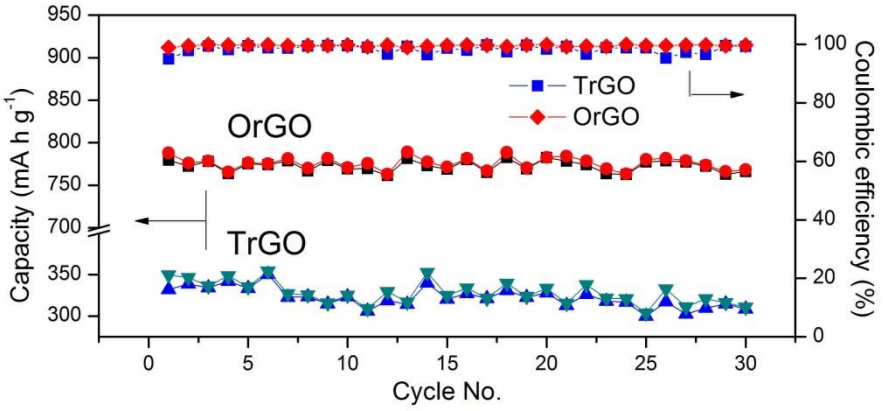

Figure 7.6 Cycling performance and CE of OrGO and TrGO electrodes at a current density of 80 mA g^{-1} for 30 cycles.

The high stability of the charge and discharge cycles can be attributed to the ultrathin nature of OrGO and TrGO sheets. Wu *et al.* reported that double-walled silicon

nanotubes (DWSiNTs) have lower cycling stability owing to the elimination of the constraining effect caused by the thicker tube side walls [347]. Moreover, the ultrathin DWSiNTs as well as being thin and stable SEI also allow an excellent high power rate capability due to the Li^+ ions being rapidly inserted into/extracted from the electrode surface through the thin SEI layer.

7.3 Summary

The electrochemical performance of OrGO and TrGO papers fabricated as electrode materials for LIBs was investigated in this chapter.

(i) Charge and discharge performance.

OrGO electrodes exhibit a high specific charge and discharge capacity at 1328 and 1364 mAh g^{-1}, which are higher values than that of TrGO electrodes at 952 and 1137 mAh g^{-1}, respectively. While an SEI layer was formed on TrGO electrodes at a potential around 0.6 V, the discharge curves for four cycles of OrGO electrodes show a potential plateau around 1.2–1.3 V, which can be attributed to the formation of Al_2O_3 NPs that probably suppress the SEI layer and the Li^+ ions reacting with the Al_2O_3 NPs. Furthermore, the higher electrical conductivity and less disordered structure of OrGO electrodes make the hysteresis voltage between charge and discharge curves lower than that of TrGO electrodes.

(ii) Cyclic voltammograms

The investigation of CV performance for OrGO electrodes vs. Li^+/Li reveal that the insertion of Li^+ ions begins at a very low potential of around 0 V while the

extraction process begins in the range of 0.2–0.3 V. The closed CV curves without an obvious irreversible cathodic peak indicate that the formation of an SEI layer on the electrode surface is suppressed by Al_2O_3 NPs.

(iii) Rate capability

OrGO electrode has an excellent rate capability at a current density of 10, 20, 40, 80 and mA g^{-1}. The reversible capacities of OrGO electrodes (1319, 939, 789 and 762 mAh g^{-1} at 10, 20, 40 and 80 mA g^{-1}, respectively) are dramatically higher than that of TrGO electrodes as well as the formerly reported graphene sheets, This can be attributed to the ion conductive Al_2O_3 NPs facilitating Li^+ ion diffusion.

(iv) Cycling performance

OrGO and TrGO electrodes were then measured for cycling performance and relative CE at a current density of 80 mA g^{-1} for 30 cycles. OrGO electrodes exhibited the high and stable specific capacities of around 800 mA h g^{-1} for 30 cycles. Moreover, the average CE of OrGO electrodes at 99.608% for 30 cycles I was higher than that of TrGO electrodes, indicating a superior reversibility of the Li^+ ion insertion/extraction process. Similar research on DWSiNTs illustrates that the high stability of the charge and discharge cycles is probably related to the ultrathin nature of OrGO and TrGO sheets.

In conclusion, the ion conductive Al_2O_3 NPs formed on OrGO plane improve the charge and discharge performance, rate capability and cycling performance of OrGO electrodes in LIBs.

Chapter 8 Conclusion

This thesis describes an innovative oxygen annealing method for the fabrication of Al_2O_3 NP/rGO composites and investigates the mechanism of Al_2O_3 NPs' distribution and aggregation on the GO plane. The electrical conductivity and wettability of OrGO paper have also been investigated, which is very pertinent to the fabrication of OrGO electrodes in LIBs.

The literature review provides a guide to current research into the properties, synthesis and functionalization of GO and rGO. The research on the structure of GO and rGO reveals that they exhibit a unique two-dimensional structure with attached oxygen functional groups which can be removed to improve electrical conductivity, electrochemical performance, chemical activity and wettability. Investigations into the properties of GO and rGO enable us to understand the structural difference between GO and rGO sheets, which is useful in understanding the formation and removal of oxygen functional groups attached on the GO plane. Furthermore, the recent progress in the functionalization of rGO sheets such as MO NP/rGO composites for energy storage applications is also reviewed, focusing on the chemical oxidation, thermal reduction and MO NPs functionalization. However, there is a long way to go before the fabrication of rGO sheets can meet the requirements of industrial applications. In furtherance of this goal, we present our research work on an innovative OrGO material with excellent electronic properties for energy storage application.

Firstly, the innovative exfoliation process using high speed centrifugation and probe ultrasonication to reduce the number of GO layers has successfully produced monolayer GO sheets, which provides the opportunity to determine the structure and distribution of Al_2O_3 NPs on individual single layers of the OrGO plane.

Secondly, a better understanding has been achieved by imaging GO, TrGO and OrGO samples with a variety of characterization methods such as optical microscopy, SEM, TEM, HRTEM and AFM. The monolayer structure of GO produced by the innovative exfoliation process has been confirmed. The "grey" flakes of the individual TrGO samples show a single-layer structure in SEM images while the darker areas indicate multi-layer features. The SAED pattern of TEM images shows the very obvious 12 diffraction spots with equivalent relative intensities between the inner and outer hexagons indicating the single-layer structure. In HRTEM images, the uniform single dark line at the edges of unfolded monolayers of OrGO further confirms the single-layer structure. Moreover, the height profile of AFM images provides evidence of the single-layer structure of OrGO sheets. The structure and formation of wrinkles in GO, TrGO and OrGO planes has also been analyzed. The wrinkles were introduced due to the thermal expansion coefficient difference between substrate and graphene sheets during the annealing process. Unlike the uniform thickness of wrinkles at the edges of folded bilayer structures, the wrinkles in a monolayer rGO sample vary in width. Additionally, the monolayer, bilayer and overlapped multi-layer structure have been investigated in detail to establish a simple system for distinguishing single-layer

sheets. Moreover, the distribution and structure of Al_2O_3 NPs synthesized in OrGO have been characterized with HRTEM and AFM. The diameter of NPs is less than 10 nm with a typical high interparticle distance of between 60-80 nm, which is confirmed by HRTEM. The NPs are located at the edges of holes produced during the annealing process. Furthermore, from height profiles of AFM images we have determined that the height of NPs is less than 2 nm. Morphology analysis has established a fundamental understanding of the monolayer structure of GO, TrGO and OrGO samples which are the basic units in GO paper. Our innovative method for producing a single-layer GO dispersion allows a better formation process of GO paper.

Thirdly, we have improved the traditional thermal annealing method by introducing oxygen gas flow in the thermal reduction process to fabricate OrGO sheets, enabling the removal of oxygen functional groups and recovery of defective regions. With this method, colloidal suspensions consisting of individual GO sheets can yield Al_2O_3 NPs decorated rGO paper by vacuum filtration through an Anodisc membrane filter. Upon the introduction of Al^{3+} as seeds anchoring on the GO plane by a vacuum filtration through an alumina Anodisc membrane filter, the Al_2O_3 molecules aggregated to form NPs and grew on the edges of holes or vacancies during thermal annealing. XPS spectra confirm the reduction efficiency of TrGO and OrGO as well as the element states of aluminium in GO or rGO planes. The Raman and FTIR results reveal dangling bonds or oxygen functional groups of GO binding to the Al^{3+} promoting aluminium oxide aggregates and growth which leads to further reduction.

Fourthly, as regards electronic properties, OrGO has a higher electrical conductivity at 7250 S m^{-1} with a narrower range of electrical conductivity mostly between 6500 and 7250 S m^{-1}, which can be attributed to a more uniform structure and a better reduction level caused by oxygen annealing. The formation of Al_2O_3 NPs on the rGO plane can form a well-ordered stacked structure of OrGO paper due to the NPs enlarging the intersheet space which facilitates the emission of evolved gas molecules during heat treatment. A short-duration annealing procedure was designed to elucidate the reduction mechanism of oxygen annealing. Similar to previous electrical conductivity results for TrGO and OrGO, short-duration annealed OrGO still had a higher electrical conductivity at 5170 Sm^{-1}, which is close to that of TrGO papers prepared by traditional thermal annealing. Analysis of the annealing mechanism indicated that the increase of the sp^2/sp^3 carbon ratio caused by the formation of Al_2O_3 NPs at the edges of defective regions in the OrGO plane allows its excellent electrical conductivity. Therefore, oxygen annealing has two functions: heat treatment for traditional thermal reduction and chemical reaction between $Al(OH)_3$ and functional groups to remove more functionalities resulting in an increase of the sp^2/sp^3 ratio.

Fifthly, wettability measurements revealed that appropriate thermal and oxygen annealing methods can be used to fabricate rGO with a tunable wettability. This allows rGO based materials great potential in practical applications. The contact angle of GO paper was measured at 43.8 °, indicating a hydrophilic property. After thermal reduction, the resultant TrGO paper had a hydrophobic property with a contact angle

of 88.3 ° due to the elimination of oxygen functional groups during the heat treatment. However, OrGO paper had a different surface wettability from TrGO due to its unique Al_2O_3 NP/rGO structure. The contact angle of OrGO sheets was measured at around 71.5 °, much less than 90 °, indicating a good hydrophilic property. Analysis of the production mechanism revealed that hydrophilic Al_2O_3 NP decorated on rGO plane improve the hydrophilic property of rGO paper while its electronic properties change from insulating to conducting.

Lastly, the electrochemical performance of OrGO and TrGO papers fabricated as electrode materials for LIBs was investigated. In the charge and discharge phases, OrGO electrodes exhibited a high specific charge and discharge capacity at 1328 and 1364 mAh g^{-1}, which were higher than that of TrGO electrodes at 952 and 1137 mAh g^{-1}, respectively. Whereas for TrGO electrodes an SEI layer formed at a potential around 0.6 V, the discharge curves for four cycles using OrGO electrodes show a potential plateau around 1.2–1.3 V, which can be attributed to the formation of Al_2O_3 NPs which probably suppressed the SEI layer and the Li^+ ions reacting with the Al_2O_3 NPs. Furthermore, the higher electrical conductivity and less disordered structure of OrGO electrodes make its hysteresis voltage between charge and discharge curves lower than that of TrGO electrodes. Also, according to cyclic voltammograms, investigation of CV performance of OrGO electrodes revealed that the insertion of Li^+ ions begins at a very low potential around 0 V vs. Li^+/Li while the extraction process begins in the range of 0.2–0.3 V. The closed CV curves are without an obvious

irreversible cathodic peak indicating that the formation of the SEI layer on the electrode surface is suppressed by Al_2O_3 NPs. Regarding rate capability, OrGO electrodes had an excellent rate capability at a current density of 10, 20, 40, 80 and mA g^{-1}. The reversible capacities of OrGO electrodes (1319, 939, 789 and 762 mAh g^{-1} at 10, 20, 40 and 80 mA g^{-1}, respectively) were dramatically higher than that of TrGO electrodes as well as formerly reported graphene sheets. This can be attributed to the ion conductive Al_2O_3 NPs facilitating Li^+ ion diffusion. OrGO and TrGO electrodes were then measured for cycling performance and relative CE at a current density of 80 mA g^{-1} for 30 cycles. OrGO electrode exhibited high and stable specific capacities at around 800 mAh g^{-1} for 30 cycles. Moreover, the average CE of OrGO electrodes at 99.608% for 30 cycles was higher than that of TrGO electrodes, indicating a superior reversibility of the Li^+ ion insertion/extraction process. The high stability of the charge and discharge cycles is probably related to the ultrathin nature of OrGO and TrGO sheets. As a result, the ion conductive Al_2O_3 NPs formed on OrGO planes improves the charge and discharge performance, rate capability and cycling performance of OrGO electrodes in LIBs.

Chapter 9 Future work

The reduction of GO for mass production and application has been discussed in the thesis. However, complete reduction is still difficult to achieve due to the limited understanding of the chemistry and structure of GO and rGO. Therefore, future research on the preparation of rGO should focus on the further investigation of the reduction mechanism and controllable functionalization of rGO for specific applications. A well-designed reduction method is needed to remove most of the oxygen functional groups and recover the defective regions. For the functionalization of rGO, other specific filter membranes can be used for rGO based nanocomposites.

The excellent electrochemical performance of OrGO has been frequently noted but, more work in the future is required for a better understanding of OrGO electrodes for full application in LIBs. Therefore, the next step is to find a cathode material to fabricate full LIBs. Energy storage is in high demand and amongst the possible options, Li-ion batteries have been the dominating energy storage device for light-weight applications in terms of energy density but lacks power density and cycle life. The future project is to investigate and develop improved materials to address the above limitations of Li-ion batteries. $LiFePO_4$ is a promising positive electrode owing to its safe and low cost raw materials and high energy density. Various annealing temperatures have been examined with $LiFePO_4$ prepared using a classical sol-gel wet chemical method. The development of a safer electrolyte using a polymer based on

polyvinylidene fluoride co-polymer is also being investigated as a replacement for current liquid electrolyte.

Appendix

Table A 1 Electrical conductivity (S/m) of TrGO and OrGO produced by a short time annealing without vacuum

	5min	10min	15min	20min	25min	30min
TrGO (S m^{-1})	0	0	0	860	1140	1040
	0	0	0	950	1020	1230
	0	0	0	550	1050	850
	0	0	520	650	930	760
	0	0	720	830	1190	890
OrGO (S m^{-1})	0	4190	4340	4830	4450	4670
	0	4470	4230	4650	4730	4340
	0	3650	4460	5170	4810	4460
	3820	4360	4630	4670	4530	4350
	3040	4210	4180	4980	4620	4930

Bandgap of TrGO and OrGO

The bandgap of TrGO and OrGO was determined by calculating the UV-Vis absorption spectra (Figure A 1and Figure A 2) using the equation

$$\alpha h\upsilon = A\left(h\upsilon - E_g\right)^n$$

where α, h, υ, A, and E_g are the absorption coefficient, Planck's constant, light frequency, proportionality coefficient, and band gap energy, respectively , as well as n is equal to 2 for an allowed indirect transition or 1/2 for an allowed direct transition.

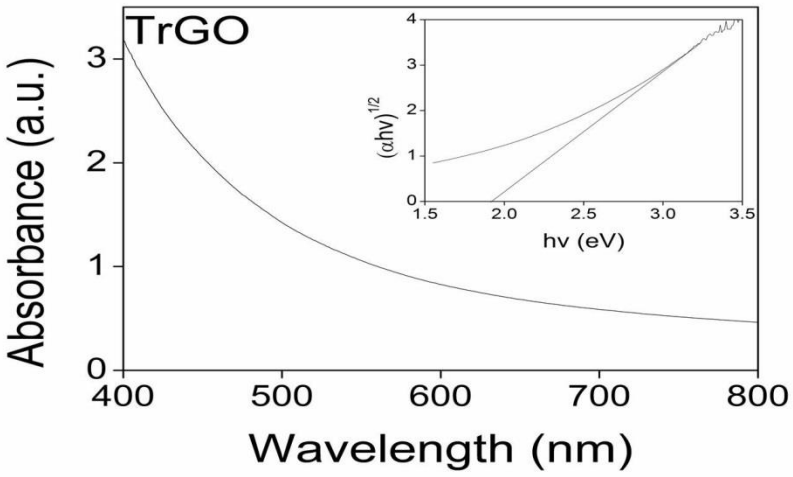

Figure A 1 UV–Vis absorption spectra of TrGO. Inset, the plots of $(\alpha h\nu)^{1/2}$ versus hν show the indirect band gap of 1.91 eV (TrGO).

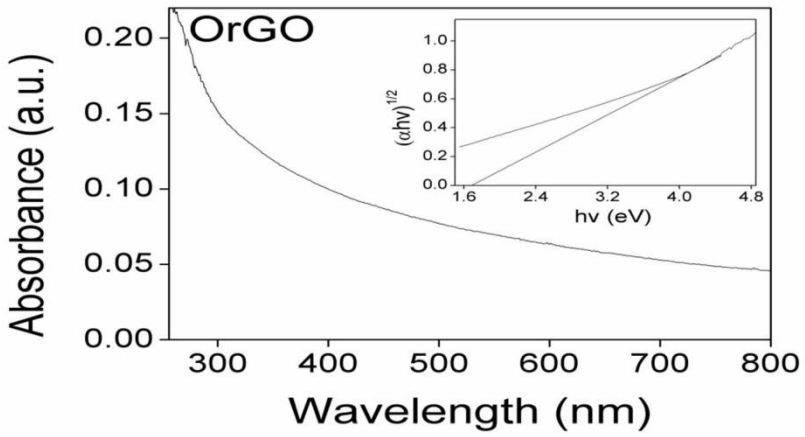

Figure A 2 UV–Vis absorption spectra of OrGO (b). Inset, the plots of $(\alpha h\nu)^{1/2}$ versus hν show the indirect band gap of 1.68 eV (OrGO),respectively.

UV–Vis results indicate that the TrGO has a bigger indirect band gap of 1.91 eV (Figure A 1) which is 0.23 eV higher than that of OrGO (1.68 eV, Figure A 2). These results suggest that the heat treatment can open the bandgap of GO. Moreover, the growth of Al_2O_3 NPs on rGO plane by oxygen annealing leads to a reduced bandgap of OrGO, which can be attributed to the increased sp^2 carbon networks in OrGO plane[280]. Joung et al. shows a bandgap variation of rGO, which is prepared by ammonia and

hydrazine hydrate reduction, from 1.43 eV to 0.21 eV with sp^2 fraction increased from 55 to 80%.

PL of TrGO and OrGO

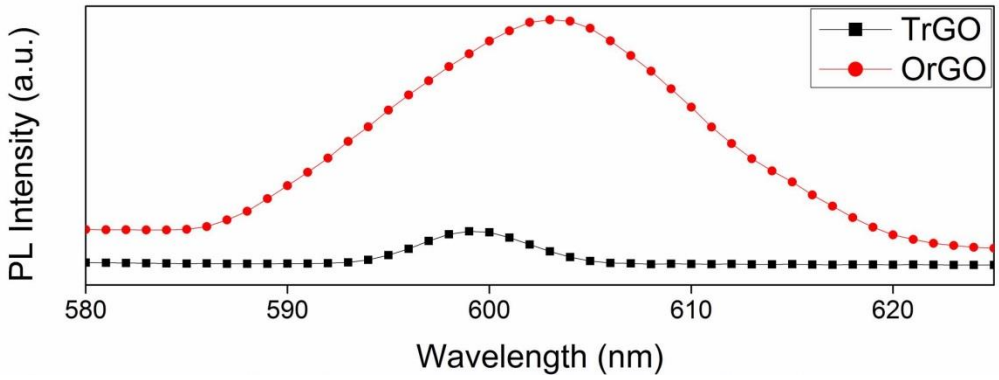

Figure A 3 Photoluminescence emission spectrum of the luminescent rGO (excitation at 400 nm) exhibiting hypersensitive red emission at 599 nm (TrGO) and 603 nm (OrGO).

Another interesting finding is the PL behavior of OrGO. Figure A 3 shows that OrGO sample excited with 400 nm xenon light has a broad and strong PL peak centered at 603 nm and TrGO sample exhibits a weak emission at 599 nm. This slight redshift of the PL peak position probably due to the variations of oxidation density [348]. The PL intensity of OrGO is dramatically higher than that of TrGO, indicating the oxygen annealing facilitating the emission process comparing to the traditional thermal annealing [78, 349].

XRD spectra of TrGO and OrGO

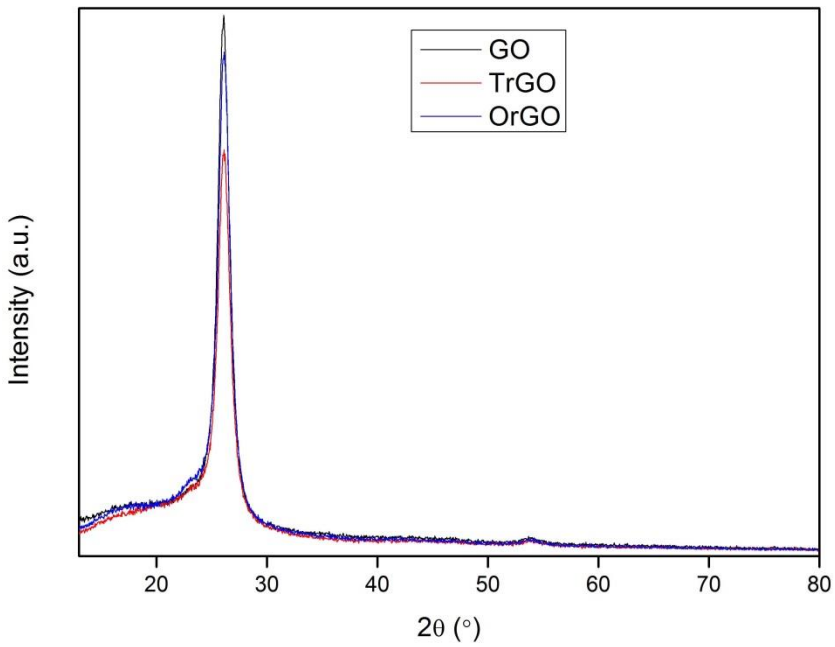

Figure A 4 XRD pattern of GO, TrGO and OrGO papers. The characterization was carried out in a Siemens D500 powder X-ray diffractometer at 40 k eV and 25 mA with Cu Kα line as the excitation source radiation (λ=1.5406 Å).

The distinct peaks at 13.0 °in the XRD spectra of the GO papers corresponding to the layer-to-layer distance (d-spacing) of approximately 3.4 Å that is equal to the interlayer separation in graphite. The numbers of perpendicularly stacked GO and reduced GO sheets in the paper material were calculated by using the classical Debye−Scherrer equation

$$\tau = \frac{K\lambda}{\beta \cos\theta}$$

$$n = \frac{\tau}{d}$$

where K is the shape factor, λ is the x-ray wavelength, β is the full width at half maximum (FWHM), θ is the Bragg angle, τ is the thickness, and *d* is the interlayer

spacing. The thickness was found to be 6.8 Å which corresponds to 2 stacked graphene oxide sheets.

References

1. Novoselov, K.S., et al., *Electric field effect in atomically thin carbon films.* Science, 2004. **306**(5296): p. 666-669.
2. Lee, C., et al., *Measurement of the elastic properties and intrinsic strength of monolayer graphene.* Science, 2008. **321**(5887): p. 385-388.
3. Chen, J.H., et al., *Intrinsic and extrinsic performance limits of graphene devices on SiO2.* Nature Nanotechnology, 2008. **3**(4): p. 206-209.
4. Kuzmenko, A.B., et al., *Universal optical conductance of graphite.* Physical Review Letters, 2008. **100**(11): p. -.
5. Zheng, Y., et al., *Gate-controlled nonvolatile graphene-ferroelectric memory.* Applied Physics Letters, 2009. **94**(16).
6. Ghosh, S., et al., *Dimensional crossover of thermal transport in few-layer graphene.* Nature Materials, 2010. **9**: p. 4.
7. *Graphene: The Next Wonder Material?* ; Available from: http://www.acs.org/content/acs/en/education/resources/highschool/chemmatters/past-issues/archive-2012-2013/graphene.html.
8. Sutter, P., *EPITAXIAL GRAPHENE How silicon leaves the scene.* Nature Materials, 2009. **8**(3): p. 171-172.
9. Li, X.S., et al., *Large-Area Synthesis of High-Quality and Uniform Graphene Films on Copper Foils.* Science, 2009. **324**(5932): p. 1312-1314.
10. Li, D., et al., *Processable aqueous dispersions of graphene nanosheets.* Nature Nanotechnology, 2008. **3**(2): p. 101-105.
11. Stankovich, S., et al., *Synthesis of graphene-based nanosheets via chemical reduction of exfoliated graphite oxide.* Carbon, 2007. **45**(7): p. 1558-1565.
12. Eda, G. and M. Chhowalla, *Chemically Derived Graphene Oxide: Towards Large-Area Thin-Film Electronics and Optoelectronics.* Advanced Materials, 2010. **22**(22): p. 2392-2415.
13. Schniepp, H.C., et al., *Functionalized single graphene sheets derived from splitting graphite oxide.* Journal of Physical Chemistry B, 2006. **110**(17): p. 8535-8539.
14. Stankovich, S., et al., *Stable aqueous dispersions of graphitic nanoplatelets via the reduction of exfoliated graphite oxide in the presence of poly(sodium 4-styrenesulfonate).* Journal of Materials Chemistry, 2006. **16**(2): p. 155-158.
15. Yang, D., et al., *Chemical analysis of graphene oxide films after heat and chemical treatments by X-ray photoelectron and Micro-Raman spectroscopy.* Carbon, 2009. **47**(1): p. 145-152.
16. Jung, I., et al., *Effect of Water Vapor on Electrical Properties of Individual Reduced Graphene Oxide Sheets.* Journal of Physical Chemistry C, 2008. **112**(51): p. 20264-20268.
17. Periasamy, M. and P. Thirumalaikumar, *Methods of enhancement of reactivity and selectivity of sodium borohydride for applications in organic synthesis.* Journal of Organometallic Chemistry, 2000. **609**(1-2): p. 137-151.
18. Wu, Z.S., et al., *Synthesis of high-quality graphene with a pre-determined number of layers.* Carbon, 2009. **47**(2): p. 493-499.

19. McAllister, M.J., et al., *Single sheet functionalized graphene by oxidation and thermal expansion of graphite.* Chemistry of Materials, 2007. **19**(18): p. 4396-4404.
20. Li, X.L., et al., *Highly conducting graphene sheets and Langmuir-Blodgett films.* Nature Nanotechnology, 2008. **3**(9): p. 538-542.
21. Lu, G.H., L.E. Ocola, and J.H. Chen, *Gas detection using low-temperature reduced graphene oxide sheets.* Applied Physics Letters, 2009. **94**(8).
22. Zhou, X.Z., et al., *In Situ Synthesis of Metal Nanoparticles on Single-Layer Graphene Oxide and Reduced Graphene Oxide Surfaces.* Journal of Physical Chemistry C, 2009. **113**(25): p. 10842-10846.
23. Li, Y.J., et al., *Catalytic performance of Pt nanoparticles on reduced graphene oxide for methanol electro-oxidation.* Carbon, 2010. **48**(4): p. 1124-1130.
24. Williams, G., B. Seger, and P.V. Kamat, *TiO2-graphene nanocomposites. UV-assisted photocatalytic reduction of graphene oxide.* Acs Nano, 2008. **2**(7): p. 1487-1491.
25. Zhu, J.X., et al., *Facile synthesis of metal oxide/reduced graphene oxide hybrids with high lithium storage capacity and stable cyclability.* Nanoscale, 2011. **3**(3): p. 1084-1089.
26. Joung, D., et al., *Anchoring Ceria Nanoparticles on Reduced Graphene Oxide and Their Electronic Transport Properties.* Journal of Physical Chemistry C, 2011. **115**(50): p. 24494-24500.
27. Ghosh, S., et al., *One pot synthesis of RGO/PbS nanocomposite and its near infrared photoresponse study.* Applied Physics a-Materials Science & Processing, 2012. **107**(4): p. 995-1001.
28. Balazs, A.C., T. Emrick, and T.P. Russell, *Nanoparticle polymer composites: Where two small worlds meet.* Science, 2006. **314**(5802): p. 1107-1110.
29. Bashyam, R. and P. Zelenay, *A class of non-precious metal composite catalysts for fuel cells.* Nature, 2006. **443**(7107): p. 63-66.
30. Capadona, J.R., et al., *A versatile approach for the processing of polymer nanocomposites with self-assembled nanofibre templates.* Nature Nanotechnology, 2007. **2**(12): p. 765-769.
31. Paek, S.M., E. Yoo, and I. Honma, *Enhanced Cyclic Performance and Lithium Storage Capacity of SnO2/Graphene Nanoporous Electrodes with Three-Dimensionally Delaminated Flexible Structure.* Nano letters, 2009. **9**(1): p. 72-75.
32. Wu, Z.S., et al., *Graphene Anchored with Co(3)O(4) Nanoparticles as Anode of Lithium Ion Batteries with Enhanced Reversible Capacity and Cyclic Performance.* ACS Nano, 2010. **4**(6): p. 3187-3194.
33. Zhu, X.J., et al., *Nanostructured Reduced Graphene Oxide/Fe(2)O(3) Composite As a High-Performance Anode Material for Lithium Ion Batteries.* ACS Nano, 2011. **5**(4): p. 3333-3338.
34. Zhou, G.M., et al., *Graphene-Wrapped Fe(3)O(4) Anode Material with Improved Reversible Capacity and Cyclic Stability for Lithium Ion Batteries.* Chemistry of Materials, 2010. **22**(18): p. 5306-5313.
35. Joung, D., et al., *High yield fabrication of chemically reduced graphene oxide field effect transistors by dielectrophoresis.* Nanotechnology, 2010. **21**(16).

36. Ghosh, S., et al., *Position dependent photodetector from large area reduced graphene oxide thin films.* Applied Physics Letters, 2010. **96**(16).
37. Kou, R., et al., *Enhanced activity and stability of Pt catalysts on functionalized graphene sheets for electrocatalytic oxygen reduction.* Electrochemistry Communications, 2009. **11**(5): p. 954-957.
38. Williams, G. and P.V. Kamat, *Graphene-Semiconductor Nanocomposites: Excited-State Interactions between ZnO Nanoparticles and Graphene Oxide.* Langmuir, 2009. **25**(24): p. 13869-13873.
39. Gomez-Navarro, C., et al., *Atomic Structure of Reduced Graphene Oxide.* Nano Letters, 2010. **10**(4): p. 1144-1148.
40. Mkhoyan, K.A., et al., *Atomic and Electronic Structure of Graphene-Oxide.* Nano Letters, 2009. **9**(3): p. 1058-1063.
41. Dreyer, D.R., et al., *The chemistry of graphene oxide.* Chemical Society Reviews, 2010. **39**(1): p. 228-240.
42. Park, S. and R.S. Ruoff, *Chemical methods for the production of graphenes.* Nature Nanotechnology, 2009. **4**(4): p. 217-224.
43. Mattevi, C., et al., *Evolution of Electrical, Chemical, and Structural Properties of Transparent and Conducting Chemically Derived Graphene Thin Films.* Advanced Functional Materials, 2009. **19**(16): p. 2577-2583.
44. Erickson, K., et al., *Determination of the Local Chemical Structure of Graphene Oxide and Reduced Graphene Oxide.* Advanced Materials, 2010. **22**(40): p. 4467-4472.
45. Kudin, K.N., et al., *Raman spectra of graphite oxide and functionalized graphene sheets.* Nano Letters, 2008. **8**(1): p. 36-41.
46. Hass, J., W.A. de Heer, and E.H. Conrad, *The growth and morphology of epitaxial multilayer graphene.* Journal of Physics-Condensed Matter, 2008. **20**(32).
47. Wang, X., L.J. Zhi, and K. Mullen, *Transparent, conductive graphene electrodes for dye-sensitized solar cells.* Nano letters, 2008. **8**(1): p. 323-327.
48. Seger, B. and P.V. Kamat, *Electrocatalytically Active Graphene-Platinum Nanocomposites. Role of 2-D Carbon Support in PEM Fuel Cells.* Journal of Physical Chemistry C, 2009. **113**(19): p. 7990-7995.
49. Lu, T., et al., *Electrochemical behaviors of graphene-ZnO and graphene-SnO2 composite films for supercapacitors.* Electrochimica Acta, 2010. **55**(13): p. 4170-4173.
50. Yu, A.P., et al., *Ultrathin, transparent, and flexible graphene films for supercapacitor application.* Applied Physics Letters, 2010. **96**(25).
51. Guo, P., H.H. Song, and X.H. Chen, *Electrochemical performance of graphene nanosheets as anode material for lithium-ion batteries.* Electrochemistry Communications, 2009. **11**(6): p. 1320-1324.
52. Kim, H., et al., *SnO2/Graphene Composite with High Lithium Storage Capability for Lithium Rechargeable Batteries.* Nano Research, 2010. **3**(11): p. 813-821.
53. Kim, H., et al., *Highly reversible Co3O4/graphene hybrid anode for lithium rechargeable batteries.* Carbon, 2011. **49**(1): p. 326-332.
54. Lian, P.C., et al., *Large reversible capacity of high quality graphene sheets as an anode material for lithium-ion batteries.* Electrochimica Acta, 2010. **55**(12): p. 3909-3914.

55. Magasinski, A., et al., *High-performance lithium-ion anodes using a hierarchical bottom-up approach.* Nature Materials, 2010. **9**(4): p. 353-358.
56. Pan, D.Y., et al., *Li Storage Properties of Disordered Graphene Nanosheets.* Chemistry of Materials, 2009. **21**(14): p. 3136-3142.
57. Park, C.M., et al., *Li-alloy based anode materials for Li secondary batteries.* Chemical Society Reviews, 2010. **39**(8): p. 3115-3141.
58. Han, M.Y., et al., *Energy band-gap engineering of graphene nanoribbons.* Physical Review Letters, 2007. **98**(20): p. -.
59. Lui, C.H., et al., *Ultraflat graphene.* Nature, 2009. **462**(7271): p. 339-341.
60. Elias, D.C., et al., *Control of Graphene's Properties by Reversible Hydrogenation: Evidence for Graphane.* Science, 2009. **323**(5914): p. 610-613.
61. Szabo, T., et al., *Evolution of surface functional groups in a series of progressively oxidized graphite oxides.* Chemistry of Materials, 2006. **18**(11): p. 2740-2749.
62. Lerf, A., et al., *Structure of graphite oxide revisited.* Journal of Physical Chemistry B, 1998. **102**(23): p. 4477-4482.
63. He, H.Y., et al., *A new structural model for graphite oxide.* Chemical Physics Letters, 1998. **287**(1-2): p. 53-56.
64. Cai, W.W., et al., *Synthesis and solid-state NMR structural characterization of (13)C-labeled graphite oxide.* Science, 2008. **321**(5897): p. 1815-1817.
65. Gao, W., et al., *New insights into the structure and reduction of graphite oxide.* Nature Chemistry, 2009. **1**(5): p. 403-408.
66. Paredes, J.I., et al., *Atomic Force and Scanning Tunneling Microscopy Imaging of Graphene Nanosheets Derived from Graphite Oxide.* Langmuir, 2009. **25**(10): p. 5957-5968.
67. Gomez-Navarro, C., et al., *Electronic transport properties of individual chemically reduced graphene oxide sheets.* Nano letters, 2007. **7**(11): p. 3499-3503.
68. Pacile, D., et al., *Electronic properties and atomic structure of graphene oxide membranes.* Carbon, 2011. **49**(3): p. 966-972.
69. Mao, S., H.H. Pu, and J.H. Chen, *Graphene oxide and its reduction: modeling and experimental progress.* Rsc Advances, 2012. **2**(7): p. 2643-2662.
70. Nakajima, T., A. Mabuchi, and R. Hagiwara, *A New Structure Model of Graphite Oxide.* Carbon, 1988. **26**(3): p. 357-361.
71. Geim, A.K. and K.S. Novoselov, *The rise of graphene.* Nature Materials, 2007. **6**(3): p. 183-191.
72. Schedin, F., et al., *Detection of individual gas molecules adsorbed on graphene.* Nature Materials, 2007. **6**(9): p. 652-655.
73. Geim, A.K., *Graphene: Status and Prospects.* Science, 2009. **324**(5934): p. 5.
74. Pisana, S., et al., *Breakdown of the adiabatic Born-Oppenheimer approximation in graphene.* Nature Materials, 2007. **6**(3): p. 198-201.
75. Rao, C.N.R., et al., *Graphene: The New Two-Dimensional Nanomaterial.* Angewandte Chemie-International Edition, 2009. **48**(42): p. 7752-7777.
76. Jung, I., et al., *Tunable Electrical Conductivity of Individual Graphene Oxide Sheets Reduced at "Low" Temperatures.* Nano Letters, 2008. **8**(12): p. 4283-4287.

77. Becerril, H.A., et al., *Evaluation of solution-processed reduced graphene oxide films as transparent conductors.* ACS Nano, 2008. **2**(3): p. 463-470.
78. Eda, G., et al., *Blue Photoluminescence from Chemically Derived Graphene Oxide.* Advanced Materials, 2010. **22**(4): p. 505-+.
79. Wei, Z.Q., et al., *Nanoscale Tunable Reduction of Graphene Oxide for Graphene Electronics.* Science, 2010. **328**(5984): p. 1373-1376.
80. Luo, D.C., et al., *Evaluation Criteria for Reduced Graphene Oxide.* Journal of Physical Chemistry C, 2011. **115**(23): p. 11327-11335.
81. Lee, G., K.S. Kim, and K. Cho, *Theoretical Study of the Electron Transport in Graphene with Vacancy and Residual Oxygen Defects after High-Temperature Reduction.* Journal of Physical Chemistry C, 2011. **115**(19): p. 9719-9725.
82. Eda, G., et al., *Insulator to Semimetal Transition in Graphene Oxide.* Journal of Physical Chemistry C, 2009. **113**(35): p. 15768-15771.
83. Lomeda, J.R., et al., *Diazonium Functionalization of Surfactant-Wrapped Chemically Converted Graphene Sheets.* Journal of the American Chemical Society, 2008. **130**(48): p. 16201-16206.
84. Liu, H., et al., *Processing of Graphene for Electrochemical Application: Noncovalently Functionalize Graphene Sheets with Water-Soluble Electroactive Methylene Green.* Langmuir, 2009. **25**(20): p. 12006-12010.
85. Meryl D. Stoller, S.P., Yanwu Zhu, Jinho An and Rodney S. Ruoff, *Graphene-Based Ultracapacitors.* Nano letters, 2008. **8**(10): p. 5.
86. Pham, V.H., et al., *Fast and simple fabrication of a large transparent chemically-converted graphene film by spray-coating.* Carbon, 2010. **48**(7): p. 1945-1951.
87. Robinson, J.T., et al., *Reduced Graphene Oxide Molecular Sensors.* Nano letters, 2008. **8**(10): p. 3137-3140.
88. Tung, V.C., et al., *High-throughput solution processing of large-scale graphene.* Nature Nanotechnology, 2009. **4**(1): p. 25-29.
89. Park, S., et al., *Aqueous Suspension and Characterization of Chemically Modified Graphene Sheets.* Chemistry of Materials, 2008. **20**(21): p. 6592-6594.
90. Wang, Y., Y. Wan, and D. Zhang, *Reduced graphene sheets modified glassy carbon electrode for electrocatalytic oxidation of hydrazine in alkaline media.* Electrochemistry Communications, 2010. **12**(2): p. 187-190.
91. Shao, Y.Y., et al., *Facile and controllable electrochemical reduction of graphene oxide and its applications.* Journal of Materials Chemistry, 2010. **20**(4): p. 743-748.
92. Wang, Z.J., et al., *Direct Electrochemical Reduction of Single-Layer Graphene Oxide and Subsequent Functionalization with Glucose Oxidase.* Journal of Physical Chemistry C, 2009. **113**(32): p. 14071-14075.
93. An, S.J., et al., *Thin Film Fabrication and Simultaneous Anodic Reduction of Deposited Graphene Oxide Platelets by Electrophoretic Deposition.* Journal of Physical Chemistry Letters, 2010. **1**(8): p. 1259-1263.
94. Ramesha, G.K. and S. Sampath, *Electrochemical Reduction of Oriented Graphene Oxide Films: An in Situ Raman Spectroelectrochemical Study.* Journal of Physical Chemistry C, 2009. **113**(19): p. 7985-7989.

95. Microscopy, A.F., *Atomic Force Microscopy*. 2005.
96. Wang, D.W., et al., *Electrochemical interfacial capacitance in multilayer graphene sheets: Dependence on number of stacking layers.* Electrochemistry Communications, 2009. **11**(9): p. 1729-1732.
97. Ferraro, J.R. and K. Nakamoto, *Introductory Raman Spectroscopy*. 1994: Access Online via Elsevier.
98. Zhou, M., et al., *Controlled Synthesis of Large-Area and Patterned Electrochemically Reduced Graphene Oxide Films.* Chemistry-a European Journal, 2009. **15**(25): p. 6116-6120.
99. Steinhardt, R.G. and E.J. Serfass, *Surface Analysis with the X-Ray Photoelectron Spectrometer.* Analytical Chemistry, 1953. **25**(5): p. 697-700.
100. Joshi, M., A. Bhattacharyya, and S.W. Ali, *Characterization techniques for nanotechnology applications in textiles.* Indian Journal of Fiber and Textile Research, 2008. **33**: p. 304-317.
101. Niyogi, S., et al., *Solution properties of graphite and graphene.* Journal of the American Chemical Society, 2006. **128**(24): p. 7720-7721.
102. Liu, Z.B., et al., *Porphyrin and Fullerene Covalently Functionalized Graphene Hybrid Materials with Large Nonlinear Optical Properties.* Journal of Physical Chemistry B, 2009. **113**(29): p. 9681-9686.
103. Lee, C., et al., *Frictional Characteristics of Atomically Thin Sheets.* Science, 2010. **328**(5974): p. 76-80.
104. Kim, K.S., et al., *Chemical Vapor Deposition-Grown Graphene: The Thinnest Solid Lubricant.* ACS Nano, 2011. **5**(6): p. 5107-5114.
105. Chen, S.S., et al., *Oxidation Resistance of Graphene-Coated Cu and Cu/Ni Alloy.* ACS Nano, 2011. **5**(2): p. 1321-1327.
106. O'Hern, S.C., et al., *Selective Molecular Transport through Intrinsic Defects in a Single Layer of CVD Graphene.* ACS Nano, 2012. **6**(11): p. 10130-10138.
107. Lee, C.Y., et al., *Coherence Resonance in a Single-Walled Carbon Nanotube Ion Channel.* Science, 2010. **329**(5997): p. 1320-1324.
108. Zhu, Y.W., et al., *Carbon-Based Supercapacitors Produced by Activation of Graphene.* Science, 2011. **332**(6037): p. 1537-1541.
109. Holt, J.K., et al., *Fast mass transport through sub-2-nanometer carbon nanotubes.* Science, 2006. **312**(5776): p. 1034-1037.
110. Koenig, S.P., et al., *Ultrastrong adhesion of graphene membranes.* Nature Nanotechnology, 2011. **6**(9): p. 543-6.
111. Shin, Y.J., et al., *Surface-energy engineering of graphene.* Langmuir : the ACS journal of surfaces and colloids, 2010. **26**(6): p. 3798-802.
112. Goncalves, G., et al., *Surface Modification of Graphene Nanosheets with Gold Nanoparticles: The Role of Oxygen Moieties at Graphene Surface on Gold Nucleation and Growth.* Chemistry of Materials, 2009. **21**(20): p. 4796-4802.
113. Wang, Y., et al., *Application of graphene-modified electrode for selective detection of dopamine.* Electrochemistry Communications, 2009. **11**(4): p. 889-892.
114. Rafiee, J., et al., *Wetting transparency of graphene.* Nature Materials, 2012. **11**(3): p. 217-22.

115. Afshari, A., et al., *Emission of phthalates from PVC and other materials.* Indoor Air, 2004. **14**(2): p. 120-128.
116. Fang, M., et al., *Covalent polymer functionalization of graphene nanosheets and mechanical properties of composites.* Journal of Materials Chemistry, 2009. **19**(38): p. 7098-7105.
117. Rosca, I.D., et al., *Oxidation of multiwalled carbon nanotubes by nitric acid.* Carbon, 2005. **43**(15): p. 3124-3131.
118. Becker, L., R.J. Poreda, and T.E. Bunch, *Fullerenes: An extraterrestrial carbon carrier phase for noble gases.* Proceedings of the National Academy of Sciences of the United States of America, 2000. **97**(7): p. 2979-2983.
119. Hummers, W.S. and R.E. Offeman, *Preparation of Graphitic Oxide.* Journal of the American Chemical Society, 1958. **80**(6): p. 1339-1339.
120. Kovtyukhova, N.I., et al., *Layer-by-layer assembly of ultrathin composite films from micron-sized graphite oxide sheets and polycations.* Chemistry of Materials, 1999. **11**(3): p. 771-778.
121. Marcano, D.C., et al., *Improved Synthesis of Graphene Oxide.* Acs Nano, 2010. **4**(8): p. 4806-4814.
122. Pan, D.Y., et al., *Hydrothermal Route for Cutting Graphene Sheets into Blue-Luminescent Graphene Quantum Dots.* Advanced Materials, 2010. **22**(6): p. 734-+.
123. Wu, Z.S., et al., *Synthesis of Graphene Sheets with High Electrical Conductivity and Good Thermal Stability by Hydrogen Arc Discharge Exfoliation.* Acs Nano, 2009. **3**(2): p. 411-417.
124. Li, X.L., et al., *Simultaneous Nitrogen Doping and Reduction of Graphene Oxide.* Journal of the American Chemical Society, 2009. **131**(43): p. 15939-15944.
125. Lopez, V., et al., *Chemical Vapor Deposition Repair of Graphene Oxide: A Route to Highly Conductive Graphene Monolayers.* Advanced Materials, 2009. **21**(46): p. 4683-+.
126. Gengler, R.Y.N., et al., *Large-Yield Preparation of High-Electronic-Quatity Graphene by a Langmuir-Schaefer Approach.* Small, 2010. **6**(1): p. 35-39.
127. Su, Q., et al., *Composites of Graphene with Large Aromatic Molecules.* Advanced Materials, 2009. **21**(31): p. 3191-+.
128. He, T.C., et al., *Enhanced Optical Nonlinearity in Noncovalently Functionalized Amphiphilic Graphene Composites.* Chempluschem, 2012. **77**(8): p. 688-693.
129. Dan Li, M.B.M., Scott Gilje, Richard B. Kaner & Gordon G. Wallace, *Processable aqueous dispersions of graphene nanosheets.* Nature Nanotechnology, 2008. **3**: p. 5.
130. Fernandez-Merino, M., et al., *Vitamin C is an ideal substitute for hydrazine in the reduction of graphene oxide suspensions.* The Journal of Physical Chemistry C, 2010. **114**(14): p. 6426-6432.
131. Gilje, S., et al., *A chemical route to graphene for device applications.* Nano letters, 2007. **7**(11): p. 3394-3398.
132. Chen, H., et al., *Mechanically strong, electrically conductive, and biocompatible graphene paper.* Advanced Materials, 2008. **20**(18): p. 3557-+.

133. Zhu, Y.W., et al., *Transparent self-assembled films of reduced graphene oxide platelets.* Applied Physics Letters, 2009. **95**(10).
134. Kotov, N.A., I. Dekany, and J.H. Fendler, *Ultrathin graphite oxide-polyelectrolyte composites prepared by self-assembly: Transition between conductive and non-conductive states.* Advanced Materials, 1996. **8**(8): p. 637-&.
135. Yin, Z.Y., et al., *Electrochemical Deposition of ZnO Nanorods on Transparent Reduced Graphene Oxide Electrodes for Hybrid Solar Cells.* Small, 2010. **6**(2): p. 307-312.
136. Robinson, J.T., et al., *Wafer-scale Reduced Graphene Oxide Films for Nanomechanical Devices.* Nano Letters, 2008. **8**(10): p. 3441-3445.
137. He, Q.Y., et al., *Centimeter-Long and Large-Scale Micropatterns of Reduced Graphene Oxide Films: Fabrication and Sensing Applications.* Acs Nano, 2010. **4**(6): p. 3201-3208.
138. Shin, H.J., et al., *Efficient Reduction of Graphite Oxide by Sodium Borohydrilde and Its Effect on Electrical Conductance.* Advanced Functional Materials, 2009. **19**(12): p. 1987-1992.
139. Pei, S., et al., *Direct reduction of graphene oxide films into highly conductive and flexible graphene films by hydrohalic acids.* Carbon, 2010. **48**(15): p. 4466-4474.
140. Wu, S.X., et al., *Electrochemical Deposition of Semiconductor Oxides on Reduced Graphene Oxide-Based Flexible, Transparent, and Conductive Electrodes.* Journal of Physical Chemistry C, 2010. **114**(27): p. 11816-11821.
141. Wang, D., et al., *Ternary Self-Assembly of Ordered Metal Oxide−Graphene Nanocomposites for Electrochemical Energy Storage.* ACS Nano, 2010. **4**(3): p. 1587-1595.
142. Wu, Z.S., et al., *Graphene/metal oxide composite electrode materials for energy storage.* Nano Energy, 2012. **1**(1): p. 107-131.
143. Dong, L.F., et al., *Graphene-supported platinum and platinum-ruthenium nanoparticles with high electrocatalytic activity for methanol and ethanol oxidation.* Carbon, 2010. **48**(3): p. 781-787.
144. Paek, S.M., E. Yoo, and I. Honma, *Enhanced Cyclic Performance and Lithium Storage Capacity of SnO(2)/Graphene Nanoporous Electrodes with Three-Dimensionally Delaminated Flexible Structure.* Nano letters, 2009. **9**(1): p. 72-75.
145. Chang, H.X., et al., *Quantum dots sensitized graphene: In situ growth and application in photoelectrochemical cells.* Electrochemistry Communications, 2010. **12**(3): p. 483-487.
146. Dong, H.F., et al., *Fluorescence Resonance Energy Transfer between Quantum Dots and Graphene Oxide for Sensing Biomolecules.* Analytical Chemistry, 2010. **82**(13): p. 5511-5517.
147. Wang, K., et al., *Graphene enhanced electrochemiluminescence of CdS nanocrystal for H2O2 sensing.* Talanta, 2010. **82**(1): p. 372-376.
148. Jin, E., et al., *Fabrication of graphene/prussian blue composite nanosheets and their electrocatalytic reduction of H2O2.* Electrochimica Acta, 2010. **55**(24): p. 7230-7234.

149. Wang, H.L., et al., *Ni(OH)(2) Nanoplates Grown on Graphene as Advanced Electrochemical Pseudocapacitor Materials.* Journal of the American Chemical Society, 2010. **132**(21): p. 7472-7477.
150. Petit, C. and T.J. Bandosz, *Graphite Oxide/Polyoxometalate Nanocomposites as Adsorbents of Ammonia.* Journal of Physical Chemistry C, 2009. **113**(9): p. 3800-3809.
151. Chen, S., J.W. Zhu, and X. Wang, *One-Step Synthesis of Graphene-Cobalt Hydroxide Nanocomposites and Their Electrochemical Properties.* Journal of Physical Chemistry C, 2010. **114**(27): p. 11829-11834.
152. Rempel, J.Y., et al., *Properties of the CdSe(0001), (0001), and (1120) single crystal surfaces: Relaxation, reconstruction, and adatom and admolecule adsorption.* Journal of Physical Chemistry B, 2005. **109**(41): p. 19320-19328.
153. Kelly, K.L., et al., *The optical properties of metal nanoparticles: The influence of size, shape, and dielectric environment.* Journal of Physical Chemistry B, 2003. **107**(3): p. 668-677.
154. Choi, D., et al., *Fully Rollable Transparent Nanogenerators Based on Graphene Electrodes.* Advanced Materials, 2010. **22**(19): p. 2187-+.
155. Wu, Z.S., et al., *Field Emission of Single-Layer Graphene Films Prepared by Electrophoretic Deposition.* Advanced Materials, 2009. **21**(17): p. 1756-+.
156. Li, Y., et al., *Palladium nanoparticle-graphene hybrids as active catalysts for the Suzuki reaction.* Nano Research, 2010. **3**(6): p. 429-437.
157. Wu, J.B., et al., *Organic solar cells with solution-processed graphene transparent electrodes.* Applied Physics Letters, 2008. **92**(26).
158. Zhang, H., et al., *P25-Graphene Composite as a High Performance Photocatalyst.* Acs Nano, 2010. **4**(1): p. 380-386.
159. Dimitrakakis, G.K., E. Tylianakis, and G.E. Froudakis, *Pillared Graphene: A New 3-D Network Nanostructure for Enhanced Hydrogen Storage.* Nano Letters, 2008. **8**(10): p. 3166-3170.
160. Neto, A.H.C. and K. Novoselov, *Two-Dimensional Crystals: Beyond Graphene.* Materials Express, 2011. **1**(1): p. 10-17.
161. Kim, K.S., et al., *Large-scale pattern growth of graphene films for stretchable transparent electrodes.* Nature, 2009. **457**(7230): p. 706-710.
162. Bae, S., et al., *Roll-to-roll production of 30-inch graphene films for transparent electrodes.* Nature Nanotechnology, 2010. **5**(8): p. 574-578.
163. Dikin, D.A., et al., *Preparation and characterization of graphene oxide paper.* Nature, 2007. **448**(7152): p. 457-460.
164. Stankovich, S., et al., *Graphene-based composite materials.* Nature, 2006. **442**(7100): p. 282-286.
165. Liang, M.H. and L.J. Zhi, *Graphene-based electrode materials for rechargeable lithium batteries.* Journal of Materials Chemistry, 2009. **19**(33): p. 5871-5878.
166. Yoo, E., et al., *Large reversible Li storage of graphene nanosheet families for use in rechargeable lithium ion batteries.* Nano letters, 2008. **8**(8): p. 2277-2282.
167. Winter, M., et al., *Insertion electrode materials for rechargeable lithium batteries.* Advanced Materials, 1998. **10**(10): p. 725-763.

168. Masarapu, C., et al., *Long-Cycle Electrochemical Behavior of Multiwall Carbon Nanotubes Synthesized on Stainless Steel in Li Ion Batteries.* Advanced Functional Materials, 2009. **19**(7): p. 1008-1014.
169. Yoon, S.H., et al., *Novel carbon nanofibers of high graphitization as anodic materials for lithium ion secondary batteries.* Carbon, 2004. **42**(1): p. 21-32.
170. Wang, G.X., et al., *Graphene nanosheets for enhanced lithium storage in lithium ion batteries.* Carbon, 2009. **47**(8): p. 2049-2053.
171. Poizot, P., et al., *Nano-sized transition-metaloxides as negative-electrode materials for lithium-ion batteries.* Nature, 2000. **407**(6803): p. 496-499.
172. Qi, X.Y., et al., *Amphiphilic Graphene Composites.* Angewandte Chemie-International Edition, 2010. **49**(49): p. 9426-9429.
173. Qi, X.Y., et al., *Conjugated-Polyelectrolyte-Functionalized Reduced Graphene Oxide with Excellent Solubility and Stability in Polar Solvents.* Small, 2010. **6**(5): p. 663-669.
174. He, Q.Y., et al., *Transparent, Flexible, All-Reduced Graphene Oxide Thin Film Transistors.* Acs Nano, 2011. **5**(6): p. 5038-5044.
175. Jeong, H.K., et al., *Thermal stability of graphite oxide.* Chemical Physics Letters, 2009. **470**(4-6): p. 255-258.
176. Yao, J., et al., *In situ chemical synthesis of SnO2-graphene nanocomposite as anode materials for lithium-ion batteries.* Electrochemistry Communications, 2009. **11**(10): p. 1849-1852.
177. Zhang, L.S., et al., *Mono dispersed SnO2 nanoparticles on both sides of single layer graphene sheets as anode materials in Li-ion batteries.* Journal of Materials Chemistry, 2010. **20**(26): p. 5462-5467.
178. Du, Z.F., et al., *In situ synthesis of SnO2/graphene nanocomposite and their application as anode material for lithium ion battery.* Materials Letters, 2010. **64**(19): p. 2076-2079.
179. Zhang, M., et al., *Fast synthesis of SnO2/graphene composites by reducing graphene oxide with stannous ions.* Journal of Materials Chemistry, 2011. **21**(6): p. 1673-1676.
180. Wang, X.M., et al., *Manipulation of Graphene Properties by Interface Engineering.* 2011 International Conference on Semiconductor Technology for Ultra Large Scale Integrated Circuits and Thin Film Transistors (Ulsic Vs. Tft), 2011. **37**(1): p. 133-139.
181. Lian, P.C., et al., *High reversible capacity of SnO2/graphene nanocomposite as an anode material for lithium-ion batteries.* Electrochimica Acta, 2011. **56**(12): p. 4532-4539.
182. Ding, S.J., et al., *SnO2 nanosheets grown on graphene sheets with enhanced lithium storage properties.* Chemical Communications, 2011. **47**(25): p. 7155-7157.
183. Zhao, B., et al., *Bivalent tin ion assisted reduction for preparing graphene/SnO2 composite with good cyclic performance and lithium storage capacity.* Electrochimica Acta, 2011. **56**(21): p. 7340-7346.
184. Wu, Z.S., et al., *Graphene Anchored with Co3O4 Nanoparticles as Anode of Lithium Ion Batteries with Enhanced Reversible Capacity and Cyclic Performance.* Acs Nano, 2010. **4**(6): p. 3187-3194.
185. Zhang, B.A., et al., *SnO2-graphene-carbon nanotube mixture for anode material with improved rate capacities.* Carbon, 2011. **49**(13): p. 4524-4534.

186. Chen, S.Q. and Y. Wang, *Microwave-assisted synthesis of a Co3O4-graphene sheet-on-sheet nanocomposite as a superior anode material for Li-ion batteries.* Journal of Materials Chemistry, 2010. **20**(43): p. 9735-9739.
187. Wang, X., et al., *Synthesis and Lithium Storage Properties of Co3O4 Nanosheet-Assembled Multishelled Hollow Spheres.* Advanced Functional Materials, 2010. **20**(10): p. 1680-1686.
188. Zhou, W.W., et al., *A general strategy toward graphene@metal oxide core-shell nanostructures for high-performance lithium storage.* Energy & Environmental Science, 2011. **4**(12): p. 4954-4961.
189. Hsieh, C.T., C.Y. Lin, and J.Y. Lin, *High reversibility of Li intercalation and de-intercalation in MnO-attached graphene anodes for Li-ion batteries.* Electrochimica Acta, 2011. **56**(24): p. 8861-8867.
190. Yang, S.B., et al., *Fabrication of Graphene-Encapsulated Oxide Nanoparticles: Towards High-Performance Anode Materials for Lithium Storage.* Angewandte Chemie-International Edition, 2010. **49**(45): p. 8408-8411.
191. Zhu, N., et al., *Graphene as a conductive additive to enhance the high-rate capabilities of electrospun Li4Ti5O12 for lithium-ion batteries.* Electrochimica Acta, 2010. **55**(20): p. 5813-5818.
192. Zhu, X.J., et al., *Nanostructured Reduced Graphene Oxide/Fe2O3 Composite As a High-Performance Anode Material for Lithium Ion Batteries.* Acs Nano, 2011. **5**(4): p. 3333-3338.
193. Zhang, M., et al., *Magnetite/graphene composites: microwave irradiation synthesis and enhanced cycling and rate performances for lithium ion batteries.* Journal of Materials Chemistry, 2010. **20**(26): p. 5538-5543.
194. Wang, G., et al., *Preparation of Fe2O3/graphene composite and its electrochemical performance as an anode material for lithium ion batteries.* Journal of Alloys and Compounds, 2011. **509**(24): p. L216-L220.
195. Behera, S.K., *Enhanced rate performance and cyclic stability of Fe3O4-graphene nanocomposites for Li ion battery anodes.* Chemical Communications, 2011. **47**(37): p. 10371-10373.
196. Su, J., et al., *Fe3O4-Graphene Nanocomposites with Improved Lithium Storage and Magnetism Properties.* Journal of Physical Chemistry C, 2011. **115**(30): p. 14469-14477.
197. Zhou, J.S., et al., *Magnetite/graphene nanosheet composites: interfacial interaction and its impact on the durable high-rate performance in lithium-ion batteries.* Rsc Advances, 2011. **1**(5): p. 782-791.
198. Huang, H.J. and X. Wang, *Graphene nanoplate-MnO2 composites for supercapacitors: a controllable oxidation approach.* Nanoscale, 2011. **3**(8): p. 3185-3191.
199. Li, B.J., et al., *Superparamagnetic Fe3O4 nanocrystals@graphene composites for energy storage devices.* Journal of Materials Chemistry, 2011. **21**(13): p. 5069-5075.
200. Kottegoda, I.R.M., et al., *Synthesis and characterization of graphene-nickel oxide nanostructures for fast charge-discharge application.* Electrochimica Acta, 2011. **56**(16): p. 5815-5822.

201. Choi, D.W., et al., *Li-ion batteries from LiFePO4 cathode and anatase/graphene composite anode for stationary energy storage.* Electrochemistry Communications, 2010. **12**(3): p. 378-381.
202. Ding, S.J., et al., *Graphene-supported anatase TiO2 nanosheets for fast lithium storage.* Chemical Communications, 2011. **47**(20): p. 5780-5782.
203. Wang, B., et al., *Synthesis of CuO/graphene nanocomposite as a high-performance anode material for lithium-ion batteries.* Journal of Materials Chemistry, 2010. **20**(47): p. 10661-10664.
204. Yang, S.B., et al., *Graphene-Based Nanosheets with a Sandwich Structure.* Angewandte Chemie-International Edition, 2010. **49**(28): p. 4795-4799.
205. Yu, A.P., et al., *Free-Standing Layer-By-Layer Hybrid Thin Film of Graphene-MnO2 Nanotube as Anode for Lithium Ion Batteries.* Journal of Physical Chemistry Letters, 2011. **2**(15): p. 1855-1860.
206. Guo, C.X., et al., *A Hierarchically Nanostructured Composite of MnO2/Conjugated Polymer/Graphene for High-Performance Lithium Ion Batteries.* Advanced Energy Materials, 2011. **1**(5): p. 736-741.
207. Mai, Y.J., et al., *CuO/graphene composite as anode materials for lithium-ion batteries.* Electrochimica Acta, 2011. **56**(5): p. 2306-2311.
208. Liu, H.D., et al., *Li3V2(PO4)(3)/graphene nanocomposites as cathode material for lithium ion batteries.* Chemical Communications, 2011. **47**(32): p. 9110-9112.
209. Wang, D.H., et al., *Self-Assembled TiO2-Graphene Hybrid Nanostructures for Enhanced Li-Ion Insertion.* ACS Nano, 2009. **3**(4): p. 907-914.
210. Wang, G., et al., *Prepartion and electrochemical performance of a cerium oxide-graphene nanocomposite as the anode material of a lithium ion battery.* Scripta Materialia, 2011. **65**(4): p. 339-342.
211. Xu, C., et al., *Fabrication of a graphene-cuprous oxide composite.* Journal of Solid State Chemistry, 2009. **182**(9): p. 2486-2490.
212. Yang, S.B., X.L. Feng, and K. Mullen, *Sandwich-Like, Graphene-Based Titania Nanosheets with High Surface Area for Fast Lithium Storage.* Advanced Materials, 2011. **23**(31): p. 3575-+.
213. Shi, Y., et al., *Nanosized Li4Ti5O12/graphene hybrid materials with low polarization for high rate lithium ion batteries.* Journal of Power Sources, 2011. **196**(20): p. 8610-8617.
214. Li, N., et al., *Battery Performance and Photocatalytic Activity of Mesoporous Anatase TiO2 Nanospheres/Graphene Composites by Template-Free Self-Assembly.* Advanced Functional Materials, 2011. **21**(9): p. 1717-1722.
215. Zhou, G.M., et al., *Graphene-Wrapped Fe3O4 Anode Material with Improved Reversible Capacity and Cyclic Stability for Lithium Ion Batteries.* Chemistry of Materials, 2010. **22**(18): p. 5306-5313.
216. Sun, Y.M., et al., *Self-Assembled Hierarchical MoO2/Graphene Nanoarchitectures and Their Application as a High-Performance Anode Material for Lithium-Ion Batteries.* Acs Nano, 2011. **5**(9): p. 7100-7107.

217. Liu, H.M. and W.S. Yang, *Ultralong single crystalline V2O5 nanowire/graphene composite fabricated by a facile green approach and its lithium storage behavior.* Energy & Environmental Science, 2011. **4**(10): p. 4000-4008.
218. Wang, J.Z., et al., *Graphene-Encapsulated Fe3O4 Nanoparticles with 3D Laminated Structure as Superior Anode in Lithium Ion Batteries.* Chemistry-a European Journal, 2011. **17**(2): p. 661-667.
219. Chen, D.Y., et al., *Graphene-Encapsulated Hollow Fe3O4 Nanoparticle Aggregates As a High-Performance Anode Material for Lithium Ion Batteries.* Acs Applied Materials & Interfaces, 2011. **3**(8): p. 3078-3083.
220. Qiu, Y.C., et al., *Synthesis of Size-Tunable Anatase TiO2 Nanospindles and Their Assembly into Anatase@Titanium Oxynitride/Titanium Nitride-Graphene Nanocomposites for Rechargeable Lithium Ion Batteries with High Cycling Performance.* Acs Nano, 2010. **4**(11): p. 6515-6526.
221. Zou, Y.Q. and Y. Wang, *NiO nanosheets grown on graphene nanosheets as superior anode materials for Li-ion batteries.* Nanoscale, 2011. **3**(6): p. 2615-2620.
222. Wu, Z.S., et al., *Anchoring Hydrous RuO2 on Graphene Sheets for High-Performance Electrochemical Capacitors.* Advanced Functional Materials, 2010. **20**(20): p. 3595-3602.
223. Prakash, A.S., et al., *Solution-Combustion Synthesized Nanocrystalline Li4Ti5O12 As High-Rate Performance Li-Ion Battery Anode.* Chemistry of Materials, 2010. **22**(9): p. 2857-2863.
224. Zhou, X.F., et al., *Graphene modified LiFePO4 cathode materials for high power lithium ion batteries.* Journal of Materials Chemistry, 2011. **21**(10): p. 3353-3358.
225. Zuo, P.P., et al., *Fabrication of biocompatible and mechanically reinforced graphene oxide-chitosan nanocomposite films.* Chemistry Central Journal, 2013. **7**.
226. *Mixed Cellulose Ester Membranes*. Available from: http://www.whatman.com/MixedCelluloseEsterMembranes.aspx.
227. *Anodisc pore structure*. Available from: http://www.whatman.com/PRODAnoporeInorganicMembranes.aspx.
228. *Holey carbon films - Nickel*. Available from: http://www.agarscientific.com/tem/coated-grids/holey-carbon-films-7087.html.
229. *Thermal Oxide Wafer: 300 nm SiO2 Layer on Si (100), 2" dia x 0.50 mm t, P type , 1 side polished,R:<0.005 ohm.cm*. Available from: http://www.mtixtl.com/si-so-ba50d300nm.aspx.
230. Giessibl, F.J., *Advances in atomic force microscopy*. Reviews of Modern Physics, 2003. **75**(3): p. 949-983.
231. Smith, W.F. and J. Hashemi, *Foundations of materials science and engineering*. 5th ed. 2010, Boston, Mass.: McGraw-Hill. xviii, 1068 p.
232. Donald, A.M., *The use of environmental scanning electron microscopy for imaging wet and insulating materials.* Nature Materials, 2003. **2**(8): p. 511-516.
233. *Scheme TEM en.*
234. Spence, J.C.H., *Experimental high-resolution electron microscopy*. Monographs on the physics and chemistry of materials. 1981, Oxford New York: Clarendon Press ; Oxford University Press. xii, 370 p.

235. Vickerman, J.C. and I.S. Gilmore, *Surface analysis : the principal techniques*. 2nd ed. 2009, Chichester, U.K.: Wiley. xix, 666 p.
236. Buschow, K.H.J., *Encyclopedia of materials : science and technology*. 2001, Amsterdam ; New York: Elsevier.
237. Martin, P.M. and Books24x7 Inc., *Handbook of deposition technologies for films and coatings science, applications and technology, third edition*. 2010, William Andrew/Elsevier,: Oxford, U.K. ; Burlington, Mass.
238. Hüfner, S., *Photoelectron spectroscopy : principles and applications*. 3rd ed. Advanced texts in physics. 2003, Berlin ; New York: Springer. xv, 662 p.
239. Smith, B.C., *Fundamentals of Fourier transform infrared spectroscopy*. 2nd ed. 2011, Boca Raton, FL: CRC Press. xiii, 193 p.
240. Faix, O., *Fourier transform infrared spectroscopy*, in *Methods in lignin chemistry*. 1992, Springer. p. 83-109.
241. Hind, A.R., S.K. Bhargava, and A. McKinnon, *At the solid/liquid interface: FTIR/ATR - the tool of choice.* Advances in Colloid and Interface Science, 2001. **93**(1-3): p. 91-114.
242. Pauw, L.J.v.d., *A new method of measuring the resistivity and Hall coefficients on lamellae of arbitrary shape.* Philips technical review, 1958. **20**: p. 220-224.
243. Sze, S.M. and M.K. Lee, *Semiconductor devices, physics and technology*. 3rd ed. 2012, Hoboken, N.J.: Wiley. ix, 578 p.
244. Kwok, D.Y., et al., *Contact Angle Measurements and Contact Angle Interpretation. 1. Contact Angle Measurements by Axisymmetric Drop Shape Analysis and a Goniometer Sessile Drop Technique.* Langmuir, 1997. **13**(10): p. 2880-2894.
245. Buschow, K.H.J., et al., *Encyclopedia of Materials - Science and Technology, Volumes 1-11*. 2001, Elsevier.
246. Woodward, R.P., *FTÅ200 Measurement Capabilities*.
247. Drelich, J., J.S. Laskowski, and K.L. Mittal, *Apparent and Microscopic Contact Angles*. 2000, VSP - An imprint of BRILL. p. 15-18.
248. Ru, L., et al., *Principles of Surface-Enhanced Raman Spectroscopy and Related Plasmonic Effects*. 2009, Elsevier.
249. Sgro, L., et al., *UV-visible spectroscopy of organic carbon particulate sampled from ethylene/air flames.* Chemosphere, 2001. **42**(5): p. 671-680.
250. Gfroerer, T.H., *Photoluminescence in Analysis of Surfaces and Interfaces*, in *Encyclopedia of Analytical Chemistry*. 2006, John Wiley & Sons, Ltd.
251. Suryanarayana, C. and M.G. Norton, *X-Ray diffraction : a practical approach*. 1998, New York: Plenum Press. xiii, 273 p.
252. Brundle, C.R., C.A. Evans, and S. Wilson, *Encyclopedia of materials characterization : surfaces, interfaces, thin films*. Materials characterization series. 1992, Boston Greenwich, CT: Butterworth-Heinemann ; Manning. xix, 751 p.
253. Eda, G., G. Fanchini, and M. Chhowalla, *Large-area ultrathin films of reduced graphene oxide as a transparent and flexible electronic material.* Nature Nanotechnology, 2008. **3**(5): p. 270-274.

254. Zhang, L.M., et al., *Functional Graphene Oxide as a Nanocarrier for Controlled Loading and Targeted Delivery of Mixed Anticancer Drugs.* Small, 2010. **6**(4): p. 537-544.
255. Wassei, J.K., et al., *Stenciling Graphene, Carbon Nanotubes, and Fullerenes Using Elastomeric Lift-Off Membranes.* Advanced Materials, 2010. **22**(8): p. 897-+.
256. Dubin, S., et al., *A One-Step, Solvothermal Reduction Method for Producing Reduced Graphene Oxide Dispersions in Organic Solvents.* ACS Nano, 2010. **4**(7): p. 3845-3852.
257. Khan, U., et al., *High-Concentration Solvent Exfoliation of Graphene.* Small, 2010. **6**(7): p. 864-871.
258. Jung, I., et al., *Simple approach for high-contrast optical imaging and characterization of graphene-based sheets.* Nano Letters, 2007. **7**(12): p. 3569-3575.
259. Lambacher, A. and P. Fromherz, *Fluorescence interference-contrast microscopy on oxidized silicon using a monomolecular dye layer.* Applied Physics a-Materials Science & Processing, 1996. **63**(3): p. 207-216.
260. Ni, Z.H., et al., *Graphene thickness determination using reflection and contrast spectroscopy.* Nano Letters, 2007. **7**(9): p. 2758-2763.
261. Ward, L., *The optical constants of bulk materials and films*. 2nd ed. Optics and optoelectronics series. 1994, Bristol ; Philadelphia: Institute of Physics Pub. xvii, 293 p.
262. Blake, P., et al., *Making graphene visible.* Applied Physics Letters, 2007. **91**(6).
263. Wu, B., et al., *Equiangular Hexagon-Shape-Controlled Synthesis of Graphene on Copper Surface.* Advanced Materials, 2011. **23**(31): p. 3522-+.
264. Huang, P.Y., et al., *Grains and grain boundaries in single-layer graphene atomic patchwork quilts.* Nature, 2011. **469**(7330): p. 389-+.
265. Ferrari, A.C., *Raman spectroscopy of graphene and graphite: Disorder, electron–phonon coupling, doping and nonadiabatic effects* Solid State Communications, 2007. **143**(1-2): p. 11.
266. Meyer, J.C., et al., *On the roughness of single- and bi-layer graphene membranes.* Solid State Communications, 2007. **143**(1-2): p. 101-109.
267. Chen, R.J., et al., *Noncovalent sidewall functionalization of single-walled carbon nanotubes for protein immobilization.* Journal of the American Chemical Society, 2001. **123**(16): p. 3838-3839.
268. Meyer, J.C., et al., *The structure of suspended graphene sheets.* Nature, 2007. **446**(7131): p. 60-63.
269. Joung, D., L. Zhai, and S.I. Khondaker, *Coulomb blockade and hopping conduction in graphene quantum dots array.* Physical Review B, 2011. **83**(11).
270. Bagri, A., et al., *Structural evolution during the reduction of chemically derived graphene oxide.* Nature Chemistry, 2010. **2**(7): p. 581-587.
271. Zhang, Y.B., et al., *Experimental observation of the quantum Hall effect and Berry's phase in graphene.* Nature, 2005. **438**(7065): p. 201-204.
272. Li, X.L., et al., *Chemically derived, ultrasmooth graphene nanoribbon semiconductors.* Science, 2008. **319**(5867): p. 1229-1232.
273. Hernandez, Y., et al., *High-yield production of graphene by liquid-phase exfoliation of graphite.* Nature Nanotechnology, 2008. **3**(9): p. 563-568.

274. Liu, Z.H., et al., *Intercalation of organic ammonium ions into layered graphite oxide.* Langmuir, 2002. **18**(12): p. 4926-4932.
275. Park, S., et al., *Graphene oxide papers modified by divalent ions - Enhancing mechanical properties via chemical cross-linking.* Acs Nano, 2008. **2**(3): p. 572-578.
276. Cote, L.J., F. Kim, and J.X. Huang, *Langmuir-Blodgett Assembly of Graphite Oxide Single Layers.* Journal of the American Chemical Society, 2009. **131**(3): p. 1043-1049.
277. Jeong, H.K., et al., *Evidence of graphitic AB stacking order of graphite oxides.* Journal of the American Chemical Society, 2008. **130**(4): p. 1362-1366.
278. Xu, Y.X., et al., *Flexible graphene films via the filtration of water-soluble noncovalent functionalized graphene sheets.* Journal of the American Chemical Society, 2008. **130**(18): p. 5856-+.
279. Yumitori, S., *Correlation of C-1s chemical state intensities with the O-1s intensity in the XPS analysis of anodically oxidized glass-like carbon samples.* Journal of Materials Science, 2000. **35**(1): p. 139-146.
280. Joung, D. and S.I. Khondaker, *Efros-Shklovskii variable-range hopping in reduced graphene oxide sheets of varying carbon sp(2) fraction.* Physical Review B, 2012. **86**(23).
281. Shin, H.J., et al., *Tailoring electronic structures of carbon nanotubes by solvent with electron-donating and -withdrawing groups.* Journal of the American Chemical Society, 2008. **130**(6): p. 2062-2066.
282. Graupner, R., et al., *Doping of single-walled carbon nanotube bundles by Bronsted acids.* Physical Chemistry Chemical Physics, 2003. **5**(24): p. 5472-5476.
283. Liang, Y.Y., et al., *TiO2 Nanocrystals Grown on Graphene as Advanced Photocatalytic Hybrid Materials.* Nano Research, 2010. **3**(10): p. 701-705.
284. Principe, E.L. and B.A. Shaw, *Observations regarding the effects of nitrogen addition to the aluminum-tungsten system by reactive sputter deposition.* Corrosion, 1997. **53**(9): p. 675-678.
285. Liao, H.M., R.N.S. Sodhi, and T.W. Coyle, *Surface-Composition of Aln Powders Studied by X-Ray Photoelectron-Spectroscopy and Bremsstrahlung-Excited Auger-Electron Spectroscopy.* Journal of Vacuum Science & Technology a-Vacuum Surfaces and Films, 1993. **11**(5): p. 2681-2686.
286. Moulder, J.F. and J. Chastain, *Handbook of X-Ray Photoelectron Spectroscopy: A Reference Book of Standard Spectra for Identification & Interpretation of XPS Data*. 1992: Perkin-Elmer.
287. Tuinstra, F. and J.L. Koenig, *Raman Spectrum of Graphite.* Journal of Chemical Physics, 1970. **53**(3): p. 1126-&.
288. Pimenta, M.A., et al., *Studying disorder in graphite-based systems by Raman spectroscopy.* Physical Chemistry Chemical Physics, 2007. **9**(11): p. 1276-1291.
289. Bourlinos, A.B., et al., *Graphite oxide: Chemical reduction to graphite and surface modification with primary aliphatic amines and amino acids.* Langmuir, 2003. **19**(15): p. 6050-6055.
290. Stankovich, S., et al., *Synthesis and exfoliation of isocyanate-treated graphene oxide nanoplatelets.* Carbon, 2006. **44**(15): p. 3342-3347.

291. Dillon, A.C., et al., *Surface-Chemistry of Al2o3 Deposition Using Al(Ch3)(3) and H2o in a Binary Reaction Sequence.* Surface Science, 1995. **322**(1-3): p. 230-242.
292. Morterra, C., et al., *X-Ray-Diffraction, High-Resolution Transmission Electron-Microscopy and Fourier-Transform Infrared Study of Ca-Doped Al2o3.* Journal of the Chemical Society-Faraday Transactions, 1993. **89**(1): p. 135-150.
293. Chun, D.H., et al., *Catalytic properties of Ni3Al foils for methanol decomposition.* Catalysis Letters, 2006. **106**(1-2): p. 71-75.
294. Su, Z.X. and W.Z. Zhou, *Formation Mechanism of Porous Anodic Aluminium and Titanium Oxides.* Advanced Materials, 2008. **20**(19): p. 3663-+.
295. Campbell, T., et al., *Dynamics of oxidation of aluminum nanoclusters using variable charge molecular-dynamics simulations on parallel computers.* Physical Review Letters, 1999. **82**(24): p. 4866-4869.
296. Wang, X.R., S.M. Tabakman, and H.J. Dai, *Atomic layer deposition of metal oxides on pristine and functionalized graphene.* Journal of the American Chemical Society, 2008. **130**(26): p. 8152-+.
297. Muszynski, R., B. Seger, and P.V. Kamat, *Decorating graphene sheets with gold nanoparticles.* Journal of Physical Chemistry C, 2008. **112**(14): p. 5263-5266.
298. Scheuermann, G.M., et al., *Palladium Nanoparticles on Graphite Oxide and Its Functionalized Graphene Derivatives as Highly Active Catalysts for the Suzuki-Miyaura Coupling Reaction.* Journal of the American Chemical Society, 2009. **131**(23): p. 8262-8270.
299. Tan, Y.W., et al., *Measurement of scattering rate and minimum conductivity in graphene.* Physical Review Letters, 2007. **99**(24).
300. Martin, J., et al., *Observation of electron-hole puddles in graphene using a scanning single-electron transistor.* Nature Physics, 2008. **4**(2): p. 144-148.
301. Wehling, T.O., et al., *Molecular doping of graphene.* Nano letters, 2008. **8**(1): p. 173-177.
302. Boukhvalov, D.W. and M.I. Katsnelson, *Modeling of graphite oxide.* Journal of the American Chemical Society, 2008. **130**(32): p. 10697-10701.
303. Das, A., et al., *Monitoring dopants by Raman scattering in an electrochemically top-gated graphene transistor*. Nature Nanotechnology, 2008. **3**(4): p. 210-215.
304. Adamson, A.W., *The physical chemistry of surfaces.* Abstracts of Papers of the American Chemical Society, 2001. **221**: p. U320-U320.
305. Ismach, A., et al., *Direct Chemical Vapor Deposition of Graphene on Dielectric Surfaces.* Nano letters, 2010. **10**(5): p. 1542-1548.
306. Taherian, F., et al., *What Is the Contact Angle of Water on Graphene?* Langmuir, 2013. **29**(5): p. 1457-1465.
307. Choi, K., T.J. Eom, and C. Lee, *Comparison of the removal efficiency for organic contaminants on silicon wafers stored in plastic boxes between UV/O-3 and ECR oxygen plasma cleaning methods.* Thin Solid Films, 2003. **435**(1-2): p. 227-231.
308. Smith, P.J. and P.M. Lindley, *Analysis of organic contamination in semiconductor processing.* Characterization and Metrology for Ulsi Technology, 1998. **449**: p. 133-139.

309. Kurokawa, A., et al., *Diagnosis and Cleaning of Carbon Contamination on SiO2 Thin Film.* Journal of Surface Analysis, 2009. **15**(3): p. 337-340.
310. Zubkov, T., et al., *Ultraviolet light-induced hydrophilicity effect on TiO2(110)(1x1). Dominant role of the photooxidation of adsorbed hydrocarbons causing wetting by water droplets.* Journal of Physical Chemistry B, 2005. **109**(32): p. 15454-15462.
311. Robertson, J. and E.P. Oreilly, *Electronic and Atomic-Structure of Amorphous-Carbon.* Physical Review B, 1987. **35**(6): p. 2946-2957.
312. Paci, J.T., T. Belytschko, and G.C. Schatz, *Computational studies of the structure, behavior upon heating, and mechanical properties of graphite oxide.* Journal of Physical Chemistry C, 2007. **111**(49): p. 18099-18111.
313. Kim, M.C., G.S. Hwang, and R.S. Ruoff, *Epoxide reduction with hydrazine on graphene: A first principles study.* Journal of Chemical Physics, 2009. **131**(6).
314. Gao, X.F., J. Jang, and S. Nagase, *Hydrazine and Thermal Reduction of Graphene Oxide: Reaction Mechanisms, Product Structures, and Reaction Design.* Journal of Physical Chemistry C, 2010. **114**(2): p. 832-842.
315. Bang, S., et al., *Al2O3 buffer in a ZnO thin film transistor with poly-4-vinylphenol dielectric.* Semiconductor Science and Technology, 2009. **24**(2).
316. Fan, J.P., et al., *Preparation and microstructure of multi-wall carbon nanotubes-toughened Al2O3 composite.* Journal of the American Ceramic Society, 2006. **89**(2): p. 750-753.
317. Tadanaga, K., J. Morinaga, and T. Minami, *Formation of superhydrophobic-superhydrophilic pattern on flowerlike alumina thin film by the sol-gel method.* Journal of Sol-Gel Science and Technology, 2000. **19**(1-3): p. 211-214.
318. Qie, L., et al., *Nitrogen‐Doped Porous Carbon Nanofiber Webs as Anodes for Lithium Ion Batteries with a Superhigh Capacity and Rate Capability.* Advanced Materials, 2012. **24**(15): p. 2047-2050.
319. Wang, H., et al., *Mn3O4− graphene hybrid as a high-capacity anode material for lithium ion batteries.* Journal of the American Chemical Society, 2010. **132**(40): p. 13978-13980.
320. Fan, Z.J., et al., *Nanographene-constructed carbon nanofibers grown on graphene sheets by chemical vapor deposition: high-performance anode materials for lithium ion batteries.* ACS Nano, 2011. **5**(4): p. 2787-94.
321. Shin, Y.J., et al., *Surface-Energy Engineering of Graphene.* Langmuir, 2010. **26**(6): p. 3798-3802.
322. Wu, Z.S., et al., *Doped Graphene Sheets As Anode Materials with Superhigh Rate and Large Capacity for Lithium Ion Batteries.* Acs Nano, 2011. **5**(7): p. 5463-5471.
323. Fan, J.P., et al., *Notice of dual publication "preparation and microstructure of multi-wall carbon nanotubes-toughened Al2O3 composite" (vol 89, pg 750, 2006).* Journal of the American Ceramic Society, 2006. **89**(8): p. 2674-2674.
324. Jiang, Z.Q. and Z.J. Jiang, *Effects of carbon content on the electrochemical performance of LiFePO4/C core/shell nanocomposites fabricated using FePO4/polyaniline as an iron source.* Journal of Alloys and Compounds, 2012. **537**: p. 308-317.

325. Wang, C.Y., et al., *Electrochemical Properties of Graphene Paper Electrodes Used in Lithium Batteries.* Chemistry of Materials, 2009. **21**(13): p. 2604-2606.
326. Shen, L., et al., *Design and Tailoring of a Three-Dimensional TiO2–Graphene–Carbon Nanotube Nanocomposite for Fast Lithium Storage.* The Journal of Physical Chemistry Letters, 2011. **2**(24): p. 3096-3101.
327. Li, S., et al., *Vertically Aligned Carbon Nanotubes Grown on Graphene Paper as Electrodes in Lithium‐Ion Batteries and Dye‐Sensitized Solar Cells.* Advanced Energy Materials, 2011. **1**(4): p. 486-490.
328. Wang, Z.L., et al., *Facile, mild and fast thermal-decomposition reduction of graphene oxide in air and its application in high-performance lithium batteries.* Chemical Communications, 2012. **48**(7): p. 976-978.
329. Bhardwaj, T., et al., *Enhanced Electrochemical Lithium Storage by Graphene Nanoribbons.* Journal of the American Chemical Society, 2010. **132**(36): p. 12556-12558.
330. Wen, Z.H., et al., *Binding Sn-based nanoparticles on graphene as the anode of rechargeable lithium-ion batteries.* Journal of Materials Chemistry, 2012. **22**(8): p. 3300-3306.
331. Xiang, H.F., et al., *Graphene sheets as anode materials for Li-ion batteries: preparation, structure, electrochemical properties and mechanism for lithium storage.* Rsc Advances, 2012. **2**(17): p. 6792-6799.
332. Vinayan, B.P., et al., *Synthesis of graphene-multiwalled carbon nanotubes hybrid nanostructure by strengthened electrostatic interaction and its lithium ion battery application.* Journal of Materials Chemistry, 2012. **22**(19): p. 9949-9956.
333. Kim, H., et al., *Graphene-Based Hybrid Electrode Material for High-Power Lithium-Ion Batteries.* Journal of the Electrochemical Society, 2011. **158**(8): p. A930-A935.
334. Zhou, H.S., et al., *Lithium storage in ordered mesoporous carbon (CMK-3) with high reversible specific energy capacity and good cycling performance.* Advanced Materials, 2003. **15**(24): p. 2107-+.
335. Aurbach, D., *Review of selected electrode-solution interactions which determine the performance of Li and Li ion batteries.* Journal of Power Sources, 2000. **89**(2): p. 206-218.
336. Balandin, A.A., et al., *Superior thermal conductivity of single-layer graphene.* Nano letters, 2008. **8**(3): p. 902-907.
337. Mukherjee, R., et al., *Photothermally Reduced Graphene as High-Power Anodes for Lithium-Ion Batteries.* ACS Nano, 2012. **6**(9): p. 7867-7878.
338. Xing, W.B. and J.R. Dahn, *Study of irreversible capacities for Li insertion in hard and graphitic carbons.* Journal of the Electrochemical Society, 1997. **144**(4): p. 1195-1201.
339. Wu, Y.P., et al., *Effects of catalytic oxidation on the electrochemical performance of common natural graphite as an anode material for lithium ion batteries.* Electrochemistry Communications, 2000. **2**(4): p. 272-275.
340. Liu, T., et al., *Effect of vacuum carbonization treatment on the irreversible capacity of hard carbon prepared from biomass material.* Materials Letters, 2010. **64**(1): p. 74-76.

341. Concheso, A., et al., *Electrochemical improvement of low-temperature petroleum cokes by chemical oxidation with H2O2 for their use as anodes in lithium ion batteries.* Electrochimica Acta, 2006. **52**(3): p. 1281-1289.
342. Chang, Y.C., et al., *Anodic performances of coke from coals.* Carbon, 1998. **36**(11): p. 1653-1662.
343. Concheso, A., et al., *Influence of the oxidative stabilisation treatment time on the electrochemical performance of anthracene oils cokes as electrode materials for lithium batteries.* Journal of Power Sources, 2006. **161**(2): p. 1324-1334.
344. Chen, X.C., et al., *A graphene-based nanostructure with expanded ion transport channels for high rate Li-ion batteries.* Chemical Communications, 2012. **48**(47): p. 5904-5906.
345. Xiao, X.C., P. Lu, and D. Ahn, *Ultrathin Multifunctional Oxide Coatings for Lithium Ion Batteries.* Advanced Materials, 2011. **23**(34): p. 3911-+.
346. Zhao, X., et al., *Flexible Holey Graphene Paper Electrodes with Enhanced Rate Capability for Energy Storage Applications.* ACS Nano, 2011. **5**(11): p. 8739-8749.
347. Wu, H., et al., *Stable cycling of double-walled silicon nanotube battery anodes through solid-electrolyte interphase control.* Nature Nanotechnology, 2012. **7**(5): p. 309-314.
348. Luo, Z.T., et al., *Photoluminescence and band gap modulation in graphene oxide.* Applied Physics Letters, 2009. **94**(11).
349. Peng, X.S., et al., *Photoluminescence and infrared properties of alpha-Al2O3 nanowires and nanobelts.* Journal of Physical Chemistry B, 2002. **106**(43): p. 11163-11167.